# DEVELOPMENT OF CONTROLLED ROCKING REINFORCED MASONRY WALLS

# DEVELOPMENT OF CONTROLLED ROCKING REINFORCED MASONRY WALLS

By

Ahmed Mohamed Abdellatif Yassin

B.Sc., M.Sc.

A Thesis Submitted to the School of Graduate Studies in Partial Fulfillment of the Requirements for the Degree Doctor of Philosophy

McMaster University



October 2021

Doctor of Philosophy (2021) McMaster University

(Civil Engineering) Hamilton, Ontario

TITLE: DEVELOPMENT OF CONTROLLED ROCKING REINFORCED MASONRY WALLS

AUTHOR: Ahmed Yassin
B.Sc., M.Sc. (Ain Shams University)

SUPERVISORS: Dr. Lydell Wiebe
Dr. Mohamed Ezzeldin

NUMBER OF PAGES: xxiii, 211

## ABSTRACT

The structural damage after the Christchurch earthquake (2011) led to extensively damaged facilities that did not collapse but did require demolition, representing more than 70% of the building stock in the central business district. These severe economic losses that result from conventional seismic design clearly show the importance of moving towards resilience-based design approaches of structures. For instance, special reinforced masonry shear walls (SRMWs), which are fixed-base walls, are typically designed to dissipate energy through the yielding of bonded reinforcement while special detailing is maintained to fulfill ductility requirements. This comes at the expense of accepting residual drifts and permanent damage in potential plastic hinge zones. This design process hinders the overall resilience of such walls because of the costs and time associated with the loss of operation and service shutdown.

In controlled rocking systems, an elastic gap opening mechanism (i.e., rocking joint) replaces the typical yielding of the main reinforcement in conventional fixed-base walls, hence reducing wall lateral stiffness without excessive yielding damage. Consequently, controlled rocking wall systems with limited damage and self-centering behavior under the control of unbonded post-tensioning (PT) are considered favorable for modern resilient cities because of the costs associated with service shutdown (i.e., for structural repairs or replacement) are minimized. However, the difficulty of PT implementation during construction is challenging in practical masonry applications. In addition, PT losses due to PT yielding and early strength degradation of masonry reduce the self-centering ability of controlled rocking masonry walls with unbonded post-tensioning (PT-CRMWs). Such challenges demonstrate the importance of considering an alternative source of self-centering.

In this regard, the current study initially evaluates the seismic performance of PT-CRMWs compared to SRMWs. Next, a new controlled rocking system for masonry walls is proposed, namely Energy Dissipation-Controlled Rocking Masonry Walls (ED-CRMWs), which are designed to self-center through vertical gravity loads only, without the use of PT tendons. To control the rocking response, supplemental energy dissipation (ED) devices are included. This proposed system is evaluated experimentally in two phases. In *Phase I* of the experimental program, the focus is to ensure that the intended behavior of ED-CRMWs is achieved. This is followed by design guidance, validated through collapse risk analysis of a series of 20 ED-CRMW archetypes. Finally, *Phase II* of the experimental program evaluates a more resilient ED-CRMW is evaluated, which incorporates a readily replaceable externally mounted flexural arm ED device. Design guidance is also provided for ED-CRMWs incorporating such devices.

## DEDICATIONS

*To*

*My Father & Mother,*

## ACKNOWLEDGMENTS

I would like to express my sincere gratitude and deep appreciation to my supervisors Dr. Lydell Wiebe and Dr. Mohamed Ezzeldin. I was lucky to be supervised by such advisors with their encouragement, support, advice, and innovative ideas. I am especially grateful for our discussions that significantly impacted the quality of the dissertation. Special thanks are due to my supervisory committee members, Dr. Wael El-Dakhakhni and Dr. Georgios Balomenos for their valuable advice and suggestions. Their helpful comments and discussions during our meetings are greatly appreciated.

The experimental work would not be possible without the help of my peers and colleagues: Anerban, Berg Ellemers, Kegan Amy, Madona Gouda, and Brenden Lie. They really helped me a lot and no words can express my gratitude to each of them enough. Deep thanks to my friend Mohamed El-Sefy, Ricky Darlington, Ahmed Geith, Moamen Galal, Matt East, Ahmed Yosri, Ahmed Alaa, Mohamed Salah, Yasien Salaheldin, and Mohamed Gamal for helping me during the construction phases of the experimental work. A word of thanks is due to the Applied Dynamic Laboratory technicians Mr. Paul Heerema and Mr. Kent Wheeler for their unwavering help. Finally, many thanks due to my former masters' supervisors at Ain Shams University whom introduced me to the fundamentals of structural engineering, Drs. Marwan Shedid, and Hussien Okail.

I am thankful for the research funding support provided through the Natural Sciences and Engineering Research Council (NSERC) of Canada, and the Canada Masonry Design Centre (CMDC). Many thanks to Dr. Bennett Banting of CMDC for providing valuable comments on the reinforced masonry practice in Canada, and for the expert masons Mr. Mario De Nicola. Support was also provided by the McMaster University Centre for Effective Design of Structures (CEDS), funded through the Ontario Research and Development Challenge Fund (ORDCF) of the Ministry of Research and Innovation (MRI). The provision of the scaled blocks through a grant from the Canadian Concrete Masonry Producers Association (CCMPA) is gratefully acknowledged.

At last, but by no means the least, I would like to say that no words can express my sincere gratitude to my parents, Mohamed Abdellatif and Soad Abdelazim, and to my brother, Raed, for their patience, care, support, and everything they did, and are still doing for me. Without their continuous support, love, prayer, and encouragement throughout my life, I would have never been the one I am now.

# TABLE OF CONTENTS

# LIST OF FIGURES

# LIST OF TABLES

## DECLARATION OF ACADEMIC ACHIEVEMENT

This thesis has been prepared in accordance with the regulations for a sandwich thesis format as a compilation of research papers stipulated by the faculty of graduate studies at McMaster University. This research presents experimental and numerical work carried out solely by Ahmed Yassin. Advice and guidance were provided for the whole thesis by the academic supervisors Dr. Lydell Wiebe and Dr. Mohamed Ezzeldin. Dr. Taylor Steele provided assistance for only chapter 2 fragility output. Information presented from outside sources, which has been used towards analysis or discussion, has been cited where appropriate; all other materials are the sole work of the author. This thesis consists of the following manuscripts in the following chapters:

**Chapter 2**

Yassin, A., Ezzeldin, M., Steele, T., and Wiebe, L. (2020). "Seismic Collapse Risk Assessment of Posttensioned Controlled Rocking Masonry Walls." *J. Struct. Eng*., 146(5), 04020060-1-16, DOI: https://doi.org/10.1061/(ASCE)ST.1943-541X.0002599

**Chapter 3**

Yassin, A., Ezzeldin, M., and Wiebe, L. (2021). "Experimental Assessment of Controlled Rocking Masonry Shear Walls without Posttensioning." *J. Struct. Eng*., (Submitted-STENG-10720).

**Chapter 4**

Yassin, A., Ezzeldin, M., and Wiebe, L. (2021). "Seismic Design and Performance Evaluation of Controlled Rocking Masonry Shear Walls without Posttensioning." *J. Struct. Eng*., (Submitted-STENG-10776).

**Chapter 5**

Yassin, A., Ezzeldin, M., and Wiebe, L. (2021). "Experimental Assessment of Resilient Controlled Rocking Masonry Walls with Replaceable Energy Dissipation." *J. Struct. Eng*., (In preparation).

# Chapter 1

## INTRODUCTION

## 1.1. BACKGROUND AND MOTIVATION

The masonry construction industry represents a historically significant portion of both existing and new residential, commercial and institutional buildings. Seismic force-resisting systems, such as special reinforced masonry shear walls, are designed to dissipate energy through inelastic behavior and yielding of main reinforcement, which requires special detailing to insure system ductility. Although the inelastic response is appealing as it allows for the reduction of design forces, it leads to damage of structural elements and permanent deformations (residual drifts). This damage may even require the replacement of the whole structural element if the damage is beyond repair. This is a major drawback as business operations will be required to shut down for a period of time. Also, the costs of repairing damaged structural and non-structural components, as well as costs associated with business operation loss (which may be greater than the structure itself), all lead to structures that cannot be described as resilient.

In this regard, rocking systems have been increasingly studied and are considered promising seismic force-resisting systems for more resilient buildings (Priestley et al. 1999). This is attributed to their ability to withstand major earthquakes with minor residual drifts and with limited structural damage concentrated at the rocking base interface (Kurama et al. 1999). This, in return, is

favorable for modern resilient cities because it minimizes the costs associated with service shutdown for structural repairs or replacement. In a post-tensioned controlled rocking masonry wall (PT-CRMW), the restoring force of post-tensioning restores the wall to its vertical plumb alignment. This mechanism is called the self-centering ability of the system. In addition, softening of the force-deformation response is achieved through an elastic gap opening mechanism (rocking at the base), replacing the typical yielding of reinforcement in special reinforced masonry shear walls. Rocking is initiated when the base overturning moment caused by lateral load exceeds the decompression moment capacity, and hence the wall uplifts from the foundation and forms a single horizontal crack at the wall-foundation interface.

Studies have been carried out on the rocking mechanism of unbonded PT-CRMWs. Limited damage and self-centering have been proven through several experimental studies of masonry walls, where PT-CRMWs were tested under quasi-static (Laursen and Ingham 2001, 2004a, 2004b; Rosenboom and Kowalsky 2004; Hassanli et al. 2016) and dynamic (Wight et al. 2006) loading. In general, PT-CRMWs responded with a rocking behavior (i.e., mainly local damage at the wall toes) along with low residual drifts. However, because PT-CRMWs are a new seismic force-resisting system relative to reinforced masonry (RM) walls with bonded reinforcement (i.e., fixed-base walls), no distinct seismic response modification factors are yet provided in North American building codes and design standards for PT-CRMWs. For special and ordinary RM wall systems, ASCE/SEI

7-16 (ASCE/SEI 2016) assigns a response modification factor, *R*, of 5.0 and 2.0, respectively. However, for prestressed masonry walls, a relatively low *R* value of 1.5 is given. In addition, the Building Code Requirements and Specification for Masonry Structures (e.g., TMS 402/602 2016) currently considers prestressed masonry walls similar to ordinary unreinforced masonry walls. The low *R* value is mainly attributed to the absence of vertical mild reinforcement to provide ductile behavior for these walls. This is for bonded tendons; however, for an unbonded prestressed masonry wall designed with a gap opening mechanism (i.e., PT-CRMWs), a significant reduction in the wall lateral stiffness occurs at small drifts, which results in an apparently ductile response but without inelastic deformations. Therefore, there is a need to evaluate whether a distinctive *R* value should be assigned to PT-CRMWs, in future editions of the ASCE/SEI 7, to account for the unique rocking ability of such walls.

Despite such advantages, the practical application of unbonded PT is typically limited to precast concrete shear walls, while in the case of masonry it is challenging because of the cast-in-situ condition. Also, the application of unbonded PT tendons in masonry raises concerns due to the high compression demands on masonry crushing toes when dead and live loads are added in practical construction scenarios, as reported by Laursen and Ingham (2004b) when both PT and slab axial load were used in the testing. This is mainly due to the low crushing strain capacity of masonry compared to concrete, especially without confinement detailing (Priestley and Elder 1983). In addition, PT losses due to PT yielding and masonry

early degradation (Hassanli et al. 2016) affect the self-centering capability of PT-CRMWs. Such challenges clearly demonstrate the importance of considering an alternative source of self-centering.

In addition, the introduction of masonry confined boundary elements detailed as confined masonry column pilasters has been used in special RM wall systems (i.e., fixed base walls) (Shedid et al. 2010; Banting and El-Dakhakhni 2014; Ezzeldin et al. 2017) as it minimizes the wall structural damage and instability; however, it has not been incorporated in rocking walls. Another form of confinement is placing steel plates inside the bed joints at wall corners known as Priestley plates (Priestley and Elder 1982; Hart et al. 1989), which has been used by Laursen and Ingham (2004a), and Rosenboom and Kowalsky (2004) in PT-CRMWs. The failure mechanism of unconfined prisms as described by Priestley and Elder (1982) is initiated due to high lateral expansion of mortar leading to the vertical splitting of the concrete masonry units. This occurs before grout crushing, which lowers the strain at peak stress to approximately 0.0015. Consequently, confining plates placed at the mortar bed joints inhibit the vertical splitting induced by mortar expansion, resulting in a more gradual falling branch to the stress-strain curve.

## 1.2. MOTIVATION

Based on all of the aforementioned issues, the main motivation behind this study is to present a new controlled rocking technique for flexure-dominated

masonry walls with aspect ratios greater than one, namely Energy Dissipation-Controlled Rocking Masonry Walls (ED-CRMWs), that needs to be experimentally tested in order to validate the new self-centering technique. The study evaluates the capability of the proposed system to self-center through vertical gravity loads only, without the use of PT tendons, while a supplemental energy dissipation (ED) source in a form of an internal unbonded axial yielding ED bar is designed to increase the system supplemental damping and ultimate strength, and also to control lateral displacements. Since confining of masonry crushing toes is an important aspect to enhance the wall ductility, the use of confined boundary elements and steel plates is also considered herein when adopted in ED-CRMWs.

In addition to the need for an experimental study in order to address these issues, there is also a need for a detailed design approach and seismic performance evaluation for the newly proposed ED-CRMWs, as no design approach for a rocking masonry with energy dissipation is provided yet in North American standards. This is unlike concrete rocking shear walls, which are addressed in ACI ITG-5.2 (2009) design guideline. The main motivation behind this is to facilitate the adoption of ED-CRMWs as a new resilient seismic force resistant system in North American codes and standards. In this regard, a design approach for the ED-CRMW configuration is introduced herein to provide a complete view of the system.

The effect of higher modes in wall responses was observed experimentally under dynamic testing (Ghorbanirenani et al. 2012), where additional plastic hinges

can develop above fixed-base walls; however, the nonlinear action in a rocking system (such as PT-CRMWs or ED-CRMWs) only occurs at the wall-foundation rocking interface. This mechanism does not limit the higher-mode response (Wiebe and Christopoulos 2015; Rutenberg, A. 2011), which has been shown numerically to contribute significantly to rocking systems. In this regard, there is also a need to incorporate the effect of higher modes in the design approach to mitigate their effect.

Despite the advantages of ED-CRMWs with internally unbonded ED bars in terms of the cost savings by avoiding post-tensioning and the simplicity of the energy dissipation used that fits with common practice construction, one limitation of this system is that the internal energy dissipation is unreachable and unreplaceable after seismic event damage. Therefore, there is a need for further upgrade to use a replaceable energy dissipation device in order to further enhance the seismic resilience of ED-CRMWs. To address this need, testing of individual flexural arms was previously conducted by Li (2019), leading to promising results that encourage implementation in ED-CRMWs. In this regard, a special connection detail needs to be developed to ensure an effective connection between the flexural arm and the wall body that preserves the unique performance of the ED-CRMWs in terms of limited damage and self-centering capability. The connection of the flexural arm to the wall is through a special steel hollow block, which should allow simple replacement within a short time after seismic event damage, so as to satisfy the immediate occupancy performance level.

## 1.3. RESEARCH OBJECTIVES

Based on the research gaps identified above, the main objective of this dissertation is to provide the necessary data to support the codification of ED-CRMWs as an alternative to PT-CRMWs and SRMWs. To do this, the following objectives were defined:

1) Assess the collapse margin ratios of PT-CRMWs through nonlinear dynamic analysis, and based on that, propose a response modification factor for this system.

2) Develop experimentally the concept of eliminating the PT tendons in ED-CRMWs through relying on gravity loads to self-center the wall with the intended limited damage.

3) Propose a design methodology for the ED-CRMWs that can be adopted in standards, and evaluate the seismic performance of the proposed system.

4) Experimentally verify the implementation of a new energy dissipation device with a special connection to the ED-CRMWs, to improve the seismic resilience.

## 1.4. THESIS ORGANIZATION

This dissertation comprises six chapters, starting with this introductory chapter, followed by four chapters covering the objectives of the thesis, and finally ending with a concluding chapter that summarizes the main findings of the research. The following paragraphs give a brief description of the content of each chapter.

- **Chapter 1** presents the motivation and objectives of the dissertation as well as background information pertaining to the research program.
- **Chapter 2** contains a seismic collapse risk assessment of 20 unbonded post-tensioned controlled rocking masonry walls following the FEMA P695 (FEMA 2009) methodology. These walls are designed for the same seismic performance factors as previously reported for special reinforced masonry shear walls (i.e., *R* equals 5) to compare and evaluate the rocking system. To conduct the evaluation, a numerical model is developed and validated. Afterwards, nonlinear static and dynamic analyses are performed following the FEMA P695 methodology. Finally, the analysis results are compared to corresponding results for special reinforced masonry shear walls in terms of equivalent safety against collapse risk.
- **Chapter 3** contains a description of *Phase I* experimental program, material properties, test setup, loading protocol and instrumentation of six ED-CRMWs with internally unbonded axial yielding bars. Following the experimental program description, the chapter focuses on quantifying the effects of confining strategies (boundary elements and confining plates), level of axial load, and location of ED on the rocking wall response. This is performed by comparing the damage sequence, the force-displacement hysteretic behavior, the self-centering behavior, the displacement ductility and the wall stiffness between all six walls. Finally, the flexural strength

predictions according to TMS 402/602 (2016) and observed experimental strengths are compared.

- **Chapter 4** presents and validates a design approach for the proposed ED-CRMW system, considering the influence of higher mode effects. Afterwards, the system seismic response modification factor to be proposed for ASCE 7 is investigated using collapse risk analysis, as no distinct values are yet provided for the proposed system. Moreover, an investigation is conducted on how the design parameters such as the response modification factor, amount of ED, and level of axial compression influence the collapse performance of ED-CRMWs.
- **Chapter 5** describes *Phase II* of the experimental program which addresses enhanced controlled rocking masonry walls with externally attached energy dissipation. This solves the limitation of internal energy dissipation being unreachable and unreplaceable after damage due to yielding or fracturing. Moreover, a special hollow steel block connection is introduced to limit the spread of damage at the base for the enhanced wall. In addition, the externally attached energy dissipation is replaced with new flexural arms after the testing, and retesting of the enhanced controlled rocking wall is reported. Afterwards, the test results of the repaired wall are compared with the original wall in terms of damage sequence, force-displacement hysteretic behavior, self-centering, displacement ductility, energy dissipation and damping. These comparisons are used to quantify the

system resilience and the efficiency of the restoration technique. Finally, design guidance is presented for the newly introduced flexural energy dissipation connection with the wall body, so as to be implemented in the design standards.

- **Chapter 6** provides a reflective summary of the research, draws out the overall implications of the research and key findings that clearly answer the main research question, and offers major conclusions and recommendations for future research.

It should be noted that although each chapter presents a standalone journal manuscript, Chapters 2, 3, 4 and 5 collectively describe a cohesive research program as outlined in this introductory chapter of the dissertation. Nonetheless, for completeness of the individual standalone manuscripts, some overlap is unavoidable.

## 1.5. REFERENCES

ACI ITG-5.2 (American Concrete Institute). (2009). "Requirements for Design of a Special Unbonded Post-Tensioned Precast Shear Wall Satisfying ACI ITG-5.1 & Commentary." *ACI ITG-5.2-09*, Farmington Hills, MI.

ASCE/SEI (Structural Engineering Institute). (2016). "Minimum design loads for buildings and other structures." *ASCE/SEI 7-16*, Reston, VA.

Banting, B., and El-Dakhakhni, W. (2014). "Seismic performance quantification of reinforced masonry structural walls with boundary elements." *Journal of*

*Structural Engineering*, 10.1061/(ASCE)ST.1943-541X.0000895, 04014001.

Ezzeldin, M., El-Dakhakhni, W., and Wiebe, L. (2017). "Experimental assessment of the system-level seismic performance of an asymmetrical reinforced concrete block–wall building with boundary elements." *J. Struct. Eng*., 143(8), 04017063.

FEMA. (2009). "Quantification of building seismic performance factors." *FEMA P695*, Washington, DC.

Ghorbanirenani, I., Tremblay, R., Léger, P., and Leclerc, M. (2012). "Shake table testing of slender RC shear walls subjected to eastern North America seismic ground motions." *Journal of Structural Engineering*, 138(12), 1515‑1529.

Hart, G. C., Sajjad, N., Kingsley, G. R., and Noland, J. L. (1989). "Analytical stress-strain curves for grouted concrete masonry." *Masonry Soc. J*., 8(1), 21–34.

Hassanli, R., ElGawady, M., and Mills, J. (2016). "Experimental investigation of in-plane cyclic response of unbonded-posttensioned masonry walls." *Journal of Structural Engineering*, 142(5), 04015171-1-15.

J. Li. (2019) Development of a flexural yielding energy dissipation device for controlled rocking masonry walls, MASc Thesis: McMaster University.

Laursen, P. T. and Ingham, J. M. (2001). "Structural Testing of Single-Story Post-Tensioned Concrete Masonry Walls." *The Professional Journal of The*

*Masonry Society*, 19(1), 69-82.

Laursen, P. T. and Ingham, J. M. (2004a). "Structural testing of enhanced post-tensioned concrete masonry walls." *ACI Journal*, 101(6), 852-862.

Laursen, P. T. and Ingham, J. M. (2004b). "Structural testing of large-scale posttensioned concrete masonry walls." *Journal of Structural Engineering*, 130(10), 1497-1505.

Priestley, M. J. N., and Elder, D. M. (1982). "Cyclic loading tests of slender concrete masonry shear walls." *Bull. N.Z. Natl. Soc. Earthquake Eng*., 15(1), 3–21.

Priestley, M. J. N., and Elder, D. M. (1983). "Stress-strain curves for unconfined and confined concrete masonry." *ACI Journal*, 80(19), 192–201.

Priestley, M. J. N., Sritharan, S., Conley, J.R., and Pampanin, S. (1999). "Preliminary results and conclusions from the PRESSS five-story precast concrete test building." *PCI Journal*, 44(6), 42–67.

Rutenberg, A. (2011). "Seismic shear forces on RC walls: review and bibliography." *Bulletin of Earthquake Engineering*, 11(5),1726‑1751.

Rosenboom, O. A., and Kowalsky, M. J. (2004). "Reversed in-plane cyclic behavior of posttensioned clay brick masonry walls." *Journal of Structural Engineering*, 10.1061/(ASCE)0733-9445(2004)130:5(787), 787–798.

Shedid, M. T., El-Dakhakhni, W. W., and Drysdale, R. G. (2010). "Alternative

strategies to enhance the seismic performance of reinforced concrete-block shear wall systems." *Journal of Structural Engineering*, 10.1061/(ASCE)ST .1943-541X.0000164, 676–689.

TMS (The Masonry Society). (2016). "Building Code Requirements and Specification for Masonry Structures." *TMS 402/602-16*, Longmont, CO.

Wiebe, L., and Christopoulos, C. (2015). "A cantilever beam analogy for quantifying higher mode effects in multistorey buildings." *Earthquake Engineering & Structural Dynamics*, 44(11), 1697-1716

Wight, G. D., Ingham, J. M., and Kowalsky, M. J. (2006). "Shake table Testing of Rectangular Post-Tensioned Concrete Masonry Walls." *PCI Journal*, 103(4), 587-595.

# Chapter 2

## SEISMIC COLLAPSE RISK ASSESSMENT OF POST-TENSIONED CONTROLLED ROCKING MASONRY WALLS

## 2.1. ABSTRACT

The use of vertical unbonded post-tensioned (PT) bars in masonry walls results in a controlled rocking behavior that can provide a high drift capacity and also re-center the wall to its vertical alignment, minimizing residual drifts after a seismic event. However, because post-tensioned controlled rocking masonry walls (PT-CRMWs) are a relatively new seismic force-resisting system relative to reinforced masonry (RM) walls with bonded reinforcement (i.e., fixed base walls), no distinct seismic response modification factors are yet provided in North American building codes and design standards for PT-CRMWs. In addition, following the FEMA P695 methodology, the National Institute of Standards and Technology (NIST) reported that some conventional low-rise RM walls could experience an excessive risk of collapse under the maximum considered earthquake (MCE). For these reasons, the current study evaluates the collapse risk of PT-CRMWs when designed using the seismic response modification factors currently assigned for special RM walls. In this respect, OpenSees is first used to develop and validate multi-spring macro models to simulate the seismic response of 20 PT-CRMWs with different configurations and axial load levels. The models are then used to perform nonlinear static and dynamic analyses following the FEMA P695 methodology, which

involves evaluating the wall overstrength and seismic collapse margin ratio relative to the MCE. The results demonstrate that low-rise PT-CRMWs, designed with the seismic response modification factors currently assigned by ASCE 7-16 to special RM walls, can meet the FEMA P695 acceptance criteria for the expected seismic collapse risk under the MCE. However, the peak forces in high-rise PT-CRMWs are governed by higher mode effects, which increase the collapse risk due to shear. Finally, the influence of confinement on reducing the collapse risk of PT-CRMW archetypes is evaluated.

## 2.2. INTRODUCTION

Post-tensioned controlled rocking masonry walls (PT-CRMWs) have lateral strength that comes primarily from vertical unbonded post-tensioned (PT) bars. Because of the lack of bond, horizontal cracks are expected to form only at the wall–foundation interface when these walls are subjected to in-plane demands, such as seismic loading. This is intended to be followed by a rocking behavior that has a high drift capacity and that also localizes the damage (Priestley et. al 1999). In addition, PT-CRMWs have a desirable ability to return back to their original vertical alignment when the lateral load is removed (i.e. to self-center), as shown in Fig. 2.1, provided that sufficient prestress forces remain in the bars (Laursen and Ingham 2001, 2004a, 2004b). Moreover, there is no strain compatibility between the unbonded PT bars and the adjacent masonry, so the elongation of these bars is distributed over their lengths. This protects masonry from cracking because tensile

stresses are not transferred from the PT bars through bond. Consequently, PT-CRMWs are expected to undergo less damage compared to conventional reinforced masonry (RM) walls (i.e. fixed base) when both wall systems are subjected to similar lateral displacement demands. This was demonstrated for reinforced concrete walls by Holden et al. (2003), where a conventional fixed-base reinforced concrete wall developed severe flexural cracks at a lateral drift of 2.5%, while an unbonded PT concrete rocking wall with the same dimensions and subjected to a similar lateral loading protocol had only superficial cracks until a lateral drift of 3.0%.

Several experimental studies have been conducted to evaluate the performance of PT masonry walls subjected to in-plane cyclic or dynamic loading demands. For example, Laursen (2002) investigated the influence of different geometrical and design parameters on the performance of unbonded PT masonry walls subjected to in-plane cyclic loading. These parameters included the wall aspect ratio, prestressing level, grouting, location of PT bars, energy dissipation devices and confinement plates. Wight et al. (2006) evaluated the lateral performance of one fully-grouted and three partially-grouted rectangular unbonded PT masonry walls under dynamic shaking table tests. Recently, Hassanli et al. (2016a) tested four fully-grouted unbonded PT masonry walls with different PT distributions and initial stressing values using in-plane cyclic loading. In general, fully-grouted walls responded primarily with a rocking behavior (i.e. mainly local

damages at the wall toes) along with higher self-centering abilities and lower residual drifts, when compared to those of their partially-grouted counterparts.

For special and ordinary RM walls systems, ASCE/SEI 7-16 (ASCE/SEI 2016) assigns a response modification factor, *R*, of 5.0 and 2.0, respectively. However, for prestressed masonry walls, a relatively low *R* value of 1.5 is given. In addition, the Masonry Standards Joint Committee (MSJC) (2013) currently considers prestressed masonry walls as ordinary unreinforced masonry walls. The low *R* value is mainly attributed to the absence of vertical mild reinforcement to provide ductile behavior for these walls. This is for bonded tendons; however, for an unbonded prestressed masonry wall designed for a gap opening mechanism, a significant reduction in the wall lateral stiffness occurs at small drifts, which results in an apparently ductile response but without any inelastic deformations. Therefore, there is a need to evaluate whether a distinctive *R* value should be assigned to PT-CRMWs, in future editions of the ASCE/SEI 7, to account for the unique rocking ability of such walls.

A methodology has been defined in FEMA P695 (FEMA 2009), *Qualification of Building Seismic Performance Factors*, to evaluate the seismic performance factors assigned to a seismic force-resisting system. The methodology considers the uncertainties associated with the ground motion, design, modeling, and test data in a probabilistic collapse risk assessment. The acceptance criteria of this methodology are defined based on achieving an acceptable collapse margin

ratio (CMR) between the median collapse spectral intensity of a suite of ground motions and the spectral intensity of the maximum considered earthquake (MCE).

The main objective of the current study is to assess the seismic collapse risk of fully-grouted unbonded PT-CRMWs with self-centering ability using the FEMA P695 methodology (FEMA 2009). First, a set of archetype walls is designed taking the seismic performance factors as those currently assigned in ASCE/SEI 7-16 (ASCE/SEI 2016) for special reinforced masonry walls (SRMWs). Subsequently, a simplified two-dimensional numerical model is developed using OpenSees (McKenna et al. 2000), and data from previous experimental test programs are used to validate the model. Following the model validation, nonlinear static pushover and multiple stripe dynamic analyses are performed on 20 unbonded PT-CRMW archetypes. The results of these archetypes are compared to the values reported for their SRMW counterparts by the GCR 10-917-8 study (NIST 2010), in terms of the collapse risk under the MCE. Finally, the influence of confinement on enhancing the CMR of the PT-CRMW archetypes is evaluated using collapse fragility curves.

## 2.3. NUMERICAL MODEL

A multi-spring macro-modeling approach can explicitly account for the hysteric energy dissipation capacities resulting from the inelastic strains in the masonry and PT bars. As such, several previous studies (e.g. Pennucci et al. 2009; Watkins et al. 2013) have used this modeling approach to simulate the cyclic behavior of controlled rocking precast concrete walls. In this approach, a bed of compression-

only axial springs is used to simulate the wall-foundation interface, while a truss element is used to represent each PT bar. The above studies demonstrated that a multi-spring macro-modeling approach was able to capture the experimental rocking deformations under cyclic loading. Therefore, this approach is also used in the current study to simulate the overall seismic behavior of PT-CRMWs

### 2.3.1. MODEL DESCRIPTION

Fig. 2.2 shows a schematic diagram of the wall model that was formulated in OpenSees (McKenna et al. 2000). As shown in the figure, the model contains four main elements: 1) a bed of spring elements to represent the wall-foundation rocking interface; 2) truss elements to represent the PT bars; 3) elastic Timoshenko beam-column elements to represent the wall panel; and 4) a leaning column using elastic beam-column elements to represent the gravity system associated with the PT-CRMW and subsequently capture the P-Delta effects on the wall. At the end of the leaning column, a rotational spring with a very low stiffness is introduced so that the column does not contribute to the stiffness of the wall.

At the wall-foundation rocking interface, all springs are defined by zero-length elements with a nonlinear constitutive material model for masonry. The spring elements are fixed at the base and connected via rigid links to the bottom of the Timoshenko beam-column element, as shown in Fig. 2.2. According to several previous experimental investigations, two main assumptions were made in the current study to model the rocking wall interface: 1) the inelastic action of the

masonry wall was concentrated at the rocking interface (Aaleti and Sritharan 2011); and 2) the wall uplift and toe compression were based on only wall base rotation (Hassanli et al. 2016a).

The choice of the number of springs is an important aspect, where the accuracy of the model is enhanced when at least 20 springs are used to represent the wall-foundation interface (Pennucci et al. 2009). A small spacing between springs is also required to avoid convergence issues caused by a large variation in stress between adjacent springs. For these reasons, the spacing between the spring elements in the current study is always set to be 10 mm.

To define the properties of each spring, the vertical displacement of the spring corresponding to the strain at the maximum compressive stress in masonry, $\varepsilon_m$, is assumed to be $\varepsilon_m$ multiplied by the height of equivalent plastic deformations, where $\varepsilon_m$ is taken as 0.003 according to NIST (2010) based on the prism test data of Atkinson and Kingsley (1985). As will be shown in the numerical results, the wall response can be captured well if the equivalent plastic hinge length, $L_p$, representing the equivalent height of plastic curvature (Laursen 2002; Thomas and Sritharan 2004; Hassanli at al. 2016b; Hassanli at al. 2017), is estimated accurately. Several formulae are available in the literature to estimate $L_p$ of conventional fixed-base shear walls (e.g. Paulay and Priestley 1992; Priestley et al. 2007), but none of these formulae provided a good correlation with the experimental results of the PT-CRMWs considered in the current study. Instead, the formula proposed by Hassanli et al. (2015), which is based on nonlinear finite-element analysis results of 45

unbonded PT masonry shear walls, was found to give the value of $L_p$ that produced the best agreement between the model and experimental results. The formulae for $L_p$ (in mm) are presented in Eqs. (2.1) and (2.2) and are given in terms of the wall length, $L_w$, in mm, the masonry compressive strength, $f_m^{'}$, and the wall axial compressive stress, $f_m$.

$$L_p = 0.11L_w + 3475\frac{f_m}{f_m^{'}} \qquad \text{for } L_w \le 3000\ mm \tag{2.1}$$

$$L_p = 0.18L_w + 1.10L_w\frac{f_m}{f_m^{'}} \qquad \text{for } L_w > 3000\ mm \tag{2.2}$$

Henry et al. (2012) experimentally and analytically investigated the behavior of unbonded PT concrete walls and reported that the wall panel behaved elastically at a short distance above a single horizontal crack located at the wall-foundation rocking interface. These findings were also confirmed for unbonded PT masonry walls, experimentally tested under either quasi-static cyclic (Hassanli et al. 2016a; Kalliontzis and Schultz 2017a; 2017b) or dynamic (Wight et al. 2006) loading. Therefore, using an elastic beam-column element in the current study to represent the wall panel was considered acceptable. However, to account for both shear and flexural deformations in the wall, elastic Timoshenko beam-column elements were used in the model.

### 2.3.2. MATERIAL MODELS

#### 2.3.2.1 MASONRY MATERIAL

The springs at the wall-foundation interface are defined by a material model with zero tensile strength (Concrete01 in OpenSees) that exhibits stiffness degradation upon unloading and reloading, in addition defines strains corresponding to maximum and crushing strengths. Hence, the material model can control the descending post-peak slope of the wall load-displacement response to account for any confinement effect, as will be discussed later. The crushing strength is taken as 0.2 $f_m^{'}$, as reported by Kent and Park (1971).

In a subset of the following analyses, to investigate the influence of confinement on the collapse capacity of PT-CRMWs, confining plates (Priestley 1982; Priestley and Elder 1983) were assumed to be placed in the bed joints within the $L_p$ of each wall, as shown in Fig. 2.3. These plates were expected to increase the crushing strain capacity and enhance the post-peak softening branch. Accordingly, to account for the influence of confining plates, the confined masonry stress-strain curve that was developed by Priestley and Elder (1983) is used, as presented in Eq. (2.3), (2.4) and (2.5). In those equations, the descending branch slope, $Z_m$, is controlled by enhancing the crushing strain, $\varepsilon_{mp}$, which is a function of the volumetric confining ratio, $\rho_s$, the spacing between the plates, $s_h$, the length of the plates, $h$, the yielding strength of the plates, $f_{ys}$, and the masonry strain corresponding to the masonry compressive strength, $\varepsilon_m$. Considering these

equations, the ratio between the confined and unconfined crushing strains was set as 2.5 as a target to determine the dimensions of the confining plates.

$$Z_m = \frac{0.5}{\left(\frac{3+0.29 f_m^{'}}{145 f_m^{'} - 1000}\right) + 0.75\rho_s \sqrt{\frac{h}{s_h}} - 0.002K} \tag{2.3}$$

$$K = 1 + \rho_s \frac{f_{ys}}{f_m^{'}} \tag{2.4}$$

$$\varepsilon_{mp} = \frac{0.8}{Z_m} + \varepsilon_m \tag{2.5}$$

#### 2.3.2.2 PT MATERIAL

The PT bars were modelled using a Giuffre Menegotto-Pinto steel model (Steel02 in OpenSees) with an initial stress to create the initial prestressing force, $T_o$, applied to the unbonded bars. As mentioned earlier, the PT bars were modeled as truss elements, while a zero-length spring with a tension only gap material was located at the bottom of each PT bar to prevent it from developing any compression forces. During the model validation, the steel model was defined using the yield strength, $f_{py}$, and the strain hardening ratio, $b$, according to the corresponding experimental study, while for the 20 PT-CRMWs archetypes, a constant strain hardening ratio of 1.6% was assumed, as per DSI (2015). In all cases, the initial elastic modulus was taken as 190 GPa and the other constants that control the transition from elastic to plastic zone for PT bars were taken as *R0*=18, *CR1*=0.925, and *CR2*=0.15.

### 2.3.3. MODEL VALIDATION

The numerical model was validated against experimental results from Laursen and Ingham (2001, 2004a, 2004b) and Hassanli et al. (2016a). These experimental

programs were selected because they included different wall types (i.e. unconfined and confined) with wide ranges of aspect ratios and initial prestressing to yielding stress ratios $f_{pi}/f_{py}$, as summarized in Table 2.1. All these walls were fully-grouted rectangular PT-CRMWs, and a two-third scale three-story wall (L3-W1) was confined using confining plates at wall corners only to increase the crushing strain of the wall. For all walls that were used to validate the model, Table 2.1 also summarizes the masonry compressive strength and PT bars configuration. Full details of the experimental programs and test results can be found in Laursen (2002) for walls L1-W3, L1-W5, L2-W5, and L3-W1, and in Hassanli et al. (2016a) for walls H-W2 and H-W3.

For each wall model, the initial post-tensioning force was applied, and then reversed cyclic horizontal displacements were applied at the top of the wall using the loading protocol of the corresponding experimental study. Considering the variability in masonry properties, Fig. 2.4 shows good agreement between the experimental hysteresis loops and the corresponding loops from the numerical model for all six walls. The model is able to capture the peak strength and strength at 80% degradation (when applicable) of all walls very closely, with maximum deviations of 11% and 14%, respectively. Moreover, the model is generally able to simulate the most relevant characteristics of the cyclic response, including initial stiffness, peak strength, stiffness degradation, strength deterioration, and energy dissipation at different drift levels.

Fig. 2.5 compares the experimental and the numerical total PT force-drift relationships for all walls. As can be seen in these figures, the model is able to predict the maximum PT forces at each cycle and the residual PT forces at the end of each cycle with maximum deviations of 19% and 29%, respectively. This agreement is considered acceptable in the current study given the simplicity of the developed model.

### 2.3.4. COLLAPSE CRITERIA

For the analyses in this study, to allow for direct comparison between SMRWs and PT-CRMWs, collapse was defined herein following the GCR 10-917-8 study (NIST 2010) as the point when the wall reaches any one of the following three conditions:

1. Masonry crushing: crushing was considered to occur when 15% of the cross section reached the crushing strain that was taken as 0.01 (NIST 2010), which represents the strain at the end of the descending branch of the typical masonry stress-strain relation.
2. PT bar rupture: fracture of a PT bar was defined by reaching a fracture strain of 0.02, which is one-third of the strain at which a bar reaches its tensile strength [i.e. 0.06 per DSI (2015)]. This low value accounts for both low-cycle fatigue and anchorage stress concentration, which can lead to an early fracture of the PT bar.

3. Shear failure: collapse due to shear-controlled behavior was considered to occur when the shear force in the wall exceeded the nominal shear strength calculated based on MSJC (2013), as presented in Eq. (2.6), (2.7) and (2.8).

$$V_n = \left(V_{nm} + V_{ns}\right)\gamma_g \tag{2.6}$$

$$V_{nm} = 0.083\left[4.0 - 1.75\left(\frac{M_u}{V_u d_v}\right)\right]A_{nv}\sqrt{f_m^{'}} + 0.25P_u \tag{2.7}$$

$$V_{ns} = 0.5\left(\frac{A_v}{s}\right)f_y d_v \tag{2.8}$$

where $V_n$ is the nominal shear strength in N, $V_{nm}$ is the masonry shear contribution in N, $V_{ns}$ is the shear reinforcement contribution in N, $\gamma_g$ is a factor to account for grouting (i.e. 1 for fully grouted), $d_v$ is the shear depth in mm (taken as $0.8L_w$), $M_u$ is the factored moment in N-mm, $V_u$ is the factored shear force in N, $A_{nv}$ is the net shear area in mm$^2$, $f_m^{'}$ is the masonry prism compressive strength in MPa, $P_u$ is factored axial load in N, $A_v$ is the shear reinforcement cross-section area in mm$^2$, $s$ is the shear reinforcement spacing in mm, and $f_y$ is the shear reinforcement yield strength in MPa. In general, the ungrouted portions of the wall due to tendon openings are very small relative to the wall gross cross-section area (less than 1%). As such, no reduction in the wall cross-section area is considered in the current study when the shear strength is evaluated (e.g. Hassanli et al. 2016a; Laursen and Ingham 2001).

## 2.4. PT-CRMW ARCHETYPES

### 2.4.1. WALL CONFIGURATIONS

The current study adopted the same buildings as in NIST GCR 10-917-8 (2010) study to investigate the FEMA P695 methodology (FEMA 2009). In that study, 20 fully-grouted rectangular conventional SRMWs were evaluated for a range of building heights and design parameters in order to cover a wide design space. The considered design variables included the number of stories, the wall aspect ratio, the gravity load level and the seismic design category (SDC). Walls that were designed for one-story buildings were for retail occupancies, while other walls that were designed with 2, 4, 8 and 12 stories were for hotels and residential occupancies. Full details about the plan configurations with all dimensions and the slab load intensities are provided in Appendix A of the GCR 10-917-8 study (NIST 2010).

To facilitate direct comparison, the same 20 SRMWs were redesigned with fully-grouted unbonded PT bars (constant over the height of the wall) using the same seismic performance factor assigned for SRMWs (R = 5). In addition, in each wall, a minimum amount of vertical reinforcement (#4 each 2.0 m) was used over the height of the building to maintain engineering practice requirements according to MSJC (2013). However, this vertical reinforcement was not extended inside the foundation to facilitate the rocking mechanism and the self-centering ability of the wall, and subsequently, it was not considered when the wall lateral resistance was

calculated (Kalliontzis et al. 2019). Table 2.2 summarizes the PT-CRMW dimensions; unconfined masonry compressive strength ( $f'_m$ ); unbonded PT tendons area, diameter ($d_{PT}$); bonded vertical reinforcement ratio ($\rho_v$); and the horizontal reinforcement amount and ratio ($\rho_h$) for all archetypes (S1-CR to S20-CR). The horizontal reinforcement was hooked 180° hook around the outermost vertical reinforcement following the detailing requirements provided by Hassanli et al. (2016a) and Kalliontzis et al. (2019). For the one and two-story archetypes, unbonded PT strands were used, while PT bars were used for the 4, 8 and 12 story archetypes. This is due to the higher yielding strain limit of PT strands compared to PT bars, which allows strands to better accommodate the high change in strains associated with the short unbonded length ($L_{un}$) of the one- and two-story archetypes. The outer diameter of the ducts was 49 mm and 43 mm for the 36 mm and 26 mm prestressed bars, respectively, while for ducts with one, two, and three strands, the outer diameter was 30 mm, 45 mm and 50 mm, respectively. Full anchorage detailing information can be found in DSI (2015). In all cases, $L_{un}$ was taken as the wall height plus 500 mm to account for the anchorage distance and embedded length in the foundation.

The compressive strength of the unconfined masonry, $f'_m$, varied from one archetype to another in the NIST (2010) study, so the same values were used to design and model each corresponding archetype with unbonded PT bars in the current study. In addition, for all walls, the PT ducts in cross section were spaced as shown in Fig. 2.6 for walls S1-CR to S5-CR for illustration. The maximum PT

bar size used in the current study is limited to 36 mm, which is considered acceptably close to the maximum bar size of 35 mm recommended in the commentary to Clause 6.1.2.1 of MSJC (2013). This bar size limit is mainly to ensure that grout has a sufficient volume to flow around the duct with no consolidation. Archetypes were separated in NIST (2010) into eight performance groups with common gravity loads, number of stories, and SDC. The 20 PT-CRMWs were divided into the same eight performance groups, covering a wide range of RM wall systems with different axial load (low and high) levels and SDC ($D_{min}$ and $D_{max}$). Although a minimum of three archetypes is required in each performance group according to the FEMA P695 methodology (FEMA 2009), the same number of archetypes was used in the current study as in the GCR 10-917-8 study (NIST 2010) to facilitate a direct comparison.

### 2.4.2. DESIGN CRITERIA

The PT-CRMWs were designed and detailed in accordance with the requirements of MSJC (2013). For unbonded PT concrete walls, ACI 318-14 (ACI 2014) recommends that PT bars should remain elastic to ensure the self-centering ability of the walls under seismic loading demands. Similarly, all PT-CRMWs in this study were designed to self-center by ensuring that the stress in each PT tendon is always less than the yield strength, $f_{py}$, at the ultimate stage. However, the stress determination of the unbonded PT at the ultimate stage, $f_{ps}$, when masonry reaches the maximum usable strain of 0.0025 (MSJC 2013), is challenging because the PT

bar elongation is affected by local deformation at the wall base. To address this, MSJC (2013) provides Eq. 2.9 to estimate $f_{ps,}$ while previous research studies (Wight and Ingham 2008; Hassanli et al. 2017) have developed Eqs. 2.10 and 2.11, respectively, to estimate $f_{ps}$.

$$f_{ps} = f_{se} + 0.03\left(\frac{E_{ps}}{L_{un}}\right)\left(d - 1.56\frac{A_{ps}f_{ps} + P}{f_m^{'}L_w}\right) \leq f_{py} \quad (2.9)$$

$$f_{ps} = f_{se} + \left(\frac{(h_w/L_w)\varepsilon_{mu}}{30\left(f_m/f_m^{'}\right)}\right)\left(\frac{E_{ps}}{L_{un}}\right)\left(d - \frac{f_m L_w}{\alpha\beta f_m^{'}}\right) \leq f_{py} \quad (2.10)$$

$$f_{ps} = f_{se} + \left(\frac{L_p(\varepsilon_{mu} - \varepsilon_0)}{c}\right)\left(\frac{E_{ps}}{L_{un}}\right)(d - c) \leq f_{py} \quad (2.11)$$

where $f_{se}$ is the effective stress in the PT bar after immediate stress losses, $E_{ps}$ is the PT modulus of elasticity, $d$ is the distance from the bar location to the outermost compression fiber, $A_{ps}$ is the bar cross-section area, $P$ is the gravity load including the wall self-weight, $\varepsilon_{mu}$ is the masonry crushing strain, $\varepsilon_0$ is the masonry strain corresponding to the wall decompression stage when the wall is about to uplift from the foundation, $\alpha$ and $\beta$ are the equivalent stress block parameters (taken as 0.8 as per MSJC 2013), and $c$ is the length of compression zone. According to MSJC (2013), $f_{ps}$ in Eq. 2.9 is equal to $f_{se}$ only for members with unbonded prestressing tendons, and thus the increase in the prestressing stress, due to PT extension during uplift, is neglected. In addition, Eq. 2.9 was based on experimental investigations of PT-MWs in the out-of-plane direction, where a constant wall base rotation of 3% at the ultimate stage was assumed. Conversely, Wight and Ingham (2008) demonstrated that this rotation varied based on the wall aspect ratio and axial stress

ratio, leading to Eq. 2.10. Recently, Hassanli et al. (2017) introduced Eq. 2.11, which considers the effect of axial stress level through $L_p$, and an extensive study was conducted to compare these three equations. The results showed that Eq. 2.11 accurately captured the wall base shear and the PT forces at the peak strength. Therefore, in the current study, Eq. 2.11 was used to calculate the stress in the unbonded PT bars when the nominal flexural strength ($M_n$) was calculated using Eqs. 2.12 and 2.13 for the PT-CRMW archetypes.

$$a = \frac{f_{ps}A_{ps} + P_u / \phi}{0.8 f_m^{'} b} \tag{2.12}$$

$$M_n = f_{ps}A_{ps}(d - a/2) + \frac{P_u}{\phi}(L_w - a/2) \tag{2.13}$$

Where a is the equivalent compression stress block, φ is the strength reduction factor with a value of 0.8, and b is the wall width. The prestress ratio, defined as the ratio of the initial PT stress to the yield strength, $\eta$, was set to be 0.5 for PT bars with a yield strength of 850MPa (DSI 2015), while for the PT strands used in low aspect ratio walls (one- and two-story walls), $\eta$ was taken as 0.25 to avoid premature yielding of the PT strands, with $f_{py}$ of 1680 MPa (DSI 2015).

Table 2.3 presents the seismic design parameters of the PT-CRMWs, including the code-defined estimate of the fundamental period, *T*; the fundamental period of the numerical model, $T_1$; the seismic base shear coefficient, *V/W* (where *V* is the base shear and *W* is the seismic weight); and the MCE spectral acceleration, $S_{MT}$. ASCE/SEI 7-16 (ASCE/SEI 2016) recommends that *T* not exceed the product

of the coefficient for the upper limit on the calculated period, $C_u$, and the approximate fundamental period, $T_a$. In the current study, $T$ was calculated as $C_u$ $T_a$, but subject to the lower bound value of 0.25 sec. as recommended in FEMA P695 (FEMA 2009). Based on this, for all 20 PT-CRMWs archetypes, $T$ was similar to that presented in the GCR 10-917-8 study (NIST 2010) because the formula used is independent of the wall configuration. Eigenvalue analysis was conducted to calculate the values of $T_1$ based on the masonry modulus of elasticity of $900\ f'_m$ as provided by MSJC (2013), and the effective moment of inertia, $I_{eff}$, which was taken as 50% of the uncracked moment of inertias, $I_g$, of the masonry shear wall (NIST 2010). However, for the nonlinear static and dynamic analyses, no stiffness modifier was used because the model directly accounts for non-linearity based on the cracked stiffness and the level of axial load.

## 2.5. NONLINEAR RESPONSE ANALYSES

As recommended by FEMA P695 methodology (FEMA 2009), nonlinear static pushover and nonlinear dynamic analyses were performed on all archetypes. The load combination used in the nonlinear analysis is 1.05 times the specified dead load, $D$, plus 0.25 times the specified live load, $L$ (FEMA 2009).

### 2.5.1. STATIC PUSHOVER ANALYSES

Pushover analyses were conducted using the lateral force design distributions prescribed by ASCE/SEI 41-17 (ASCE/SEI 2017) following the first-mode shape and mass distribution. The pushover analysis was used to compute the period-based

ductility, $\mu_T$, and the overstrength factor, $\Omega$. The period-based ductility, $\mu_T$, is defined in Eq. (2.14) as the ratio between the roof drift corresponding to a 20% reduction in base shear, $\delta_u$, and the effective yielding drift of the roof, $\delta_{y,eff}$. The effective yielding drift is calculated according to Eq. (2.15), where $C_o$ is a coefficient that accounts for the difference between the roof displacement of a multiple-degree-of-freedom system and the displacement of an equivalent single-degree-of-freedom system. Using the ordinate of the first mode shape at the roof ($\phi_{1,r}$) and the first modal mass participation ratio ($\Gamma_1$), the coefficient $C_o$ is calculated using Eq. (2.16). In Eq. (2.15), $W$ is the building seismic weight, $V_{\max}$ is the maximum base shear determined from the pushover curve, and $g$ is the acceleration due to gravity. The overstrength factor, $\Omega$, is defined in Eq. (2.17) as the ratio of the maximum base shear, $V_{\max}$, to the design base shear, $V_d$.

$$\mu_T = \frac{\delta_u}{\delta_{y,eff}} \tag{2.14}$$

$$\delta_{y,eff} = C_o \frac{V_{\max} \times g}{W \times 4\pi^2} \max(T_1, T)^2 \tag{2.15}$$

$$C_o = \phi_{1,r} \Gamma_1 \tag{2.16}$$

$$\Omega = \frac{V_{\max}}{V_d} \tag{2.17}$$

For archetypes S2-CR and S5-CR, Fig. 2.7 compares the pushover curves for SRMWs designed and modeled using nonlinear fiber sections in NIST (2010) to those for PT-CRMWs designed in the current study. As shown in Fig. 2.7, the initial stiffness is essentially identical for both wall types until decompression occurs. However, $\delta_u$ of walls S2-CR and S5-CR is approximately 320% higher and

56% lower than for the fixed base walls S2 and S5 designed in NIST (2010), respectively. The primary reason for this low $\delta_u$ value of wall S5-CR is the high axial stress level resulting from the PT bars, which leads to premature wall toe crushing at an early drift demand.

Although the two wall types were designed to have similar lateral strength, Fig. 2.7 and Table 2.4 show that the overstrength factor, $\Omega$, for PT-CRMWs is on average less than that of SRMWs designed in NIST (2010). This is attributed to the distribution of the vertical reinforcement in SRMWs, allowing multiple bars to yield and reach hardening, whereas the PT-CRMWs had concentrated PT bars close to the wall centerline. In addition, the ratio between the ultimate and yield strengths ($f_{pu}/f_{py}$) of PT tendons used in the current study is approximately 1.15, while the same ratio ($f_u/f_y$) is approximately 1.5 for the vertical reinforcement used in SRMWs (NIST 2010).

### 2.5.2. GROUND MOTION SELECTION AND SCALING

Nonlinear dynamic analysis was performed for each archetype using the set of 44 far-field ground motion records (i.e. 22 pairs of horizontal components) selected for the FEMA P695 methodology (FEMA 2009). Fig. 2.8 shows the response spectrum of the 44 ground motions with their scaled median and compared to MCE spectra of SDC $D_{min}$ and $D_{max}$. Following the recommendation given, the ground motion records were normalized by their respective peak ground velocities and then

collectively scaled so that the median value of the records matched the MCE elastic design spectrum at the fundamental code-based period, *T*.

### 2.5.3. MULTIPLE STRIPE ANALYSIS

Dynamic analysis was conducted to calculate the probability of collapse of the 20 PT-CRMWs archetypes at different earthquake intensities using the 44 far-field ground motion records. Dynamic analysis results are presented using the multiple stripe analysis (MSA) method (Jalayer 2003). The MSA allows the fragility parameters to be computed from the observed data by counting the number of collapses at each scaled intensity measure (Baker 2015), thus reducing the number of analyses required compared to incremental dynamic analysis (IDA). All the ground motion records were scaled from 50% to 400% of the MCE at 50% increments, leading to a total of 8 stripes.

Following NIST (2010), initial stiffness-proportional Rayleigh damping was applied. Only the linear elastic frame elements (i.e. neither the PT nor the spring elements) were assigned any stiffness-proportional damping. The Rayleigh damping parameters were calculated for all archetypes using a damping ratio of 5% in the first and third modes ($\omega_1$ and $\omega_3$), except for those with only one or two stories, where $\omega_1$ and $5.0\omega_1$ were used instead. For each wall, the seismic mass of each floor was assigned in the horizontal degree of freedom only, to facilitate a direct comparison with SMRWs that were assigned mass in the same degree of freedom (NIST 2010).

The median collapse spectral intensity, $S_{CT}$, was determined for each archetype assuming a lognormal distribution using the maximum likelihood method (Baker 2015). In addition, for each archetype, the spectral acceleration of the MCE, $S_{MT}$, corresponding to the fundamental code-based period of the archetype, $T$, was determined. According to the FEMA P695 methodology (FEMA 2009), the collapse margin ratio (CMR) was calculated using Eq. (2.18):

$$CMR = \frac{S_{CT}}{S_{MT}} \tag{2.18}$$

The values of CMR, calculated from Eq. (2.18) using the dynamic analyses, are summarized in Table 2.4 for all PT-CRMWs archetypes. The CMR values for SRMWs that were reported in the GCR 10-917-8 study (NIST 2010) are also listed for comparison.

## 2.6. COLLAPSE RISK ASSESSMENT

In the FEMA P695 methodology (FEMA 2009), the performance is assessed through the adjusted collapse margin ratio (ACMR), computed as the product of the spectral shape factor (SSF) and the CMR obtained from the MSA results:

$$ACMR = SSF \times CMR \tag{2.19}$$

The SSF is defined based on the period-based ductility, $\mu_T$, obtained from the pushover analyses, and the fundamental code-based period, $T$. The calculated values of the ACMR are then compared with two acceptable values, which are

given in FEMA P695 (FEMA 2009) in terms of the total system uncertainty, $\beta_{TOT}$, calculated from Eq. (2.20) as

$$\beta_{TOT} = \sqrt{\beta_{RTR}^2 + \beta_{DR}^2 + \beta_{TD}^2 + \beta_{MDL}^2} \tag{2.20}$$

where $\beta_{RTR}$ is the record-to-record uncertainty arising from variations in frequency content of the different ground motions. A value of 0.4 was used for $\beta_{RTR}$ because $\mu_T$ for all PT-CRMW archetypes is greater than 3.0 (FEMA 2009). The factor $\beta_{DR}$ accounts for the robustness and accuracy of the design requirements, which was categorized as B-Good with a $\beta_{DR}$ value of 0.2 (FEMA 2009). The factor $\beta_{TD}$ describes the robustness and quality of the test data that are used to define the system, which was categorized as B-Good with a $\beta_{TD}$ value of 0.2 (FEMA 2009). Finally, $\beta_{MDL}$ represents the uncertainty associated with the numerical models, which depends on how well the model predicts the structural collapse behavior. The model uncertainty was categorized as B-Good with a $\beta_{MDL}$ value of 0.2 (FEMA 2009). The values of $\beta_{DR}$, $\beta_{TD}$ and $\beta_{MDL}$ are identical to those used in the NIST (2010) study. Based on the above, the $\beta_{TOT}$ was calculated as 0.529.

FEMA P695 (FEMA 2009) identifies two acceptable ACMR values: 1) $ACMR_{20\%}$, which is taken as 1.56 to ensure a probability of collapse less than 20% for each individual archetype within a performance group; and 2) $ACMR_{10\%}$, which is taken as 1.96 to ensure a probability of collapse less than 10% on average across a performance group. Both acceptable values must be satisfied to pass the methodology (FEMA 2009).

## 2.7. PERFORMANCE EVALUATION RESULTS

### 2.7.1. COLLAPSE RISK OF WALLS WITHOUT CONFINEMENT

The results of the performance evaluation are shown in Table 2.5, where the ACMR values for all archetypes are compared with the acceptable ACMR for both PT-CRMW and SRMW systems. Although both systems were designed using the same *R* value, the ACMR values calculated for PT-CRMWs were acceptable for performance groups 1S, 3S, 5S and 7S, representing short-period archetypes (low-rise walls), while the ACMR values were not acceptable for SRMWs in the same performance groups. Conversely, for performance groups 2S, 4S, 6S and 8S with long-period archetypes (high-rise walls), SRMWs satisfied the acceptance criteria of the methodology, while PT-CRMWs did not fully meet the acceptance criteria. Collapse of these high-rise walls was mainly governed by a shear failure, where the base shear force exceeded the corresponding diagonal shear strength presented in Eq. 2.6, before either the masonry crushing strain or the PT fracture strain was reached, as described in detail below.

Fig. 2.9 shows the shear and moment envelopes from the dynamic analysis for walls S1-CR through S5-CR at scaling factors of 1, 2 and 3 relative to the MCE level using one ground motion record (Imperial Valley 1979) for illustration. As shown in Fig. 2.9, the shear and moment envelopes for walls S1-CR, S2-CR and S3-CR are largest at the base and do not greatly exceed the respective capacities. However, the shear and moment envelopes for walls S4-CR and S5-CR exceed the

shear and flexural strengths of the walls, despite the formation of the nonlinear mechanism at the wall-foundation rocking joints. This is because of higher mode effects, which allow the moment and shear envelopes to increase even after the moment at the wall base has been limited by rocking or yielding, particularly for taller walls (Sullivan et al. 2008; Rutenberg 2011; Wiebe and Christopoulos 2015). In this regard, the PT-CRMWs were modeled in the current study using an elastic element coupled with lumped plasticity nonlinear springs at the base. Although this modeling approach represents the intended behavior of rocking systems, with damage expected only at the wall-foundation interface, this does not allow for the formation of plastic hinges along the wall height to limit the higher mode effects. Conversely, the higher mode effects are expected to be much less significant in the SRMWs reported by GCR 10-917-8 (NIST 2010) because they were modeled using nonlinear elements with fiber sections, allowing for the possibility of additional plastic hinges above the wall base (Ghorbanirenani et al. 2012).

To illustrate the system performance if shear failure were prevented, such as by increasing the shear capacity or mitigating higher mode effects (Wiebe et al. 2013), Fig. 2.10 is used to compare the collapse fragility curves for walls S1-CR, S2-CR, S3-CR, S4-CR, and S5-CR considering all three collapse criteria described above to those with shear failure excluded (SFE). These collapse fragility curves were developed by counting the number of collapses that occurred for each of the 8 stripes (Baker 2015). As can be seen in Fig. 2.10, the $S_{CT}$ values are 5%, 16% and 98% higher for S3-CR, S4-CR and S5-CR, respectively, compared to the same

walls when all collapse criteria are considered (ACC). Consequently, the ACMR for wall S5-CR reached a value of 2.04 when shear failure was excluded (SFE), indicating that the wall performance was enhanced enough to pass the FEMA P695 methodology. Moreover, Fig. 2.10 confirms that the influence of shear failure because of higher mode effects is severe on high-rise walls, such as S5-CR, with almost no influence on low-rise walls such as S1-CR and S2-CR.

Regarding the influence of the gravity load level on the CMR, Table 2.5 shows that most of the walls with low gravity load had lower CMRs compared to those with high gravity loads. This is because the amount of PT tendons required for walls with low gravity load is greater than for walls with high gravity load in order to achieve the desired strength. This, in turn, increases the compression demand on the wall toes as the wall rocks, leading to the crushing strain being reached at a smaller base rotation.

Finally, the overstrength factor ($\Omega$) for PT-CRMWs is taken as the largest average value of the mean overstrength factor calculated for each performance group based on the pushover analyses discussed earlier, as per FEMA P695 (FEMA 2009). Thus, based on the results in Table 2.5, the value of $\Omega$ is 1.91. This is smaller than the value of 2.5 currently provided in ASCE/SEI 7-16 (ASCE/SEI 2016) for SRMWs.

### 2.7.2. INFLUENCE OF CONFINEMENT

Fig. 2.10 also compares the collapse fragility curves of walls S1-CR, S2-CR, S3-CR, S4-CR, and S5-CR for walls with confined masonry response when all collapse criteria are considered (confined ACC). The fragility curves are represented by the lognormal cumulative distribution because this is a common assumption in earthquake engineering, though this could also be checked using routine statistical analysis techniques (e.g., Chi-Square test or Kolmogrov-Smirnov goodness fit test). As can be seen in Fig. 2.10, $S_{CT}$ is increased by 19%, 24% and 18% relative to the unconfined walls S1-CR, S3-CR and S4-CR, respectively, when confinement is introduced. This is because the larger masonry crushing strain of confined walls delays the collapse of these walls, and thus has the potential to minimize the collapse risk under high seismic demands. However, S2-CR and S5-CR did not show any enhancement. For S2-CR, this is because the collapse was governed mainly by PT fracture, which is not avoided by adding confinement. For S5-CR, the collapse was governed mainly by shear failure due to the high shear demands caused by higher mode effects, which implies that confinement could be an effective strategy for S5-CR only if shear failure is prevented.

Finally, Fig. 2.10 also shows the fragility curves for walls S1-CR to S5-CR if shear failure is excluded and confinement is also used (confined SFE). In this case, the $S_{CT}$ values are 23%, 42%, 46% and 260% higher for walls S1-CR, S3-CR, S4-CR and S5-CR, respectively, compared to similar unconfined walls when all collapse

criteria are considered (unconfined ACC). In all cases except S2-CR, the combination of preventing shear failure and providing confinement to the rocking toe is enough to satisfy the acceptance criteria of FEMA P695 (FEMA 2009) for the PT-CRMW system.

## 2.8. CONCLUSIONS

This study evaluated the collapse risk of PT-CRMWs at the MCE level when the seismic performance factors that are currently assigned to SRMWs are adopted. In this respect, 20 PT-CRMW archetypes were evaluated using the FEMA P695 (FEMA 2009) methodology through multi-spring models developed using OpenSees. The experimentally validated models achieved the methodology requirements in terms of simulating the wall stiffness degradation, lateral strength, inelastic deformation and P-delta effects. Using these models, nonlinear pushover and dynamic analyses were performed to evaluate the overstrength, $\Omega$, period-based ductility, $\mu_T$, and median collapse capacity, $S_{CT}$, for all walls.

The GCR 10-917-8 study (NIST 2010) demonstrated that one- and two-story SRMW archetypes designed using $R$ = 5.0 had a CMR that did not limit the probability of collapse under the MCE level to less than 20%, and hence did not fully meet the acceptance criteria of the FEMA P695 methodology (FEMA 2009). Conversely, the results in the current study demonstrated that the $R$ factor currently assigned to PT-CRMWs (i.e. $R$ = 1.5) is conservative for low-rise walls without or

with confining plates, as using an *R* factor of 5 fully satisfied the acceptance criteria of the methodology.

Considering PT-CRMW archetypes with 8 and 12 stories, an *R* value of 5 did not fully meet the acceptance criteria of the methodology due to higher mode effects, which enlarged the shear and flexural demands on the wall relative to the design values. This was attributed to the use of an elastic wall element, which did not allow for the spread of nonlinearity along the wall height to limit these effects. However, the results demonstrated that these archetypes could pass the methodology with an *R* value of 5 if shear failure was prevented and confinement provided to the rocking toe. In this respect, a further investigation using wall systems with multiple rocking joints to mitigate higher mode effects is recommended. Additional studies also are still needed to investigate the influence of energy dissipation devices on the collapse risk and the self-centering ability of fully- and partially-grouted post-tensioned controlled rocking masonry walls.

## 2.9. ACKNOWLEDGMENTS

The financial support for this project was provided through the Canadian Concrete Masonry Producers Association (CCMPA), the Canada Masonry Design Centre (CMDC), the Natural Sciences and Engineering Research Council (NSERC) and the Ontario Centres of Excellence (OCE).

## 2.10. REFERENCES

Aaleti, S. and Sritharan, S. (2011). "Performance Verification of the PreWEC Concept and Development of Seismic Design Guidelines." ISU-CCEE Report, 02/11 Iowa State University.

ACI (American Concrete Institute). (2014). "Building code requirements for structural concrete." ACI 318-14, Farmington Hills, MI.

ASCE/SEI (Structural Engineering Institute). (2017). "Seismic evaluation and retrofit of existing buildings." ASCE/SEI 41-17, Reston, VA.

ASCE/SEI (Structural Engineering Institute). (2016). "Minimum design loads for buildings and other structures." ASCE/SEI 7-16, Reston, VA.

Atkinson, R. H., and Kingsley, G. R. (1985). "A comparison of the behavior of clay and concrete masonry in compression." Rep. No. 1.1-1, U.S.-Japan Coordinated Program for Masonry Building Research, Atkinson-Noland & Associates, Boulder, CO.

Baker J. (2015). "Efficient analytical fragility function fitting using dynamic structural analysis." Earthquake Spectra, 31(1), 579–599

DSI (DYWIDAG Systems International). (2015). DYWIDAG Post-Tensioning System using Bars.

FEMA. (2009). "Quantification of building seismic performance factors." FEMA P695, Washington, DC.

Ghorbanirenani, I., Tremblay, R., Léger, P., and Leclerc, M. (2012). "Shake table testing of slender RC shear walls subjected to eastern North America seismic ground motions." Journal of Structural Engineering, 138(12), 1515‑1529.

Hassanli, R., ElGawady, M., and Mills, J. (2015). "Plastic hinge length of unbonded post-tensioned masonry walls." 12th North American Masonry Conference, Denver.

Hassanli, R., ElGawady, M., and Mills, J. (2016a). "Experimental investigation of in-plane cyclic response of unbonded-posttensioned masonry walls." Journal of Structural Engineering, 142(5), 04015171-1-15.

Hassanli, R., ElGawady, M., and Mills, J. (2016b). "Force–displacement behavior of unbonded post-tensioned concrete walls." Engineering Structures, 106, 495–505.

Hassanli, R., ElGawady, M., and Mills, J. (2017). "Simplified approach to predict the flexural strength of self-centering masonry walls." Engineering Structures, 142, 255–271.

Henry, R. S., Brooke, N. J., Sritharan, S., and Ingham, J. M. (2012). "Defining concrete compressive strain in unbonded post-tensioned walls." ACI Journal, 109(1), 101-112.

Holden, T., Restrepo, J., Mander, J. B. (2003). "Seismic performance of precast reinforced and prestressed concrete walls." Journal of Structural Engineering,

129(3), 286-296.

Jalayer, F. (2003). "Direct probabilistic seismic analysis: implementing non-linear dynamic assessments." PhD Thesis, Department of Civil and Environmental Engineering, Stanford University.

Kalliontzis, D., and Schultz, A. E. (2017a). "Characterizing the In-Plane Rocking Response of Masonry Walls with Unbonded Posttensioning." Journal of Structural Engineering, 143(9), 04017110.

Kalliontzis, D., and Schultz, A. E. (2017b). "Improved estimation of the reverse-cyclic behavior of fully-grouted masonry shear walls with unbonded post-tensioning." Engineering Structures, 145, 83–96.

Kalliontzis, D., Sritharan, S., and Schultz, A. E. (2019). "Improving Performance of Unbonded Post-Tensioned Masonry Walls with the Use of Rubber Interface" 13th North American Masonry Conference, Salt Lake City.

Kent, D.C., and Park, R. (1971). "Flexural members with confined concrete." Journal of the Structural Division, Proc. of the American Society of Civil Engineers, 97(ST7), 1969-1990.

Laursen, P. T. and Ingham, J. M. (2001). "Structural Testing of Single-Storey Post-Tensioned Concrete Masonry Walls." The Professional Journal of The Masonry Society, 19(1), 69-82.

Laursen, P. T. and Ingham, J. M. (2004a). "Structural testing of enhanced post-

tensioned concrete masonry walls." ACI Journal, 101(6), 852-862.

Laursen, P. T. and Ingham, J. M. (2004b). "Structural testing of large-scale posttensioned concrete masonry walls." Journal of Structural Engineering, 130(10), 1497-1505.

Laursen, P. T. (2002). "Seismic analysis and design of post-tensioned concrete masonry walls." PhD Thesis, Department of Civil and Environmental Engineering, University of Auckland.

McKenna, F., Fenves, G. L., and Scott, M. H. (2000). "Open system for earthquake engineering simulation." University of California, Berkeley, CA.

MSJC (Masonry Standards Joint Committee). (2013). "Building code requirements for masonry structures." TMS 402-13/ASCE 5-13/ACI 530-13, ASCE, Reston, VA.

NIST (National Institute of Standards and Technology). (2010). "Evaluation of the FEMA P695 methodology for quantification of building seismic performance factors." NIST GCR 10-917-8, Gaithersburg, MD.

Paulay, T. and Priestley, M. (1992). Seismic design of reinforced concrete and masonry buildings, Wiley, New York.

Pennucci, D., Calvi, G. M., and Sullivan, T. J. (2009). "Displacement-based design of precast walls with additional dampers." Journal of Earthquake Engineering, 13(1), 40-65.

Priestley, M. J. N., Sritharan, S., Conley, J. R., and Pampanin, S. (1999). "Preliminary results and conclusions from the PRESSS five-story precast concrete test building." PCI Journal, 44(6), 42-67.

Priestley, M. J. N. (1982). "Ductility of confined concrete masonry shear walls." Bulletin of the New Zealand National Society for Earthquake Engineering, 15(1), 22-26.

Priestley, M. J. N. and Elder, D. M. (1983). "Stress-strain curves for unconfined and confined concrete masonry." ACI Journal, 80(19), 192-201.

Priestley, N., Calvi, G., and Kowalsky, M. (2007). Displacement-based seismic design of structures, Istituto Universitario di Studi Superiori (IUSS), Pavia, Italy.

Rutenberg, A. (2011). "Seismic shear forces on RC walls: review and bibliography." Bulletin of Earthquake Engineering, 11(5),1726‑1751.

Sullivan, T. J., Priestley, M. J. N., and Calvi, G. M. (2008). "Estimating the higher-mode response of ductile structures." Journal of Earthquake Engineering, 12, 456–472.

Thomas, D. J., and Sritharan, S. (2004). "An evaluation of seismic design guidelines proposed precast jointed wall systems." ISU-ERI-Ames Rep. ERI-04643, Dept. of Civil, Construction, and Environmental Engineering, Iowa State Univ., Ames, IA.

Watkins, J., Henry, R. S., and Sritharan, S. (2013). "Computational modelling of self-centering precast concrete walls." 4th ECCOMAS Thematic Conference on Computational Methods in Structural Dynamics and Earthquake Engineering, Kos, Greece.

Wiebe, L., Christopoulos, C., Tremblay, R., and Leclerc, M. (2013). "Mechanisms to limit higher mode effects in a controlled rocking steel frame. 2: Large-amplitude shake table testing." Earthquake Engineering & Structural Dynamics, 42(7), 1069-1086.

Wiebe, L., and Christopoulos, C. (2015). "A cantilever beam analogy for quantifying higher mode effects in multistorey buildings." Earthquake Engineering & Structural Dynamics, 44(11), 1697-1716.

Wight, G. D., Ingham, J. M., and Kowalsky, M. J. (2006). "Shaketable Testing of Rectangular Post-Tensioned Concrete Masonry Walls." PCI Journal, 103(4), 587-595.

Wight, G. D., and Ingham, J. M. (2008). "Tendon Stress in Unbonded Posttensioned Masonry Walls at Nominal In-Plane Strength." Journal of Structural Engineering, 134(6), 938-946.

## 2.11. TABLES

**Table 2.1.** Wall Dimensions and Properties for the Model Validation

| Reference | Wall ID | Height (mm) | Length (mm) | Aspect Ratio | Thickness (mm) | $f_m^{'}$ (MPa) | PT bars | $f_{pi}/f_{py}$ | $f_{py}$ (MPa) | Spacing (mm) | $d_{PT}$ (mm) |
|---|---|---|---|---|---|---|---|---|---|---|---|
| Laursen (2002) | L1-W3 | 2800 | 3000 | 0.93 | 140 | 20.6 | 2 | 0.78 | 970 | 800 | 23.0 |
| | L1-W5 | 2800 | 1800 | 1.55 | 140 | 20.5 | 2 | 0.55 | 970 | 800 | 23.0 |
| | L2-W5 | 2800 | 3000 | 0.93 | 140 | 12.5 [a] | 2 | 0.76 | 970 | 800 | 23.0 |
| | L3-W1 | 5250 | 2400 | 2.18 | 140 | 17.9 | 3 [b] | 0.62 | 1520 | 400 | 15.2 |
| Hassanli et al. (2016) | H-W2 | 2300 | 1400 | 1.64 | 190 | 17.5 | 3 | 0.42 | 900 | 600 | 20.0 |
| | H-W3 | 2300 | 1400 | 1.64 | 190 | 17.5 | 4 | 0.32 | 900 | 400 | 20.0 |

[a] High strength blocks made of steel fiber reinforced concrete with cube crushing strength of 131 MPa were used at the base corners.
[b] PT strands were used in this wall instead of bars.

**Table 2.2.** Dimensions and Reinforcement Details of PT-CRMWs

| Archetype ID | Height (mm) | Length (mm) | Nominal Thickness (mm) | $f_m^{'}$ (MPa) | PT Area ($mm^2$) | $d_{PT}$ (mm) | $\rho_v$ (%) | Horizontal RFT (mm) | $\rho_h$ (%) |
|---|---|---|---|---|---|---|---|---|---|
| S1-CR | 3657 | 7315 | 203 | 10.34 | 5x124 | 14.2* | 0.046 | #5@1,220 | 0.085 |
| S2-CR | 6096 | 9754 | 203 | 17.23 | 4x140 | 15.2* | 0.041 | #6@800 | 0.180 |
| S3-CR | 12192 | 9754 | 203 | 20.68 | 2x551 | 26.0 | 0.041 | #5@800 | 0.127 |
| S4-CR | 24384 | 9754 | 203 | 17.23 | 4x1018 | 36.0 | 0.041 | #4@800 | 0.082 |
| S5-CR | 36576 | 9754 | 305 | 20.68 | 7x1018 | 36.0 | 0.026 | 2 × #4@800 | 0.107 |
| S6-CR | 3657 | 7315 | 203 | 13.78 | 5x140 | 15.2* | 0.046 | #5@1,220 | 0.085 |
| S7-CR | 6096 | 9754 | 203 | 13.78 | 5x140 | 15.2* | 0.041 | #5@800 | 0.127 |
| S8-CR | 12192 | 9754 | 203 | 20.68 | 3x551 | 26.0 | 0.041 | #5@800 | 0.127 |
| S9-CR | 24384 | 9754 | 203 | 20.68 | 2x1018 | 36.0 | 0.041 | #5@800 | 0.127 |
| S10-CR | 36576 | 9754 | 305 | 20.68 | 7x1018 | 36.0 | 0.026 | 2 × #4@800 | 0.107 |
| S11-CR | 3657 | 7315 | 203 | 10.34 | 5x124 | 14.2* | 0.046 | #5@1,220 | 0.085 |
| S12-CR | 6096 | 9754 | 203 | 17.23 | 6x140 | 15.2* | 0.041 | #4@800 | 0.082 |
| S13-CR | 12192 | 9754 | 203 | 13.78 | 4x1018 | 36.0 | 0.041 | #6@800 | 0.180 |
| S14-CR | 24384 | 9754 | 203 | 13.78 | 10x1018 | 36.0 | 0.041 | #4@800 | 0.082 |
| S15-CR | 36576 | 9754 | 305 | 20.68 | 16x1018 | 36.0 | 0.026 | 2 × #4@1,220 | 0.072 |
| S16-CR | 3657 | 7315 | 203 | 13.78 | 5x140 | 15.2* | 0.046 | #5@1,220 | 0.085 |
| S17-CR | 6096 | 9754 | 203 | 13.78 | 8x140 | 15.2* | 0.041 | #5@800 | 0.127 |
| S18-CR | 12192 | 9754 | 203 | 13.78 | 5x1018 | 36.0 | 0.041 | #6@800 | 0.180 |
| S19-CR | 24384 | 9754 | 203 | 13.78 | 10x1018 | 36.0 | 0.041 | #4@800 | 0.082 |
| S20-CR | 36576 | 9754 | 305 | 13.78 | 16x1018 | 36.0 | 0.026 | 2 × #4@1,220 | 0.072 |

* Strands are used.

**Table 2.3.** Summary of PT-CRMW Archetypes Design Parameters and Performance Groups

| Archetype ID | Archetype design parameters | | | | | | |
|---|---|---|---|---|---|---|---|
| | Number of stories | Gravity loads | SDC | T (s) | $T_1$ (s) | V/W (g) | $S_{MT}$ (g) |
| Performance group number PG-1S (Short period domain) | | | | | | | |
| S1-CR | 1 | High | $D_{max}$ | 0.25 | 0.18 | 0.200 | 1.50 |
| S2-CR | 2 | High | $D_{max}$ | 0.26 | 0.14 | 0.200 | 1.50 |
| S3-CR | 4 | High | $D_{max}$ | 0.45 | 0.22 | 0.200 | 1.50 |
| Performance group number PG-2S (Long period domain) | | | | | | | |
| S4-CR | 8 | High | $D_{max}$ | 0.75 | 0.50 | 0.160 | 1.20 |
| S5-CR | 12 | High | $D_{max}$ | 1.02 | 0.86 | 0.118 | 0.89 |
| Performance group number PG-3S (Short period domain) | | | | | | | |
| S6-CR | 1 | High | $D_{min}$ | 0.25 | 0.18 | 0.100 | 0.75 |
| S7-CR | 2 | High | $D_{min}$ | 0.28 | 0.20 | 0.100 | 0.75 |
| Performance group number PG-4S (Long period domain) | | | | | | | |
| S8-CR | 4 | High | $D_{min}$ | 0.48 | 0.36 | 0.084 | 0.63 |
| S9-CR | 8 | High | $D_{min}$ | 0.80 | 0.87 | 0.050 | 0.37 |
| S10-CR | 12 | High | $D_{min}$ | 1.09 | 1.47 | 0.037 | 0.28 |
| Performance group number PG-5S (Short period domain) | | | | | | | |
| S11-CR | 1 | Low | $D_{max}$ | 0.25 | 0.18 | 0.200 | 1.50 |
| S12-CR | 2 | Low | $D_{max}$ | 0.26 | 0.14 | 0.200 | 1.50 |
| S13-CR | 4 | Low | $D_{max}$ | 0.45 | 0.27 | 0.200 | 1.50 |
| Performance group number PG-6S (Long period domain) | | | | | | | |
| S14-CR | 8 | Low | $D_{max}$ | 0.75 | 0.61 | 0.160 | 1.20 |
| S15-CR | 12 | Low | $D_{max}$ | 1.02 | 0.84 | 0.118 | 0.89 |
| Performance group number PG-7S (Short period domain) | | | | | | | |
| S16-CR | 1 | Low | $D_{min}$ | 0.25 | 0.18 | 0.100 | 0.75 |
| S17-CR | 2 | Low | $D_{min}$ | 0.28 | 0.20 | 0.100 | 0.75 |
| Performance group number PG-8S (Long period domain) | | | | | | | |
| S18-CR | 4 | Low | $D_{min}$ | 0.48 | 0.45 | 0.084 | 0.63 |
| S19-CR | 8 | Low | $D_{min}$ | 0.80 | 1.10 | 0.050 | 0.37 |
| S20-CR | 12 | Low | $D_{min}$ | 1.09 | 1.85 | 0.037 | 0.28 |

**Table 2.4.** Summary of Analysis Results for Unconfined PT-CRMWs and SRMWs Archetypes

| ArchetypeID | Design configuration | | | Pushover and dynamic analysis results | | | |
|---|---|---|---|---|---|---|---|
| | Number of stories | Gravity loads | SDC | overstrength ($\Omega$) | $S_{MT}$ *(g)* | $S_{CT}$ *(g)* | CMR |
| Performance group number PG-1S | | | | | | | |
| S1-CR | 1 | High | $D_{max}$ | 1.15 (1.84) [a] | 1.50 | 1.78 | 1.19 (0.52) [a] |
| S2-CR | 2 | High | $D_{max}$ | 1.68 (2.28) [a] | 1.50 | 3.02 | 2.01 (1.14) [a] |
| S3-CR | 4 | High | $D_{max}$ | 1.40 (1.87) [a] | 1.50 | 3.74 | 2.49 (1.55) [a] |
| Performance group number PG-2S | | | | | | | |
| S4-CR | 8 | High | $D_{max}$ | 1.45 (1.89) [a] | 1.20 | 1.49 | 1.29 (1.31) [a] |
| S5-CR | 12 | High | $D_{max}$ | 1.26 (1.61) [a] | 0.89 | 0.62 | 0.72 (1.94) [a] |
| Performance group number PG-3S | | | | | | | |
| S6-CR | 1 | High | $D_{min}$ | 1.71 (1.62) [a] | 0.75 | 1.47 | 1.96 (1.04) [a] |
| S7-CR | 2 | High | $D_{min}$ | 2.10 (2.61) [a] | 0.75 | 2.19 | 2.92 (1.92) [a] |
| Performance group number PG-4S | | | | | | | |
| S8-CR | 4 | High | $D_{min}$ | 1.39 (1.65) [a] | 0.63 | 1.36 | 2.15 (1.65) [a] |
| S9-CR | 8 | High | $D_{min}$ | 1.40 (1.93) [a] | 0.37 | 0.44 | 1.20 (1.63) [a] |
| S10-CR | 12 | High | $D_{min}$ | 1.41 (1.68) [a] | 0.28 | 0.28 | 1.00 (2.07) [a] |
| Performance group number PG-5S | | | | | | | |
| S11-CR | 1 | Low | $D_{max}$ | 1.15 (1.84) [a] | 1.50 | 1.78 | 1.19 (0.52) [a] |
| S12-CR | 2 | Low | $D_{max}$ | 1.43 (1.82) [a] | 1.50 | 3.40 | 2.27 (1.71) [a] |
| S13-CR | 4 | Low | $D_{max}$ | 1.59 (1.73) [a] | 1.50 | 2.72 | 1.81 (1.65) [a] |
| Performance group number PG-6S | | | | | | | |
| S14-CR | 8 | Low | $D_{max}$ | 1.37 (1.59) [a] | 1.20 | 1.36 | 1.14 (1.31) [a] |
| S15-CR | 12 | Low | $D_{max}$ | 1.43 (1.47) [a] | 0.89 | 0.85 | 0.95 (1.94) [a] |
| Performance group number PG-7S | | | | | | | |
| S16-CR | 1 | Low | $D_{min}$ | 1.71 (1.62) [a] | 0.75 | 1.47 | 1.96 (1.04) [a] |
| S17-CR | 2 | Low | $D_{min}$ | 2.03 (1.80) [a] | 0.75 | 2.14 | 2.86 (2.38) [a] |
| Performance group number PG-8S | | | | | | | |
| S18-CR | 4 | Low | $D_{min}$ | 1.52 (1.41) [a] | 0.63 | 1.12 | 1.78 (1.65) [a] |
| S19-CR | 8 | Low | $D_{min}$ | 1.42 (1.22) [a] | 0.37 | 0.43 | 1.16 (1.63) [a] |
| S20-CR | 12 | Low | $D_{min}$ | 1.20 (1.46) [a] | 0.28 | 0.20 | 0.72 (2.13) [a] |

[a] Values for the corresponding Special RM walls reported by GCR 10-917-8 (NIST 2010) study.

**Table 2.5.** Summary of Collapse Risk Performance Evaluation for Unconfined PT-CRMW and SRMW Archetypes

| Archetype ID | Number of stories | Computed overstrength and collapse margin parameters | | | | | Acceptance check | |
|---|---|---|---|---|---|---|---|---|
| | | overstrength ($\Omega$) | CMR | period based ductility ($\mu_T$) | SSF | ACMR | Acceptable ACMR | Pass/Fail |
| | | | | Performance group number PG-1S | | | | |
| S1-CR | 1 | 1.15 (1.84) [a] | 1.19 (0.52) [a] | 25.71(5.20) [a] | 1.33 | 1.58(0.66) [a] | 1.56 | Pass(Fail) [a] |
| S2-CR | 2 | 1.68 (2.28) [a] | 2.01 (1.14) [a] | 35.80(8.10) [a] | 1.33 | 2.67(1.52) [a] | 1.56 | Pass(Fail) [a] |
| S3-CR | 4 | 1.40 (1.87) [a] | 2.49 (1.55) [a] | 18.48(11.80) [a] | 1.33 | 3.31(2.06) [a] | 1.56 | Pass(Pass) [a] |
| **Mean of PG-1S** | | **1.41(2.00)** [a] | | | | **2.52(1.41)** [a] | 1.96 | **Pass(Fail)** [a] |
| | | | | Performance group number PG-2S | | | | |
| S4-CR | 8 | 1.45 (1.89) [a] | 1.29 (1.31) [a] | 7.61(6.40) [a] | 1.37 | 1.76(1.76) [a] | 1.56 | Pass(Pass) [a] |
| S5-CR | 12 | 1.26 (1.61) [a] | 0.72 (1.94) [a] | 10.48(14.60) [a] | 1.47 | 1.05(2.84) [a] | 1.56 | Fail(Pass) [a] |
| **Mean of PG-2S** | | **1.36(1.75)** [a] | | | | **1.40(2.30)** [a] | 1.96 | **Fail(Pass)** [a] |
| | | | | Performance group number PG-3S | | | | |
| S6-CR | 1 | 1.71 (1.62) [a] | 1.96 (1.04) [a] | 45.28(13.30) [a] | 1.14 | 2.23(1.19) [a] | 1.56 | Pass(Fail) [a] |
| S7-CR | 2 | 2.10 (2.61) [a] | 2.92 (1.92) [a] | 33.20(14.40) [a] | 1.14 | 3.33(2.18) [a] | 1.56 | Pass(Pass) [a] |
| **Mean of PG-3S** | | **1.91(2.12)** [a] | | | | **2.78(1.69)** [a] | 1.96 | **Pass(Fail)** [a] |
| | | | | Performance group number PG-4S | | | | |
| S8-CR | 4 | 1.39 (1.65) [a] | 2.15 (1.65) [a] | 31.35(28.40) [a] | 1.14 | 2.45(1.88) [a] | 1.56 | Pass(Pass) [a] |
| S9-CR | 8 | 1.40 (1.93) [a] | 1.20 (1.63) [a] | 23.98(7.10) [a] | 1.20 | 1.44(2.03) [a] | 1.56 | Fail(Pass) [a] |
| S10-CR | 12 | 1.41 (1.68) [a] | 1.00 (2.07) [a] | 14.03(16.00) [a] | 1.27 | 1.27(2.84) [a] | 1.56 | Fail(Pass) [a] |
| **Mean of PG-4S** | | **1.40(1.75)** [a] | | | | **1.72(2.25)** [a] | 1.96 | **Fail(Pass)** [a] |
| | | | | Performance group number PG-5S | | | | |
| S11-CR | 1 | 1.15 (1.84) [a] | 1.19 (0.52) [a] | 23.87(5.20) [a] | 1.33 | 1.58(0.66) [a] | 1.56 | Pass(Fail) [a] |
| S12-CR | 2 | 1.43 (1.82) [a] | 2.27 (1.71) [a] | 35.49(8.30) [a] | 1.33 | 3.02(2.27) [a] | 1.56 | Pass(Pass) [a] |
| S13-CR | 4 | 1.59 (1.73) [a] | 1.81 (1.65) [a] | 11.63(11.30) [a] | 1.33 | 2.41(2.19) [a] | 1.56 | Pass(Pass) [a] |
| **Mean of PG-5S** | | **1.39(1.80)** [a] | | | | **2.34(1.71)** [a] | 1.96 | **Pass(Fail)** [a] |
| | | | | Performance group number PG-6S | | | | |
| S14-CR | 8 | 1.37 (1.59) [a] | 1.14 (1.31) [a] | 7.57(13.60) [a] | 1.37 | 1.56(1.82) [a] | 1.56 | Pass(Pass) [a] |
| S15-CR | 12 | 1.43 (1.47) [a] | 0.95 (1.94) [a] | 10.33(42.80) [a] | 1.47 | 1.40(2.84) [a] | 1.56 | Fail(Pass) [a] |
| **Mean of PG-6S** | | **1.40(1.53)** [a] | | | | **1.48(2.33)** [a] | 1.96 | **Fail(Pass)** [a] |
| | | | | Performance group number PG-7S | | | | |
| S16-CR | 1 | 1.71 (1.62)[a] | 1.96 (1.04) [a] | 48.87(13.30) [a] | 1.14 | 2.23(1.19) [a] | 1.56 | Pass(Fail) [a] |
| S17-CR | 2 | 2.03 (1.80)[a] | 2.86 (2.38) [a] | 40.12(14.40) [a] | 1.14 | 3.26(2.71) [a] | 1.56 | Pass(Pass) [a] |
| **Mean of PG-7S** | | **1.87(1.71)** [a] | | | | **2.75(1.95)** [a] | 1.96 | **Pass(Fail)** [a] |
| | | | | Performance group number PG-8S | | | | |
| S18-CR | 4 | 1.52 (1.41)[a] | 1.78 (1.65) [a] | 18.70(29.00) [a] | 1.14 | 2.03(1.88) [a] | 1.56 | Pass(Pass) [a] |
| S19-CR | 8 | 1.42 (1.22)[a] | 1.16 (1.63) [a] | 11.38(17.70) [a] | 1.20 | 1.39(2.05) [a] | 1.56 | Fail(Pass) [a] |

| | | | | | | | | |
|---|---|---|---|---|---|---|---|---|
| S20-CR | 12 | 1.20 (1.46)[a] | 0.72 (2.13) [a] | 9.43(20.70) [a] | 1.27 | 0.91(2.92) [a] | 1.56 | Fail(Pass) [a] |
| **Mean of PG-8S** | | **1.38(1.50)** [a] | | | | **1.45(2.28)** [a] | 1.96 | **Fail(Pass)** [a] |

[a] Values for the corresponding Special RM walls reported by GCR 10-917-8 (NIST 2010) study.

## 2.12. FIGURES

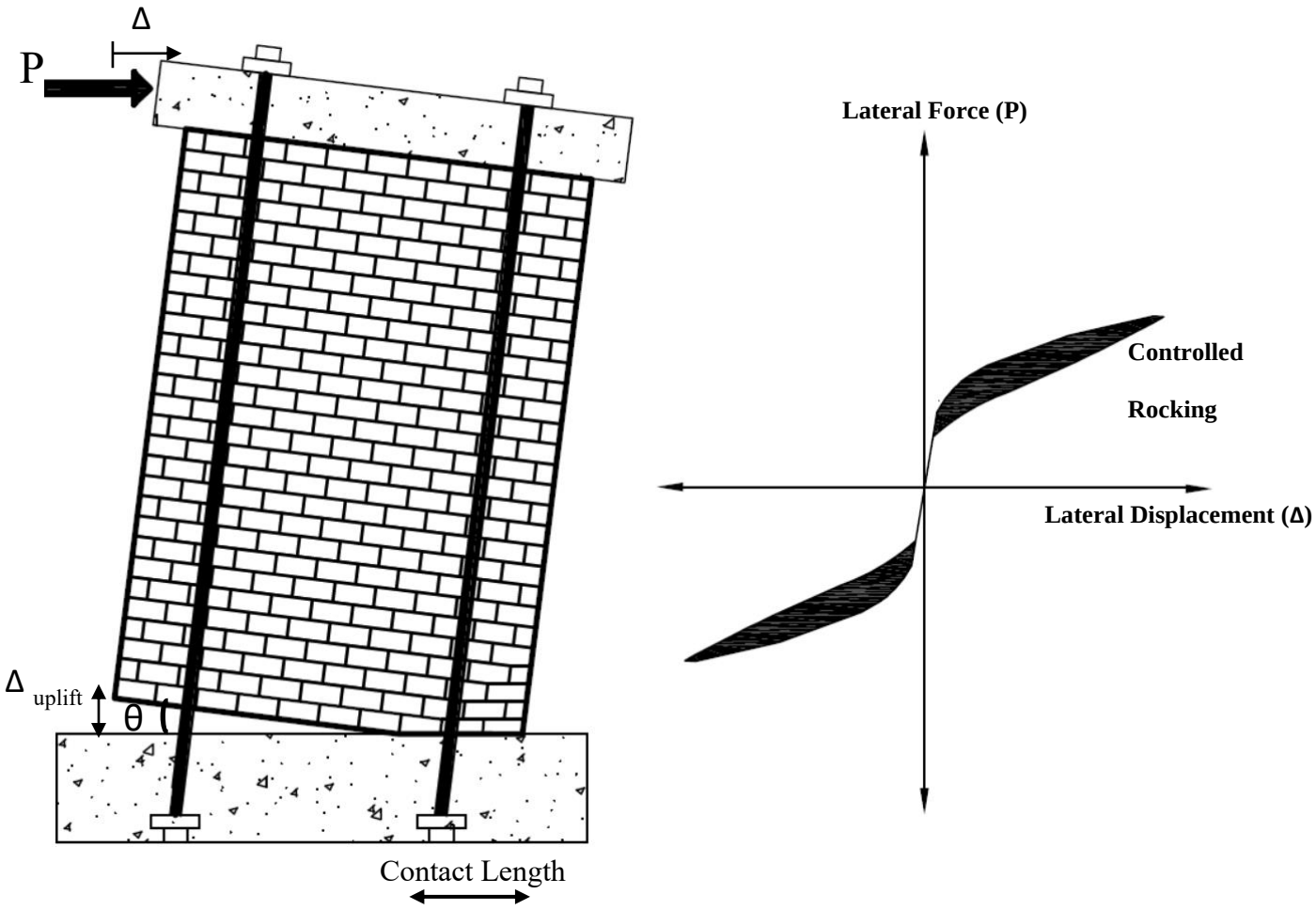


**Fig. 2.1.** Post-tensioned controlled rocking masonry wall response

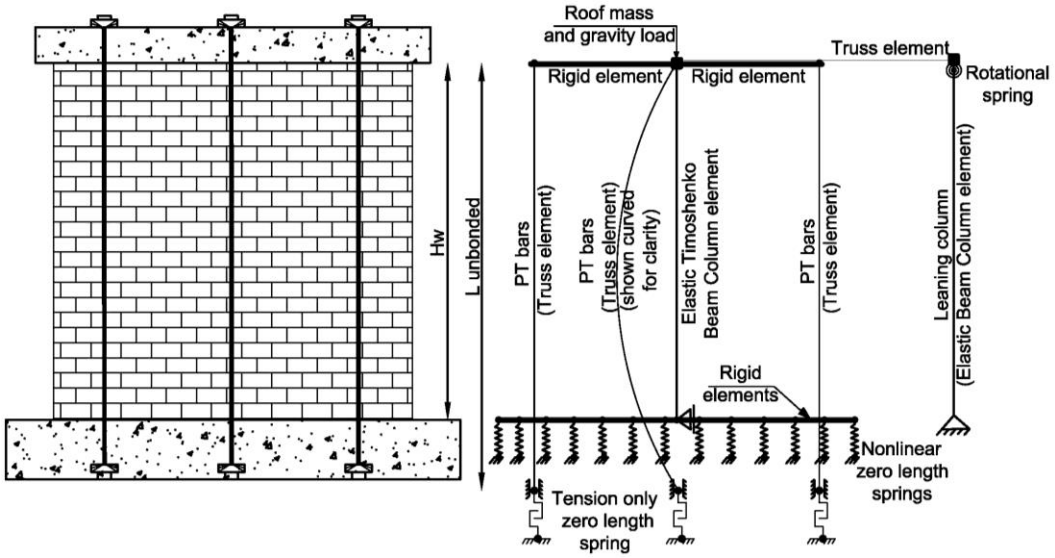


**Fig. 2.2.** Schematic diagram for the model

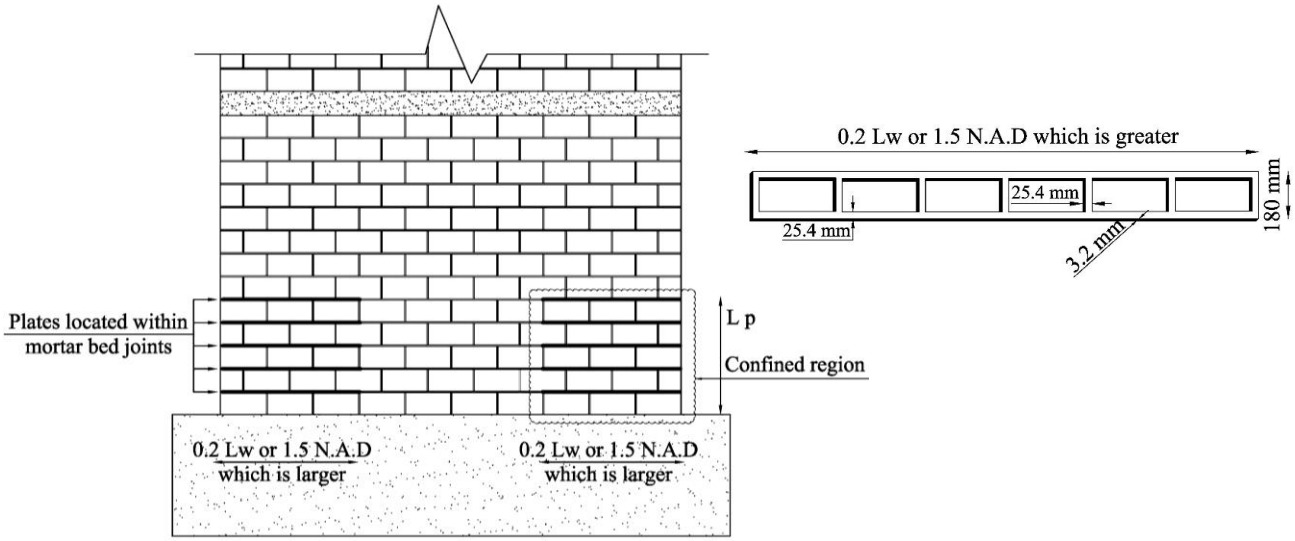


**N.A.D: Neutral Axis Depth**

**Fig. 2.3.** Confining plates detail and configuration

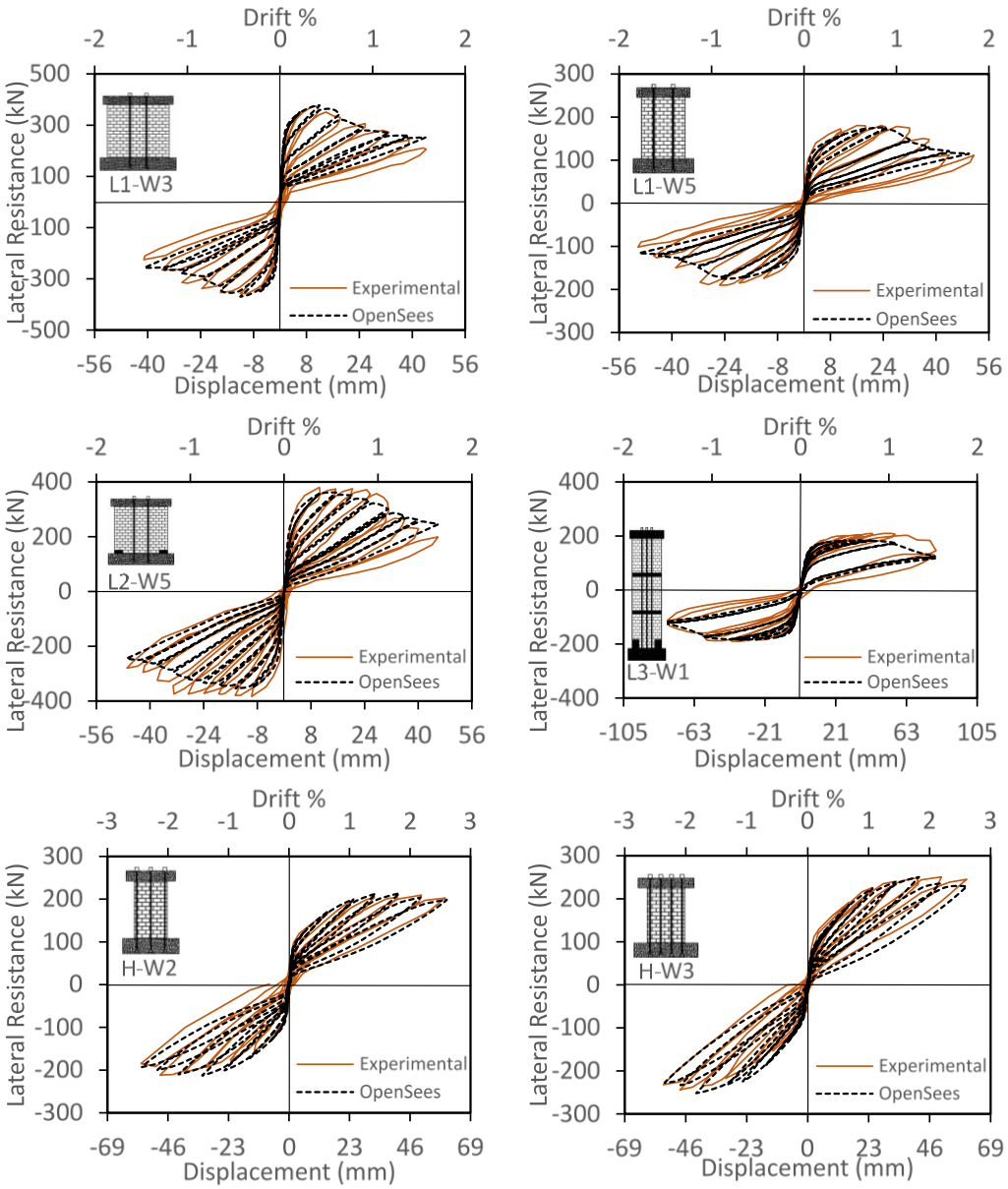


**Fig. 2.4.** Experimental and numerical cyclic responses

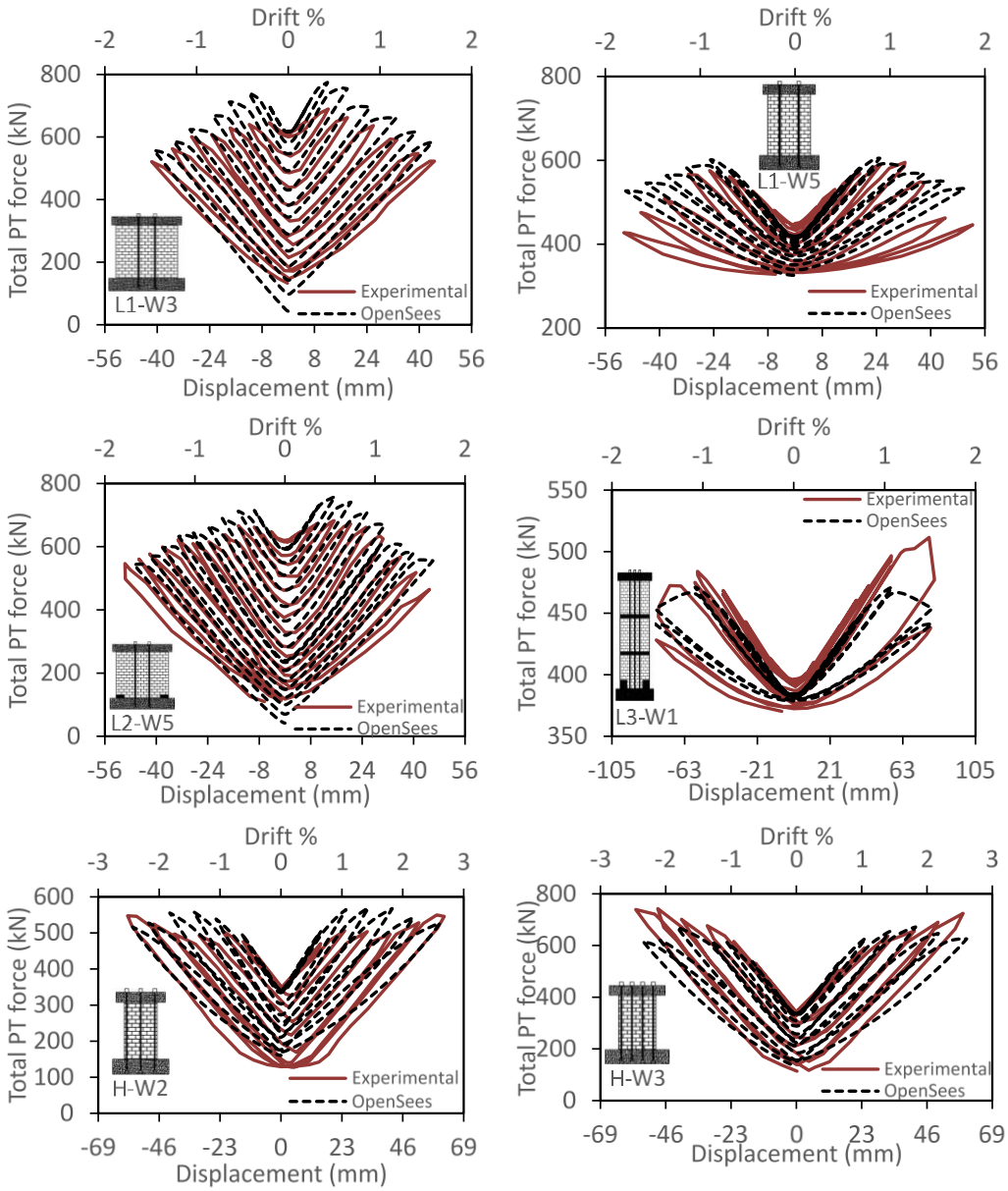


**Fig. 2.5.** Experimental and numerical cyclic responses for unbonded PT bars

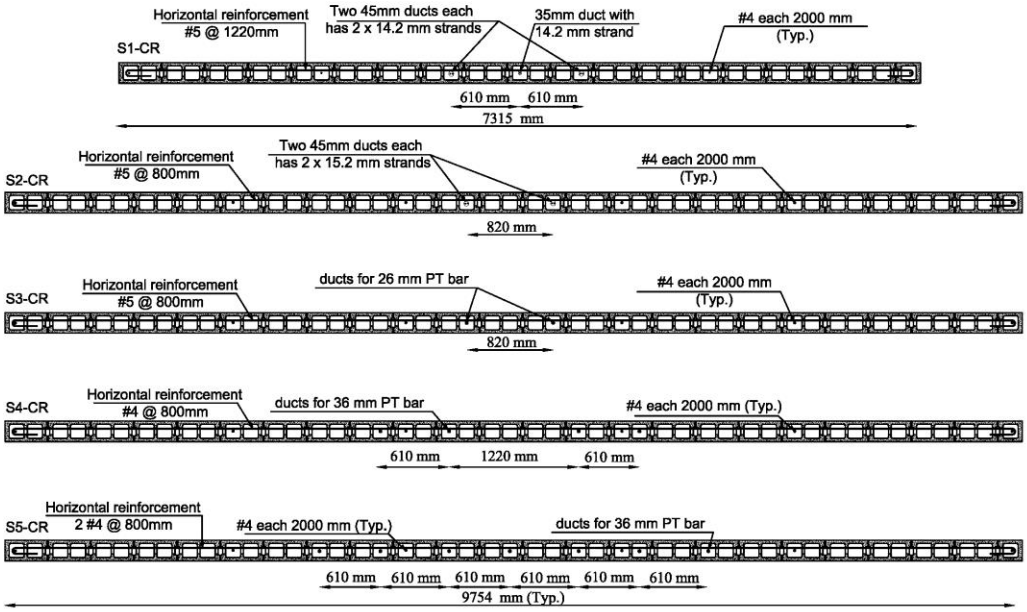


**Figure 2.6.** Wall cross section and PT bar configurations

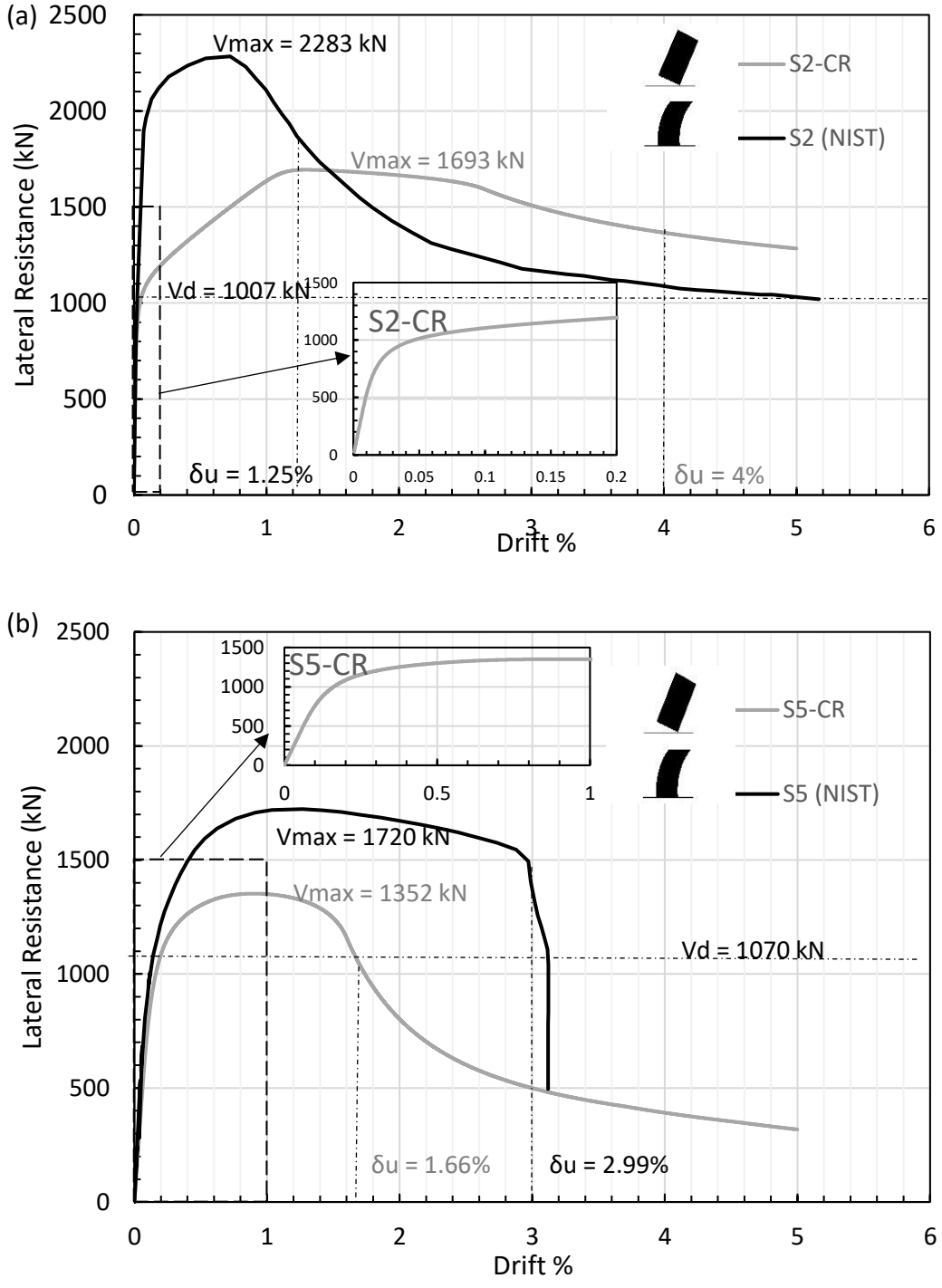


**Figure 2.7.** Archetype pushover curves

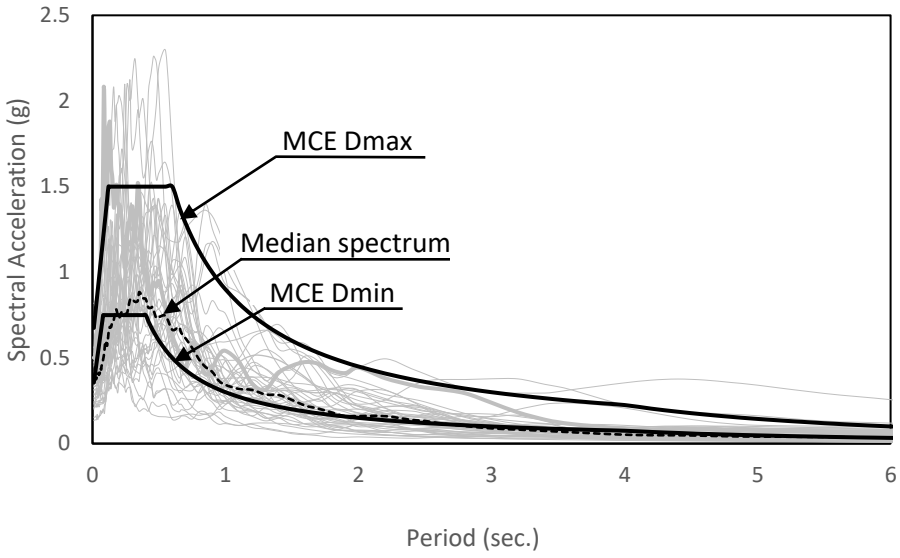


**Figure 2.8.** Response spectra of the 44 ground motions, scaled median response spectrum of record set for wall S6-CR, maximum considered earthquake at SDC Dmax, and SDC Dmin

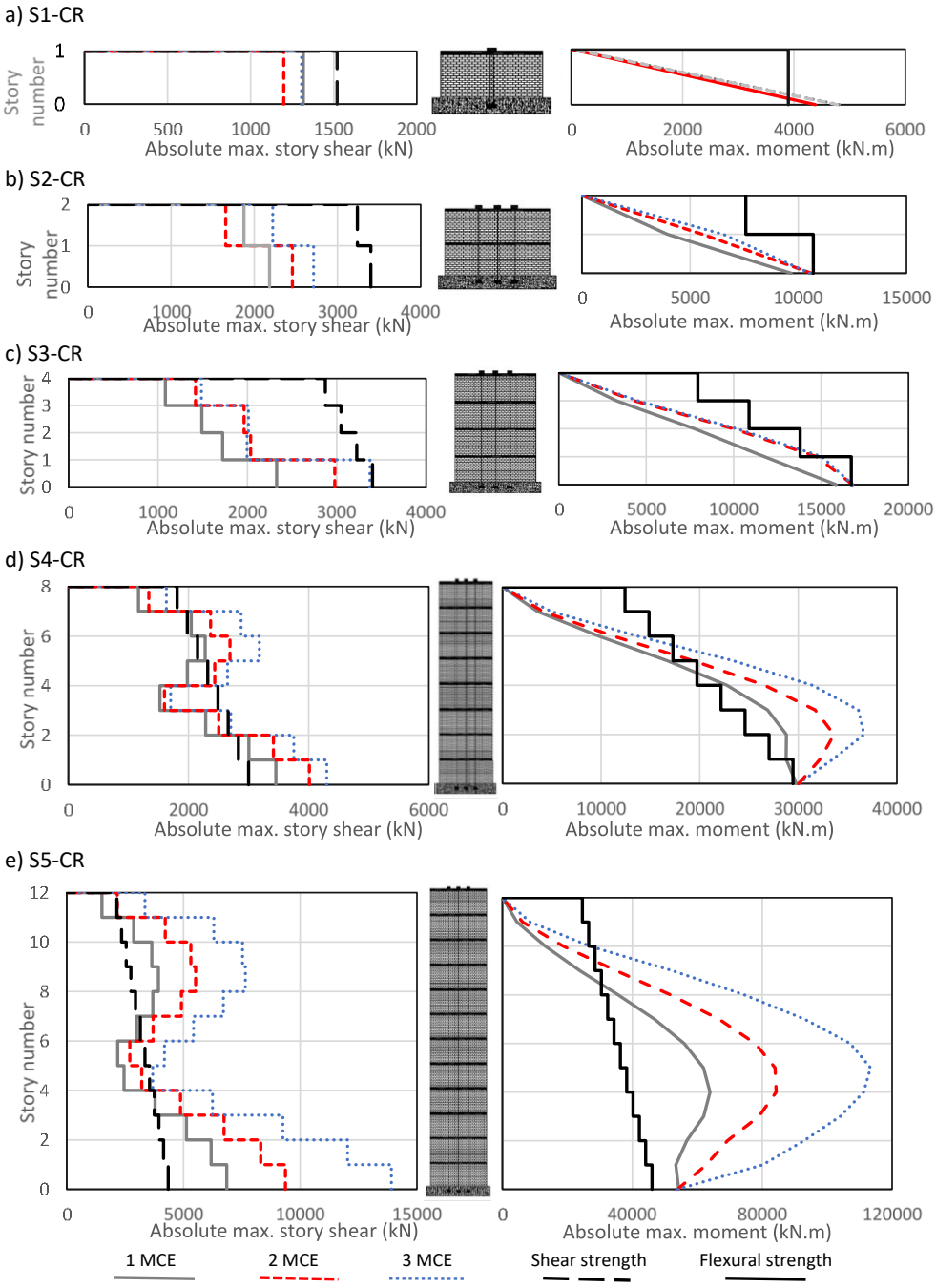


**Figure 2.9.** Story shear and moment envelopes for S1-CR to S5-CR archetypes during Imperial Valley ground motion

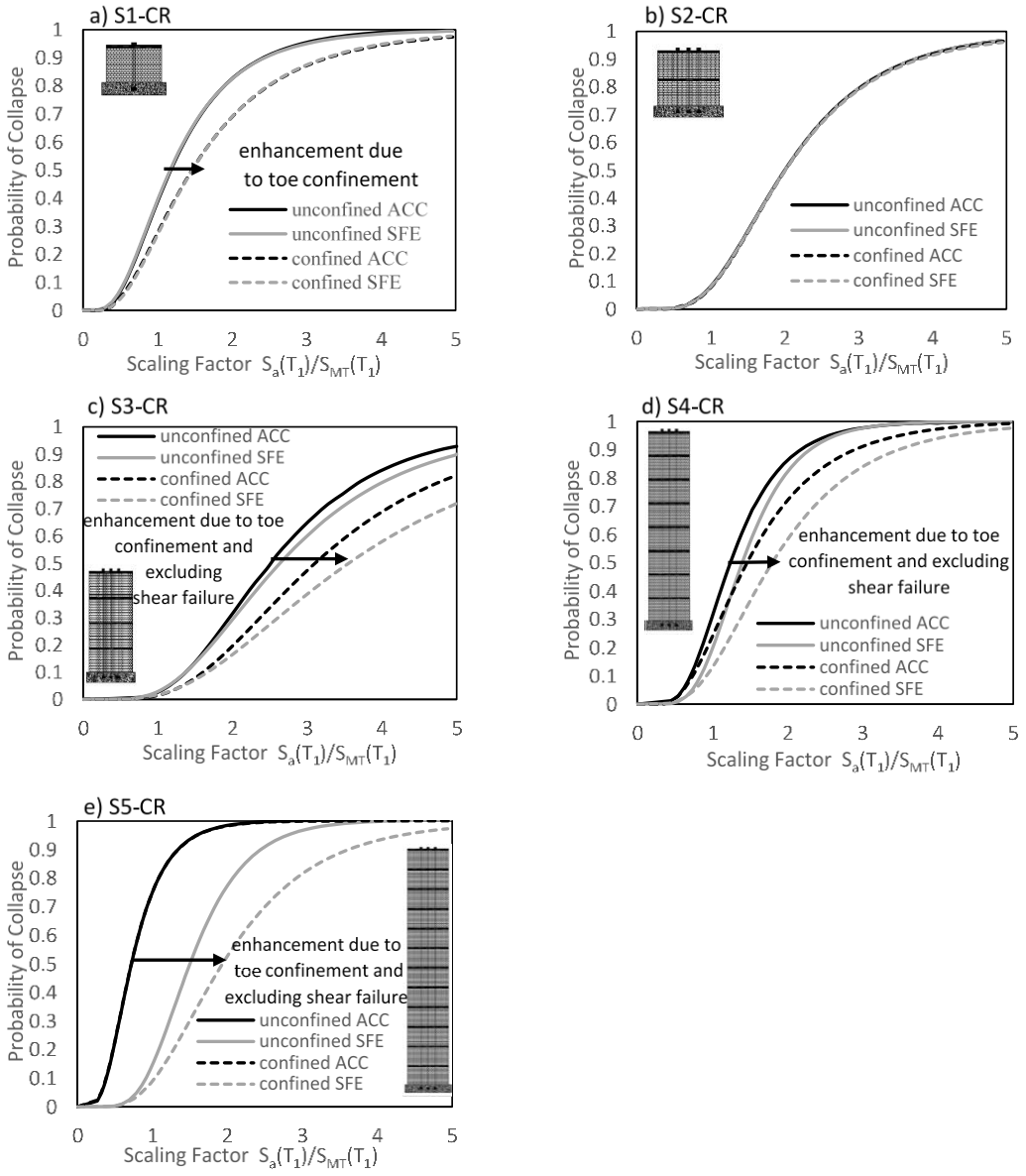


**Figure 2.10.** Collapse fragility curves for confined and unconfined archetypes considering all collapse criteria (ACC) or with shear failure excluded (SFE)

# Chapter 3

# EXPERIMENTAL ASSESSMENT OF CONTROLLED ROCKING MASONRY SHEAR WALLS WITHOUT POSTTENSIONING

## 3.1. ABSTRACT

Several research studies have recently evaluated the seismic response of controlled rocking masonry walls (CRMWs) with unbonded post-tensioning (PT) tendons. These studies demonstrated that such walls typically have both low damage and self-centering ability, thus presenting an enhanced seismic response compared to conventional fixed-base shear walls. However, practical difficulties related to PT implementation during construction, coupled with the problem of PT losses which subsequently affects the wall self-centering ability, point to an opportunity to develop an alternative approach to control rocking walls. In response, the current study introduces controlled rocking masonry shear walls without PT tendons and with energy dissipation (ED) device of embedded unbonded axial yielding dog-bone bars, named as ED-CRMWs. Experimental results are presented from six half-scale two-story fully grouted ED-CRMWs that were tested under displacement-controlled cyclic loading. All six walls were designed to have the same lateral resistance to facilitate investigating the influence of different design parameters, including toe confinement strategies through steel plates or boundary elements, axial compressive stress levels, ED device locations, and horizontal reinforcement ratios. The experimental results are presented in terms of the failure modes and

damage levels, force-displacement response, residual drifts, and ductility capacities. The results show that even with no PT, all ED-CRMWs preserved the intended self-centering behavior with a flag-shaped hysteretic response, having a maximum residual drift ratio of 0.15%, except for one unconfined wall. In addition, the strategy of using end-confined boundary elements produced the most effective performance of the system pertaining to strength degradation, self-centering, and displacement ductility with a drift ratio of 2.35% being reached before strength degradation. In general, all walls exhibited limited and localized damage at the wall toes, thus demonstrating the promising concept of relying on gravity loads and ED devices in CRMWs, without the need for unbonded PT tendons.

## 3.2. INTRODUCTION

The design of special reinforced masonry walls (SRMWs) is oriented towards reducing stiffness and dissipating energy through the inelastic behavior of reinforcement yielding, while special detailing is maintained to ensure system ductility. Although this nonlinear inelastic behavior reduces design forces, it normally leads to residual drifts and corresponding permanent damage. An alternative nonlinear mechanism, popularized by Priestley et al. (1999), is based on an elastic gap opening mechanism (rocking base) that reduces the wall lateral stiffness and subsequently replaces the typical yielding of reinforcement in SRMWs (i.e., fixed-base walls). Following earthquakes, rocking walls have the ability to return to their original vertical positions with minimal residual drifts,

which is known as self-centering behavior. This behavior is often promoted by using unbonded post-tensioning (PT) tendons to control the rocking response. Consequently, controlled rocking walls with self-centering ability can be considered promising for resilient structures, minimizing structural damage and associated interruptions of building usage (Chancellor et al. 2014).

Controlled rocking walls with unbonded PT tendons have been investigated by several researchers. Priestley et al. (1999) dynamically tested a 60% scale five-story precast concrete building as part of the Precast Seismic Structural Systems (PRESSS) project. The results confirmed that the lateral response was governed mainly by rocking deformations, while flexural and shear deformations were minimal (Nakaki et al. 1999) with a residual drift of only 0.06% after loading to 1.8% drift. These promising results led researchers to extend the rocking mechanism to unbonded PT controlled rocking masonry walls (PT-CRMWs). For example, Laursen and Ingham (2001 and 2004) conducted an extensive study on 16 PT-CRMWs to investigate the effects of grouting infill (fully-grouted, partially-grouted, and un-grouted), wall aspect ratios, locations of PT tendons, and prestressing levels. Confinement plates and dog-bone axial yielding devices were used to enhance the performance of these walls under in-plane cyclic loading. In addition, Rosenboom and Kowalsky (2004) carried out experimental tests using clay masonry blocks to investigate the effects of bonded and unbonded PT bars, supplemental mild steel, and confinement plates on the behavior of PT-CRMWs. Wight et al. (2006) also performed shaking table tests on solid and perforated PT-

CRMWs and a simple masonry structure. Recently, Hassanli et al. (2016) tested four fully-grouted concrete masonry walls with different initial prestressing to yielding stress ratios and different distributions of PT bars. A numerical study has also been conducted recently on the seismic collapse risk of PT-CRMWs (Yassin et al. 2020). All the above studies demonstrated that the behavior of fully-grouted post-tensioned controlled rocking masonry walls was similar to that of controlled rocking precast concrete walls, including minimal residual drifts and localized damage at the wall bases.

Previous studies on controlled rocking systems have used unbonded PT tendons to provide strength that increases the rocking load, stiffness for the wall after decompression, and to maintain self-centering ability after the lateral load is removed. Despite these advantages, the application of unbonded PT tendons in masonry also creates challenges due to the high compression demands on the masonry toes when dead and live loads are added in practical construction scenarios (Laursen and Ingham 2004). These challenges are mainly related to the low compression strain capacity of masonry due to the lack of confinement detailing relative to concrete (Priestley and Elder 1983). In addition, PT losses due to PT yielding and early strength degradation of masonry (Hassanli et al. 2016) reduce the self-centering ability of PT-CRMWs. Such challenges demonstrate the importance of considering an alternative source of self-centering. In this regard, the current study proposes a new controlled rocking system for masonry walls, namely Energy Dissipation-Controlled Rocking Masonry Walls (ED-CRMWs). The study

evaluates the capability of this system to self-center through vertical gravity loads only, without the use of PT tendons, while a supplemental energy dissipation (ED) device is designed and used to increase strength and to control seismic lateral displacements. As ED-CRMW systems mainly depend on gravity loads to have their strength, which depends on the architectural plan configuration, these systems may require more walls at their floor plan to reduce the demand compared to PT-CRMWs. Since confinement of masonry toes is an important aspect for wall ductility (Priestley and Elder 1982; Hart et al. 1989; Shedid et al. 2010; Banting and El-Dakhakhni 2014; Ezzeldin et al. 2016), the use of steel plates and boundary elements is also considered herein as applied to the proposed ED-CRMWs.

The current chapter reports the experimental results of six half-scale two-story fully grouted ED-CRMWs tested under displacement-controlled cyclic loading. The chapter investigates the effects of the following parameters on the overall behavior of ED-CRMWs: (1) elimination of PT, (2) adoption of different confinement strategies for wall toes, (3) location of ED device, and (4) axial stress level. In this respect, the chapter first presents a description of the experimental program, test setup and instrumentation, and provides information about the properties of the construction materials used in the six walls. Following this experimental program section, the chapter focuses on comparing the damage sequence, the force-displacement hysteretic behavior, the self-centering, the neutral axis depth and the base rotation, and the displacement ductility of the six walls. Finally, the predicted flexure and shear strengths using The Masonry Society (TMS

402/602 2016) expressions are reported and compared with their corresponding experimental values.

## 3.3. EXPERIMENTAL PROGRAM

The experimental program was designed to evaluate the lateral response of six ED-CRMWs without unbonded PT tendons and with different confinement strategies (i.e., steel plates or boundary elements), as presented in Table 3.1. The walls were selected to investigate the influence of each design parameter on the failure modes and extent of damage, post-peak behavior, displacement ductility, and self-centering capability. All six walls were subjected to fully-reversed displacement-controlled quasi-static cyclic loading.

### 3.3.1. TEST MATRIX

Using half-scale blocks, six two-story concrete-block shear walls were constructed, each with a length of 1895 mm (corresponding to 3990 mm length in full-scale). The half-scale blocks (90 x 90 x 185 mm) that were used are true replicas of the full-scale concrete-blocks (190 x 190 x 390 mm) widely used in North America. Full details pertaining to the use of scaled masonry units and scaled reinforcement bars in testing models can be found in Harris and Sabnis (1999). The cross-sections and reinforcement details of all the walls are shown in Fig. 3.1. As can be seen in the figure, minimum vertical bonded D7 bars (area = 45 $mm^2$) were provided inside the walls according to the TMS (2016), but they were not embedded in the foundation and were instead terminated at the wall-foundation interface. Such D7

bars were only used to maintain the wall integrity during rocking and satisfy the standard design requirements for seismic detailing. In addition, two internal unbonded axial yielding ED M10 bars (area = 100 $mm^2$) were used for all six walls, each with an unbonded length of 900 mm to ensure sufficient base rotation ductility with enough yielding before masonry crushing. The ED connection details are shown in Fig. 3.2.

Five walls (W1 and W3 to W6) had rectangular cross-sections, while wall W2 was an end-confined boundary wall, where the boundary elements at the wall ends were built with pilaster units (185 mm x 185 mm). Multiple confinement strategies were also investigated, as shown in Fig. 3.1. Specifically, while wall W1 had no confinement, closed ties were provided each 160 mm for end-boundary wall W2. For walls W3 to W6, Priestley steel plates (1.58 mm thickness of grade 350W) were provided within the bed joints of the first five courses at the wall ends.

In all walls, ED devices were placed at $\pm$700 mm from the wall centerline, except W4, where ED devices were placed at $\pm$140 mm from the wall centerline to investigate the effect of the ED location on the wall behavior. In addition, five walls (W1 to W4 and W6) were subjected to an axial stress of 1.17 MPa, representing normal intensity slab gravity loads, while wall W5 was subjected to a higher axial stress of 2.31 MPa to investigate the influence of the axial load on the wall response. D4 bars (area = 25 $mm^2$) were also used as horizontal reinforcement every other course for five walls (W1 to W5), while only wall W6 did not have any horizontal reinforcement to quantify its influence on the wall overall behavior.

### 3.3.2. DESIGN CRITERIA

All walls were designed to have the same lateral load capacity to facilitate investigating the influence of each design parameter. The walls were also capacity designed to fail in flexure due to toe crushing with adequate horizontal shear reinforcement, except wall W6 as mentioned earlier. Since the design of the walls was intended to ensure self-centering, the amount of ED (i.e., cross section area) was set so that the ratio of the moment contribution of ED to that of restoring force due to gravity loads is less than one (Kurama 2005). In addition, following the ACI ITG 5.2 (2009) recommendations, the maximum developed ED force $F_u$ should be less than the restoring gravity force $P$ to ensure rocking joint (wall-foundation interface) gap closure after loading. Both requirements were addressed as shown in Eqns. 3.1 and 3.2, respectively. A full detailed design guideline for ED-CRMWs is presented by Yassin et al. (2021).

$$\frac{\sum_{i=1}^{n} f_{uED} A_{iED} (d_i - a/2)}{P(\frac{L_w - a}{2})} < 1 \quad (3.1)$$

$$\frac{\sum_{i=1}^{n} f_{uED} A_{iED}}{P} < 1 \quad (3.2)$$

where $f_{uED}$ is the ED bar ultimate stress, $A_{iED}$ is the cross-sectional area of ED bar $i$, $d_i$ is the distance from ED bar $i$ to the outermost compression fiber, $a$ is the equivalent rectangular stress block, $P$ is the gravity load including the wall self-weight, and $L_w$ is the wall length. At the decompression stage (when the wall is about to uplift), the wall resistance, $Q_{Dec}$, was calculated based on axial loads only, where ED devices were assumed not yet engaged at zero base rotation, $\theta$. Moreover,

ED yielding should occur only in the unbonded length, while the bonded zone should not yield in order to prevent tension cracks inside the masonry. In this regard, the unbonded length is selected to cross the base rocking joint, as shown in Fig. 3.2. The design criteria of the ED-CRMWs are to ensure decompression and then ED yielding before masonry crushing takes place to ensure ductility, and finally ED fracture. To achieve this, the ED bar curtailment is required to prevent bar fracture before reaching the ultimate stage (i.e., crushing of wall corners). In this regard, the unbonded length, $L_{un}$, (taken as 900 mm in the current study) was selected such that the strain demand at the ED bar location due to uplifting at the ultimate drift (when the masonry strain at the outermost fiber reached 0.0025, as specified by the TMS 2016) is greater than four times the yield strain ($5.5\varepsilon_y$ in the current study), and also less than 85% of steel strain at ultimate strength in order to avoid low cycle fatigue.

### 3.3.3. CONSTRUCTION DETAILS

Wall construction was carried out using half-scale 5 mm thick mortar joints to represent the 10 mm common joints in full-scale masonry construction. Following common North American practice, all the wall specimens were built by a professional mason in a running bond pattern with face shell mortar bedding. For each wall, two reinforced concrete (RC) slabs were constructed with 90 mm thickness and were reinforced by 3 and 8 M10 bars in the longitudinal and transverse directions, respectively. Each wall was constructed on a 500 mm thick

by 500 mm wide by 2300 mm long concrete footing that was reinforced by top and bottom M10 bars at 200 mm in both orthogonal directions. A rigid steel loading beam, composed of two equal 150 mm leg angles, was placed on top of the second story slab and connected to the slab by 8 M20 shear studs. To prevent sliding at the wall base, a steel stopper at a 45° angle was mounted on the footing at each end of the wall, as shown in Fig. 3.3. To accommodate the wall horizontal reinforcement, the masonry unit webs were saw cut to a depth of 20 mm to generate notches. For rectangular walls, the horizontal reinforcement formed 180° hooks around the outermost vertical bonded bars, with a 200 mm return leg that extended to the third-last cell in order to provide sufficient development length, as shown in Fig. 3.1. For end-boundary wall W2, the horizontal reinforcement along the web was extended inside the boundary element zone and was bent 90° around the outermost vertical bonded bars. Also, for wall W2, the D4 bars were used as closed ties around the four vertical bonded bars, as shown in Fig. 3.1. The construction stages of all walls started by placing the ED bars (M10) (welded with end plate 50mm x 50mm at its end) inside hollow PVC tubes to ensure their unbonding within the required length. Then the ED bars (M10) were placed inside the footing and secured its position through welding of the end plate to the footing reinforcement cage. After pouring the footing, the first six courses were constructed and fully grouted using a high-slump grout with a maximum aggregate size of 5 mm. The remaining seven courses were then constructed and fully grouted. Once the first story was completed, temporary formwork was placed for the RC slab and the reinforcement was placed

before the concrete was poured. The same process was repeated for the construction of the second story.

### 3.3.4. MATERIAL PROPERTIES

Samples from the half–scale blocks were randomly selected and tested in accordance with CSA A165-14 (CSA 2014a) using hard capping and 120 mm thick loading plates. The average compressive strength for the blocks, based on a net area of 8,490 $mm^2$, was 33.8 MPa with a coefficient of variation (COV) = 7.8%. Ready mix Type S was used for mortar, and flow table tests were performed and resulted in an average flow of 120%. Forty-two mortar cubes (three per batch during construction), were tested in compression following CSA A179-14 (CSA 2014d) and yielded an average compressive strength of 24.8 MPa (COV = 6.3%). Thirty-two fine grout cylinders were tested as per CSA A179-14 (CSA 2014d) and the average compressive strength was 22.8 MPa (COV = 11.8%). The concrete used in the footing and story slabs had average compressive strengths of 30.0 MPa (COV=7.3%) and 33.0 MPa (COV=8.9%), respectively. Three four-blocks high by one-block long (375 mm high x 185 mm long x 90 mm thick) fully grouted masonry prisms were constructed during each construction stage (a total of twenty-four prisms). These prisms were later tested in accordance with CSA S304-14 (CSA 2014c), and the specified masonry strength, $f'_m$, and average compressive strength for the prisms, $f_{av}$, were 16.4 MPa and 18.9 MPa, respectively (COV = 13.3%). Tension tests were also performed on all bars according to CSA G30.18-

09 (CSA 2014b). The average yield strengths of the M10, D7 and D4 bars were 476 MPa (COV = 4.2%), 461 MPa (COV = 3.2%), and 489 MPa (COV = 5.8%), respectively.

### 3.3.5. TEST SETUP

The test setup components and connections are shown in Fig. 3.3. The lateral cyclic displacement was applied at the second-floor slab using a hydraulic actuator with a maximum capacity of 500 kN and a maximum stroke of $\pm$250 mm. The walls were constrained in the out-of-plane direction at the first- and second-story slabs using a guidance frame system of four points at each slab. A constant axial load was applied using two hydraulic jacks, each attached at the top of the wall using two 26-mm diameter high-strength rods anchored to a steel box section, which in turn was attached to the double angle steel loading beam.

### 3.3.6. INSTRUMENTATION AND LOADING PROTOCOL

Displacement potentiometers were used to monitor the wall lateral displacements and vertical deformations, as shown in Fig. 3.4. Specifically, to track the gap opening of the rocking joint, five vertical potentiometers (V1 to V5) were attached to the footing surface and connected to the wall at 240 mm above the wall-foundation interface. In addition, twelve vertical potentiometers (V6 to V17) were used to measure the wall vertical displacements, which were then converted into axial strains to calculate the curvature distribution along the wall height. Lateral displacement potentiometers (H1 to H6) were used to record lateral drifts and

wall/footing sliding. Masonry compressive strains at the wall toes (corners of the first course) were recorded during testing using Linear Potentiometers (L1 and L2) with 100 mm gauge length at each toe, converting the change in displacements to vertical strains in the masonry within the gauge length. Strain gauges (S) were also used to monitor the initiation and extent of yielding of the ED devices (S1 to S3 and S6 to S8), the outermost vertical bonded bars (S4 and S9), and the horizontal reinforcement (S5). As can be seen in Fig. 3.4, six strain gauges were attached to the ED M10 bars, four of which were mounted within the unbonded length, $L_{un}$ (at 0.3 and 0.5 of $L_{un}$), while the remaining two strain gauges were mounted at 100 mm into the bonded region.

The FEMA 461 (2007) quasi-static testing protocol was adopted in the current study, as shown in Fig. 3.5. According to this protocol, at least six cycles should be executed before the lowest damage state is reached. In the current study, the onset of ED yielding was considered as the lowest damage state and the corresponding wall displacement was estimated using the analytical model developed by Yassin et al. (2018) to calculate the initial amplitude cycle $\Delta_o$. Afterwards, each cycle was repeated twice and the displacement amplitude was increased by 40% from the previous amplitude until reaching the ultimate displacement, $\Delta_u$ (FEMA 2007), corresponding to the wall ultimate resistance at which the most severe damage level is expected to initiate. This displacement was also predicted in the current study using the model developed by Yassin et al. (2018). Beyond $\Delta_u$, the displacement amplitude was increased by $0.3\Delta_u$ each cycle

as per the FEMA 461 (2007) guidelines. Each test was terminated either when the actuator reached its full stroke capacity or when the wall lost 50% of its lateral load resistance, $Q_u$.

## 3.4. TEST RESULTS

### 3.4.1. DAMAGE SEQUENCE AND FAILURE MODES

The failure modes and extent of damage are discussed for all walls in this subsection. Drift is defined as the lateral displacement measured by the horizontal potentiometer H1 normalized by 2.51 m (i.e., the height of H1 above the wall-foundation interface). In general, all walls showed a pure rocking response characterized by a gap opening at the rocking joint, the eventual failure mode is due to toe crushing, without any horizontal tension or diagonal shear cracks, and no sliding was observed at any time throughout any of the tests.

For wall W1 with no confinement, the rocking joint started opening at 0.06% drift when the wall started rocking, as presented in Table 3.2. The rocking joint opening extended to half the wall length at 0.12% drift. Afterwards, the unbonded ED bars reached the yield strain at 0.22% drift with no evidence of tension horizontal cracks at the wall bed joints, including those above the unbonded length. Vertical cracks were initiated only at the first course of both wall corners at 0.45% drift. Subsequently, face shell spalling initiated at these corners with the propagation of vertical cracks inward to the second block of the first course at 0.90% drift. After that, complete face shell spalling was observed at a drift ratio of

1.25%, as shown in Fig. 3.6a. Crushing of the wall compression toes in both corner blocks was then observed with the propagation of the damage inward to the second and third blocks of the first and second courses at 1.90% drift, with buckling of the ED bars. Finally, fracture of the ED bars was observed at 2.80% drift, by which the rocking toes had shifted inward to the fourth block on both wall sides. As can be seen in Fig. 3.6a, the wall damage was limited to the four corner blocks of the first and second courses.

For wall W2 with end-confined boundary elements, a similar behavior to wall W1 was observed at the early stages of loading (up to 0.22% drift), as shown in Table 3.2. However, the first minor vertical cracks did not begin to initiate at the first course of both wall toe pilaster blocks until 0.68% drift. Superficial face shell peeling started at these toes at a drift ratio of 1.0%. Afterwards, a distinctive behavior of W2 was observed compared to W1. Specifically, due to the presence of closed ties at the pilaster blocks, the confined cores which were subjected to high compression demands did not deteriorate. Although the ED bars buckled at 1.60% drift, causing face shell spalling, the wall resistance did not drop as the compression zones were still protected within the confined boundary elements. Therefore, no progression of damage inward to the web blocks due to crushing was observed, indicating the efficiency of this confining technique. Afterwards, the pronounced uplift elongation and low cyclic fatigue in the ED bars caused the fracture of the bars at 2.4% drift at both ends (in the push and pull directions), leading to a sudden drop in the wall strength of about 30%, as discussed in detail in the following

section. The test continued until 4.90% drift with limited damage at the wall boundary elements and without any tension or diagonal shear cracks, as shown in Fig. 3.6b.

For wall W3 with Priestley plates, a similar damage sequence to W1 was noticed, as presented in Table 3.2. Face shell spalling at the wall compression toes along with spreading of vertical cracks inward to the second block of the first course were noticed at 1.25% drift, as shown in Fig. 3.6c. Crushing of both corner blocks and complete face shell spalling of the second block of the first course due to ED buckling resulted in strength degradation at 1.60% drift. Finally, the ED bars fractured at 2.30% drift, and complete crushing of the third block of the first course was observed at 2.60% drift. As shown in Fig. 3.6c, unlike wall W1, the damage was limited to the first three blocks on each side of the wall's first course.

For wall W4 with inner ED and Priestley plates, the onset of the ED yielding was delayed to 0.46% drift, as presented in Table 3.2. This is due to the ED being closer to the wall centerline, so more base rotation was required to achieve yielding with the same unbonded length used. Face shell removal followed by crushing of both corner blocks occurred, leading to strength degradation of 15% at 2.25% drift. At the end of the test, the damage was limited to the first two blocks on each side of the wall's first course, as shown in Fig. 3.6d.

For wall W5 with a high axial stress level and Priestley plates, as shown in Fig. 3.6e, delayed initiation of rocking and yielding occurred at 0.09% and 0.35%

drift, respectively, relative to wall W3, as shown in Table 3.2. Also, vertical cracks reached the seventh course (compared to only the first course in wall W3) with face shell spalling of only the corner block at the push side at 1.9% drift. However, early initiation of strength degradation at 0.9% drift occurred due to face shell spalling of the wall toes at the pull side. This unsymmetric response might be attributed to low grout compaction in the pull side corner leading to core grout voids, and hence early crushing compared to the push side. In this regard, only the push side of wall W5 is considered in the following sections.

For wall W6 with Priestley plates and no horizontal reinforcement, shown in Fig. 3.6f, early ED bar buckling was observed along with complete crushing of both compression rocking toes, leading to premature strength degradation in the wall's post-peak behavior compared to wall W3. These results confirm the importance of horizontal reinforcement in maintaining the wall integrity and preventing premature post-peak strength deterioration, as suggested by Hassanli et al. (2016) and Laursen (2002).

### 3.4.2. FORCE-DISPLACEMENT RESPONSE

Figure 7 shows the relationship between the force measured by the load cell of the hydraulic actuator and the corresponding lateral displacement of the horizontal string potentiometer H1. As intended, Fig. 3.7 shows that all the six ED-CRMWs had approximately the same ultimate strength, $Q_u$, of about 95 kN, except for W5 that reached 148 kN due to its higher axial stress level (see Table 3.1). The ultimate

strength of wall W2 was also 103 kN, where this 8.5% higher strength is attributed to the enlarged wall ends that reduced the required length of the wall in compression, leading to a longer moment arm and hence increased flexural strength. In addition, for all walls, as depicted in Fig. 3.7, the increase in wall strength due to strain hardening after the ED bars yielded was relatively small. This is mainly attributed to not using distributed ED bars along the wall length, but only one ED bar at each wall side.

As shown in Fig. 3.7, wall W2 with end-confined boundary elements reached its peak strength at a drift ratio of 2.30%, while the rectangular walls (W1, W3-W6) reached their peak strengths at drift ratios of 1.30%, 1.25%, 1.35%, 0.85%, and 0.72%, respectively. This reflects an advantage of using boundary elements at the wall ends, which increased the ultimate displacement by at least 70%. In addition, the hysteretic loop of wall W4, shown in Fig. 3.7d, has less enclosed area compared to the other rectangular walls (i.e., relatively pinched) due to the ED bars being located at $\pm$140 mm from the wall centerline, which reduced the elongation demand on the ED bars.

As shown also in Fig. 3.7, all rectangular walls (W1, W3-W6) experienced gradual strength degradation due to deterioration of the rocking toe, reaching 80% of their ultimate strengths at drift ratios of 2.00%, 1.90%, 2.20%, and 1.75% for walls W1, W3, W4, and W6, respectively, and 1.95% and 1.60% in the push and pull directions for wall W5, respectively. Conversely, for wall W2, no strength degradation due to rocking toe crushing was observed; however, due to the

symmetrical fracture of both ED bars, a sudden 30% loss in the wall strength occurred at 2.40% drift in both push and pull directions. The 30% reduction in strength corresponds to the designed contribution of the ED bars, while 70% of the wall strength was retained because of the axial load. Testing of wall W2 continued until 4.90% drift, with the wall responding in a free rocking mode with essentially no energy dissipated. Although wall W2 did not reach 50% strength degradation, the test was terminated at 4.90% drift because the maximum stroke of the actuator was reached.

### 3.4.3. LATERAL LOAD CAPACITY AND DISPLACEMENT CHARACTERISTICS

The load-displacement envelopes for all six ED-CRMWs are presented in Fig. 3.8. As shown in Fig. 3.8, the different stages that each ED-CRMW undergoes represent the unique characteristic behavior of this system, by which the system exhibited a near ideal elastic-perfectly plastic load-deformation behavior. Specifically, for each wall, the first stage was decompression, which corresponded to the point where a change in wall stiffness was observed at small drifts before yielding of the ED bars occurred. At this point, the rocking mechanism initiated with the wall uplifting from the foundation to form a single horizontal crack at the wall-foundation interface. This occurred when the base overturning moment due to lateral loads exceeded the wall decompression moment capacity. All the lateral deformations before the decompression stage were only flexure and shear deformations, whereas

later deformations were primarily due to rocking, as will be discussed in detail later. All ED-CRMWs reached this decompression stage at a drift ratio of 0.06% (except W5 at 0.09%) and exhibited essentially the same decompression strength, $Q_o$, of about 60 kN (except W5 at 98 kN).

The next distinctive change in lateral stiffness in Fig. 3.8 was caused by the yielding of the ED bars, as verified by the strain gauge readings. All ED-CRMWs reached this stage at a drift ratio of 0.22% (except wall W4 at 0.45% and wall W5 at 0.35%) and exhibited almost the same yield strength, $Q_y$, of about 90 kN (except wall W5 of 145 kN). Afterwards, an almost horizontal plateau was observed in the force-deformation envelopes for all ED-CRMWs, where the length of the plateau depended mainly on the confinement strategy used in the wall. In this regard, all walls reached at least 1.5% drift before significant strength degradation, and the level of enhancement in displacement capacity achieved by the boundary elements in wall W2 is clear. Conversely, the effect of the axial compression level in reducing the wall displacement capacity of wall W5 is also clear.

### 3.4.4. SELF-CENTERING

To quantify the self-centering capability of the tested ED-CRMWs, the lateral drift at the point of zero lateral force was considered as the residual drift, $d_r$, measured at the end of the first cycle at each displacement level. In Fig. 3.9, the residual drift, $d_r$, after each cycle is plotted against the corresponding peak drift of that cycle. As shown in the figure, the residual drifts for walls with confining strategies W2-W6

(i.e., end-confined boundary elements or confining plates) had residual drifts of no more than 0.15% throughout the tests, which is less than the 0.2% residual drift assigned by the FEMA P58 (2018) for damage state DS1, where no structural realignment or repair is required. This illustrates the advantage of using boundary elements or confining plates, which protected rocking toes from deterioration and maintained self-centering capability throughout the test. Conversely, wall W1 without any confinement exhibited increased residual drifts, reaching a maximum of 0.43% at the end of the test due to significant deterioration and crushing of the rocking toes. In general, ED-CRMWs can achieve similar behavior as their PT-CRMWs counterparts regarding the self-centering capability, even without PT.

### 3.4.5. MASONRY VERTICAL STRAIN

Masonry vertical strains at the wall toes in both push and pull directions are presented in Fig. 3.10. In this study, the reported compressive strains at the crushing toes are limited to the stage just before strength degradation is initiated, and no data is reported after that stage because the damage to the toe regions made any readings unreliable. As seen in Fig. 3.10, all ED-CRMWs reached a compressive strain of 0.015 safely without any strength degradation, and this value is considerably higher than the 0.0025 usable strain in the TMS (2016) standard for bonded PT walls. This finding is consistent with previous experimental tests on rocking walls with unbonded PT (Laursen 2002; Hassanli et al. 2016), where such walls reached high strains compared to those of conventional fixed-base walls

without rocking behavior. This is mainly because damage to the crushing toe is not exacerbated by tension yielding cracks during reversed cycles as in conventional walls. Moreover, the boundary elements of wall W2 were clearly effective in reducing the compressive strain at a given drift, as shown in Fig.3.10. This is due to the reduction in its neutral axis depth, as will be discussed next.

### 3.4.6. NEUTRAL AXIS DEPTH

Figure 3.11 shows the base crack profile of the rocking joint in the push and pull directions for all walls. As shown in Fig. 3.11, the base rocking joint gap widens as the drift ratio increases for all six walls. For example, the gap opening for all walls reached between 12.9 mm to 15.0 mm at the extreme left and right sensors at a drift ratio of 0.90%. However, wall W2 with boundary elements achieved the largest gap opening among all the walls: 68 mm, which corresponds to 3.90% drift.

Fig. 3.11 was used to determine the neutral axis depth (N.A.D.) at different drift levels, and these are shown in Fig. 3.12. As can be seen in Fig. 3.12, for all walls, the N.A.D normalized by the wall length, $L_w$, decreased steeply until approximately 0.25% drift, after which the N.A.D. stabilized at approximately 6-9% of $L_w$, which agrees well with the design value (7.8% $L_w$). Afterward, for all walls, the deterioration of crushing toes increased the N.A.D. value as it shifted inward, as shown in Fig.3.11. For wall W2 with end-confined boundary elements, due to the preservation of the compression zone without significant deterioration,

the N.A.D. value was consistent at a small value of 3% of $L_w$ due to the enlarged boundary widths.

### 3.4.7. DISPLACEMENT DUE TO BASE ROTATION

Figure 13 shows the relationship between the base rotations and their corresponding lateral drift ratios. The base rotation was calculated using the measured vertical displacements at the wall bases (V1 and V5) and assuming that the wall rotation is a rigid body motion around the neutral axis (Kalliontzis and Schultz 2017a). As shown in Fig. 3.13, the wall base rotations and the drift ratios are close to each other with a maximum difference of only 8%, indicating that ED-CRMWs responded mainly in a rigid body rocking deformation. This finding agrees with previous research conclusions on PT-CRMWs (Kalliontzis and Schultz 2017b and Hassanli et al. 2016).

### 3.4.8. DISPLACEMENT DUCTILITY

Displacement ductility, $\mu_{\Delta}$, is used in the current study to evaluate and compare the post-peak behavior of the ED-CRMWs. All walls exhibited a near ideal point of nonlinearity followed by a plateau with minimal hardening, as shown in Fig. 3.8. Therefore, the displacement ductility, $\mu_{\Delta 0.8u}$, is defined herein as the ratio between the displacement corresponding to 80% degradation in the wall ultimate strength, and the displacement corresponding to the onset of ED bar yielding (confirmed by the strain gauge readings), without any idealization of the load-displacement

relationship. As shown in Table 3.3, a significant enhancement is obvious in $\mu_{\Delta 0.8u}$ for wall W2 compared to all rectangular walls. For example, the $\mu_{\Delta 0.8u}$ values of wall W2 are 40% and 48% higher than those of wall W1 in the push and pull directions, respectively. This reflects the influence of boundary elements in enhancing the seismic performance of rocking wall systems. However, compared to wall W1, Priestley plates did not enhance the displacement ductility of wall W3 as expected. This is attributed to the effect of ED bar buckling at wall ends which exacerbate the strength degradation of the wall and hence displacement ductility. Considering wall W4, the increased demands on the compression toes (as twice the ED area was used to get the same ultimate resistance) did not affect the displacement at 20% strength degradation, but the delayed yielding of the ED bars reduced the displacement ductility of wall W4 by 25% and 27% relative to wall W1 in the push and pull directions, respectively. Also, the effect of increasing the axial compression in reducing the wall ductility is clear in wall W5, which reached a displacement ductility of 5.9 and 5.1 in the push and pull directions, respectively. This is attributed to both delaying the yielding stage and reducing the displacement at 20% strength degradation because of early crushing. For wall W6 with no horizontal reinforcement, Table 3.3 shows that the displacement at 20% strength degradation was reduced relative to wall W3, leading to a decrease of displacement ductility, which confirms the importance of horizontal reinforcement to prevent premature post-peak failure.

## 3.5. STRENGTH PREDICTION AND LIMIT STATES DESIGN

The flexural strength of the ED-CRMWs considered in the current study was calculated based on a sectional beam analysis assuming a linear strain distribution. In this regard, the equivalent rectangular stress block depth, *a*, was calculated using the TMS (2016) equation presented in Eq. 3.3. The flexural strength of ED-CRMWs is then equal to the nominal moment capacity, $M_n$, provided in Eq. 3.4, divided by the effective height (i.e., from actuator centerline to the wall-foundation interface). The strength predictions were carried out without material or strength reduction factors.

$$a = \frac{\sum_{i=1}^{n} f_{yED} A_{iED} + P}{0.8 f_m^{'} b} \tag{3.3}$$

$$M_n = \sum_{i=1}^{n} f_{yED} A_{iED} (d_i - a/2) + P(\frac{L_w - a}{2}) \tag{3.4}$$

where $b$ is the wall width, $f_{yED}$ is the yield strength of the ED bars. The ED-CRMWs were designed to fail due to flexure by toe crushing. In this regard, shear failure due to diagonal tension or compression and sliding failure were prevented by ensuring that the resistance to shear and sliding was much greater than the wall flexure strength. The shear strength was calculated following the TMS (2016) as shown in Eq. 3.5 for fully grouted walls and considering shear reinforcement:

$$V_n = 0.083\left[4.0 - 1.75\left(\frac{M}{V d_v}\right)\right] A_{nv}\sqrt{f_m^{'}} + 0.25P + 0.5\left(\frac{A_v}{s}\right) f_y d_v \tag{3.5}$$

where $d_v$ is the shear depth (taken as $0.8L_w$), $A_{nv}$ is the net shear area, $f_m^{'}$ is the masonry prism compressive strength, $A_v$ is the shear reinforcement cross-section area, $s$ is the shear reinforcement spacing, and $f_y$ is the shear reinforcement yield strength.

The flexural strength predictions according to the TMS (2016) are presented in Table 3.3, where the predicted and experimental strengths are denoted by $Q_{pr}$ and $Q_{exp}$, respectively. In general, the results in Table 3.3 indicate that the use of beam theory resulted in accurate flexural strength predictions of ED-CRMWs for both configurations (i.e., rectangular and end-confined). This suggests that ED-CRMWs could be adopted in the North American design standards without modifying the existing strength calculation clauses pertaining to PT-CRMWs. Using Eq. 3.5, the shear strengths were determined as 219 kN for walls W1–W5 and 190 kN for Wall W6, which are significantly higher than the predicted flexural strengths provided in Table 3.3, confirming that a flexural failure mode was expected.

## 3.6. CONCLUSIONS

The current chapter evaluated the experimental results of six half-scale two-story fully grouted Energy Dissipation-Controlled Rocking Masonry Walls (ED-CRMWs) with different configurations, including energy dissipation (ED) locations, axial compression levels, and toe confinement techniques. The main objective of the chapter was to evaluate the ability of the walls to self-center with minimum residual drifts and damage localized at the wall toes only, similar to PT-CRMW counterparts. In this respect, all walls (except wall W5) were designed to have the same lateral resistance to allow for direct comparison. The experimental

work presented in this chapter led to the following observations and conclusions for the ED-CRMW system in general:

- All walls reached 1.5% drift without any strength degradation, with a flexural mode of failure due to crushing of wall toes without any tensile or shear cracks. In addition, all walls achieved high drifts of at least 1.8% with localized damage only within the crushing toes of the wall and/or ED bar fracture while the rest of the wall body was free of any damage.
- All walls achieved a high level of self-centering with less than 0.15% residual drift, except for wall W1, which reached 0.45% residual drift due to the absence of any confining technique for the wall toes. Moreover, the response of all walls was dominated by rocking deformations, which contributed about 92% of the total deflection. Hence, the system as designed can be considered as a rocking rigid body.
- For confining techniques, the Priestley plates limited the damage to be within the first row of blocks only and maintained an acceptable self-centering performance with 0.15% of residual drifts. On the other hand, the end-confined boundary elements significantly enhanced the wall response in all aspects: 1) the limited damage that was observed at the crushing toes with only superficial vertical cracks on the face shell, where the confined core remained intact up to 4.90% drift; and 2) the enhanced displacement ductility, $\mu_{0.8u}$, which was at least 40% larger than other walls, given that the sudden drop in strength was only due to the ED fracture and not due toe crushing.

- The high axial stress level (2.31 MPa) reduced the wall displacement ductility of wall W5 due to the increased compression demands on the wall toes and the associated delay of yielding.
- Placing the ED device close to the centerline of wall W4 reduced the energy dissipated and delayed the yielding stage, thereby reducing the wall displacement ductility capacity.
- Horizontal reinforcement is recommended for maintaining the wall integrity and preventing premature post-peak strength deterioration, even if it is not required for shear strength.

In general, the test results of the ED-CRMWs demonstrated that relying on gravity loads from slabs can maintain the high performance of rocking walls regarding self-centering capability, limited damage, and high drift capacity. Considering the cost savings by avoiding PT with the simplicity of the ED used, ED-CRMWs are considered a promising alternative to PT-CRMWs. One limitation to this system is that the internal ED device is inaccessible and thus not replaceable. Therefore, further research studies are still needed to investigate the applicability of using replaceable ED devices.

## 3.7. ACKNOWLEDGMENTS

The financial support for this project was provided through the Canadian Concrete Masonry Producers Association (CCMPA), the Canada Masonry Design Centre

(CMDC), the Natural Sciences and Engineering Research Council (NSERC) and the Ontario Centres of Excellence (OCE).

## 3.8. REFERENCES

ACI ITG-5.2 (American Concrete Institute). (2009). "Requirements for Design of a Special Unbonded Post-Tensioned Precast Shear Wall Satisfying ACI ITG-5.1 & Commentary." ACI ITG-5.2-09, Farmington Hills, MI.

Banting, B., and El-Dakhakhni, W. (2014). "Seismic performance quantification of reinforced masonry structural walls with boundary elements." Journal of Structural Engineering, 10.1061/(ASCE)ST.1943-541X.0000895, 04014001.

Chancellor, N., Eatherton, M., Roke, D., and Akbaş, T. (2014). "Self-centering seismic lateral force resisting systems: High performance structures for the city of tomorrow." Build. Multidiscip. Digital Publishing Inst., 4(3), 520–548.

CSA (Canadian Standards Association). (2014a). "Standards on concrete masonry units." CSA A165-14, Mississauga, ON, Canada.

CSA (Canadian Standards Association). (2014b). "Carbon steel bars for concrete reinforcement." CSA G30.18-09, Mississauga, ON, Canada.

CSA (Canadian Standards Association). (2014c). "Design of masonry structures." CSA S304-14, Mississauga, ON, Canada.

CSA (Canadian Standards Association). (2014d). "Mortar and grout for unit masonry." CSA A179-14, Mississauga, ON, Canada.

Ezzeldin, M., Wiebe, L., and El-Dakhakhni, W. (2016). "Seismic collapse risk assessment of reinforced masonry walls with boundary elements using the FEMA P695 methodology." Journal of Structural Engineering, 142(11), 04016108.

FEMA. (2007) "Interim testing protocols for determining the seismic performance characteristics of structural and nonstructural components." FEMA 461, Washington, DC.

FEMA. (2018) "Seismic performance assessment of buildings" FEMA-P58, Washington, DC.

Harris, H., and Sabnis, G.M. (1999). "Structural Modeling and Experimental Techniques (2nd ed.)". CRC Press. https://doi.org/10.1201/9780367802295

Hart, G. C., Sajjad, N., Kingsley, G. R., and Noland, J. L. (1989). "Analytical stress-strain curves for grouted concrete masonry." Masonry Soc. J., 8(1), 21–34.

Hassanli, R., ElGawady, M., and Mills, J. (2016). "Experimental investigation of in-plane cyclic response of unbonded-posttensioned masonry walls." Journal of Structural Engineering, 142(5), 04015171-1-15.

Kalliontzis, D., and Schultz, A. E. (2017a). "Characterizing the In-Plane Rocking Response of Masonry Walls with Unbonded Posttensioning." Journal of Structural Engineering, 143(9), 04017110.

Kalliontzis, D., and Schultz, A. E. (2017b). "Improved estimation of the reverse-cyclic behavior of fully-grouted masonry shear walls with unbonded post-tensioning." Eng. Struct., 145, 83–96.

Kurama, Y. (2005). "Seismic Design of Partially Post-Tensioned Precast Concrete Walls." PCI Journal, 50(4), 100–125.

Laursen, P. T. and Ingham, J. M. (2001). "Structural Testing of Single-Story Post-Tensioned Concrete Masonry Walls." The Professional Journal of The Masonry Society, 19(1), 69-82.

Laursen, P. T. and Ingham, J. M. (2004). "Structural testing of large-scale posttensioned concrete masonry walls." Journal of Structural Engineering, 130(10), 1497-1505.

Laursen, P. T. (2002). "Seismic analysis and design of post-tensioned concrete masonry walls." PhD Thesis, Department of Civil and Environmental Engineering, University of Auckland.

Nakaki, S.D., Stanton, J.F., Sritharan, S. (1999). "An overview of the PRESSS five-story precast concrete test building." PCI Journal, 44(2), 26–39.

Priestley, M. J. N., and Elder, D. M. (1982). "Cyclic loading tests of slender concrete masonry shear walls." Bull. N.Z. Natl. Soc. Earthquake Eng., 15(1), 3–21.

Priestley, M. J. N., and Elder, D. M. (1983). "Stress-strain curves for unconfined

and confined concrete masonry." ACI Journal, 80(19), 192–201.

Priestley, M. J. N., Sritharan, S., Conley, J.R., and Pampanin, S. (1999). "Preliminary results and conclusions from the PRESSS five-story precast concrete test building." PCI Journal, 44(6), 42–67.

Rosenboom, O. A., and Kowalsky, M. J. (2004). "Reversed in-plane cyclic behavior of posttensioned clay brick masonry walls." Journal of Structural Engineering, 10.1061/(ASCE)0733-9445(2004)130:5(787), 787–798.

Shedid, M. T., El-Dakhakhni, W. W., and Drysdale, R. G. (2010). "Alternative strategies to enhance the seismic performance of reinforced concrete-block shear wall systems." Journal of Structural Engineering, 10.1061/(ASCE)ST .1943-541X.0000164, 676–689.

TMS (The Masonry Society). (2016). "Building Code Requirements and Specification for Masonry Structures." TMS 402/602-16, Longmont, CO.

Wight, G. D., Ingham, J. M., and Kowalsky, M. J. (2006). "Shaketable Testing of Rectangular Post-Tensioned Concrete Masonry Walls." PCI Journal, 103(4), 587-595.

Yassin, A., Ezzeldin, M., Steele, T., and Wiebe, L. (2020). "Seismic collapse risk assessment of post-tensioned controlled rocking masonry walls." J. Struct. Eng., 146(5), 04020060-1-16.

Yassin, A., Ezzeldin, M., and Wiebe, L. (2018). "Evaluation of methods for

predicting the response of controlled rocking reinforced masonry walls.". Proceedings of the 10th International Masonry Conference, July 9-11, Milan, Italy.

Yassin, A., Ezzeldin, M., and Wiebe, L. (2021). "Seismic Design and Performance Evaluation for Controlled Rocking Masonry Shear Walls without Posttensioning." In preparation.

## 3.9. TABLES

**Table 3.1.** Test matrix and specimen details of ED-CRMWs.

| Wall ID | Wall type | Wall dimension LxH (mm) | Vertical bonded reinforcement | ED unbonded bar[a] | Shear reinforcement | Axial stress (MPa) | Confinement |
|---|---|---|---|---|---|---|---|
| W1 | Unconfined | 1895 x 2660 | 6D7 | 1M10@ 700mm | D4 every other course | 1.17 | none |
| W2 | End-Confined | 1895 x 2660 | 4D7@Web, 8D7 @ Ends | 1M10@ 700mm | D4 every other course | 1.17 | D4 closed ties every other course |
| W3 | Priestley plates | 1895 x 2660 | 6D7 | 1M10@ 700mm | D4 every other course | 1.17 | Plate every course @ first five courses |
| W4 | Inner ED + Priestley plates | 1895 x 2660 | 6D7 | 1M10@ 140mm | D4 every other course | 1.17 | Plate every course @ first five courses |
| W5 | High axial+ Priestley plates | 1895 x 2660 | 4D7 | 1M10@ 700mm | D4 every other course | 2.31 | Plate every course @ first five courses |
| W6 | No horizontal reinforcement | 1895 x 2660 | 6D7 | 1M10@ 700mm | none | 1.17 | Plate every course @ first five courses |

[a] Relative to wall centerline

**Table 3.2.** Damage sequence for the ED-CRMWs

| | Drift corresponding to damage state sequence[a] | | | | | | |
|---|---|---|---|---|---|---|---|
| Wall ID | Initiation of rocking joint gap opening | Onset of ED yielding | Initiation of vertical cracks at first course (wall toes) | Initiation of face shell spalling at first course (wall toes) | Face shell Spalling at first course (wall toes) | Crushing of core grout first course (wall toes) | Fracture of ED |
| W1 | 0.06% | 0.22% | 0.45% | 0.90% | 1.25% | 1.90% | 2.80% |
| W2 | 0.06% | 0.22% | 0.68% | 1.00%[b] | N.A.[c] | N.A. | 2.40% |
| W3 | 0.06% | 0.22% | 0.64% | 0.90% | 1.25% | 1.60% | 2.30% |
| W4 | 0.06% | 0.46% | 0.64% | 1.00% | 1.60% | 2.25% | 2.60% |
| W5 | 0.09% | 0.35% | 0.64% | 0.90% | 1.25% | 1.60% | N.A. |
| W6 | 0.06% | 0.22% | 0.46% | 0.64% | 0.90% | 1.25% | 1.90% |

[a] No evidence of any tension or diagonal shear cracks.
[b] Superficial face shell peeling.
[c] Only at wall web at the ED locations due to ED bar buckling at 1.60% drift.

**Table 3.3.** Summary of displacements, displacement ductility, predicted and measured strength

| **Wall** | **Wall type** | **Direction** | $\Delta_y$ **(mm)** | $\Delta_u$ **(mm)** | $\Delta_{0.8u}$ **(mm)** | $\mu_{0.8u}$ | $Q_{pr}$ **(kN)** | $Q_{exp}$ **(kN)** | $Q_{pr}/Q_{exp}$ |
|---|---|---|---|---|---|---|---|---|---|
| W1 | Unconfined | Push | 5.7 | 32.1 | 50.2 | 8.8 | 92.3 | 92.5 | 0.99 |
| | | Pull | 5.9 | 38.5 | 51.7 | 8.7 | 92.3 | 93.0 | 0.99 |
| W2 | End-Confined | Push | 4.7 | 58.1 | 58.1 | 12.4 | 97.5 | 104.1 | 0.94 |
| | | Pull | 4.5 | 58.2 | 58.2 | 12.9 | 97.5 | 104.5 | 0.93 |
| W3 | Priestley plates | Push | 5.4 | 30.2 | 47.7 | 8.8 | 92.3 | 93.6 | 0.98 |
| | | Pull | 5.8 | 31.5 | 48.8 | 8.4 | 92.3 | 95.1 | 0.97 |
| W4 | Inner ED + Priestley plates | Push | 8.3 | 33.1 | 54.9 | 6.6 | 92.3 | 91.2 | 1.01 |
| | | Pull | 8.5 | 32.8 | 53.2 | 6.3 | 92.3 | 94.3 | 0.98 |
| W5 | High axial+ Priestley plates | Push | 8.2 | 29.8 | 48.9 | 5.9 | 144.0 | 150.7 | 0.95 |
| | | Pull | 7.9 | 22.7 | 40.1 | 5.1 | 144.0 | 149.5 | 0.96 |
| W6 | No horizontal reinforcement | Push | 5.8 | 23.4 | 44.9 | 7.7 | 92.3 | 95.9 | 0.96 |
| | | Pull | 5.9 | 18.2 | 45.3 | 7.6 | 92.3 | 97.6 | 0.94 |

## 3.10. FIGURES

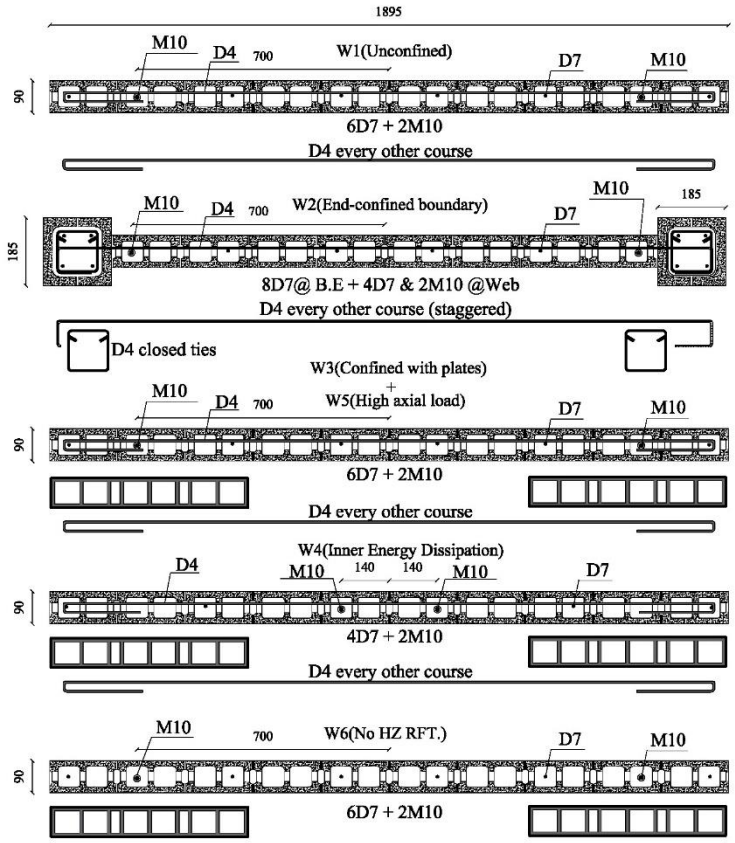


**Fig. 3.1.** ED-CRMWs cross-section and reinforcement details (all dimensions are in mm).

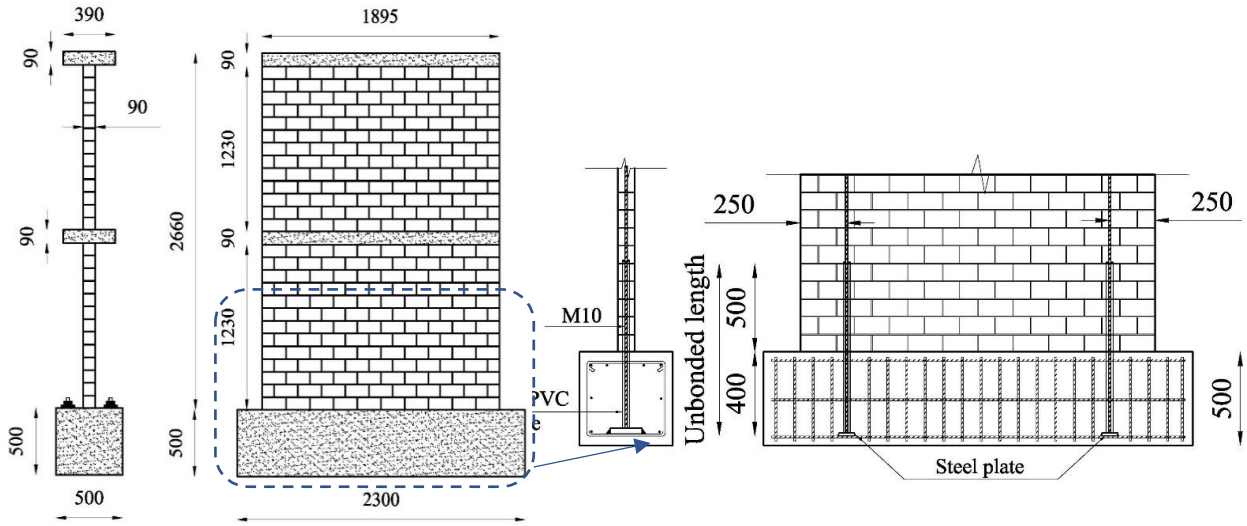


**Fig. 3.2.** Energy dissipation connection inside the walls (all dimensions are in mm).

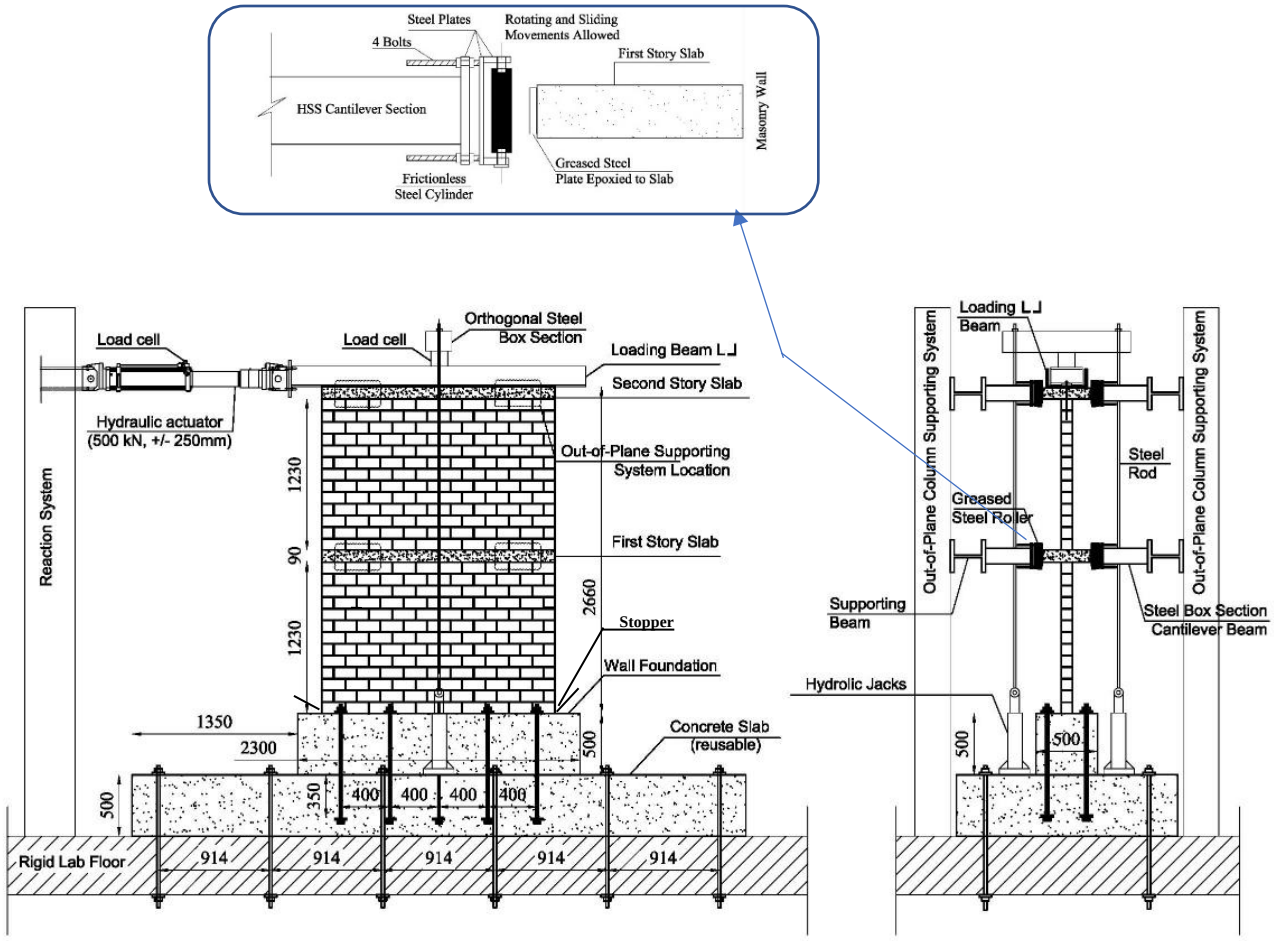


**Fig. 3.3.** Test setup (all dimensions are in mm)

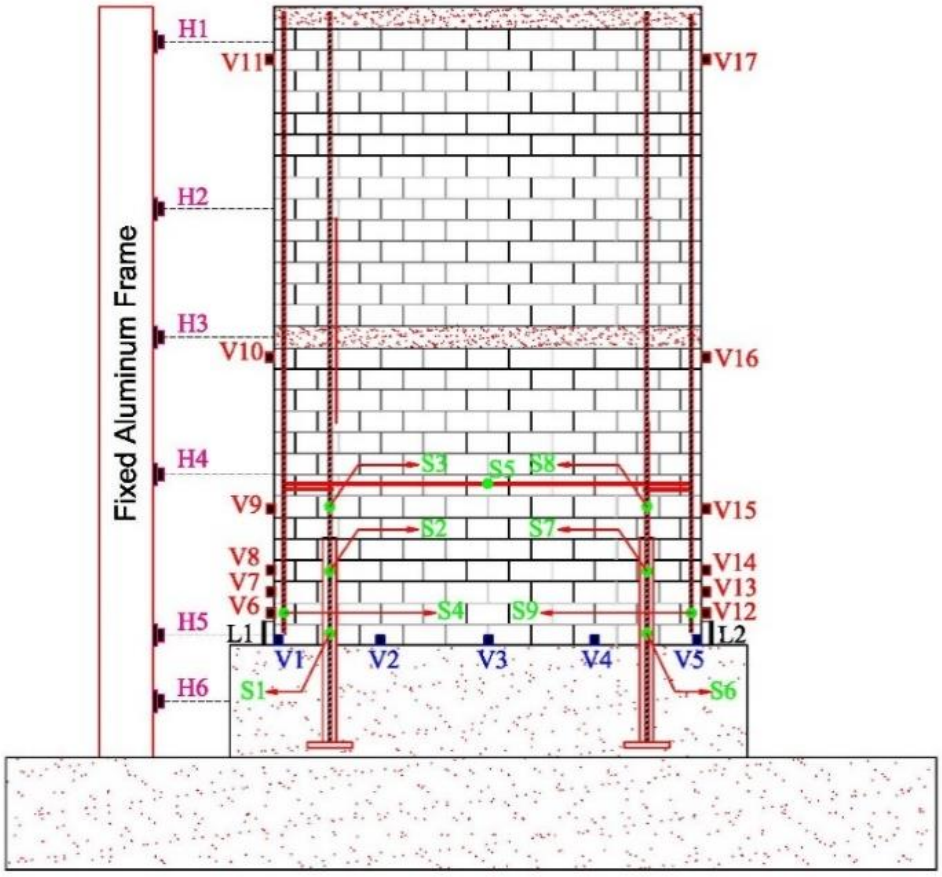


**Fig. 3.4.** Typical wall instrumentation (all dimensions are in mm)

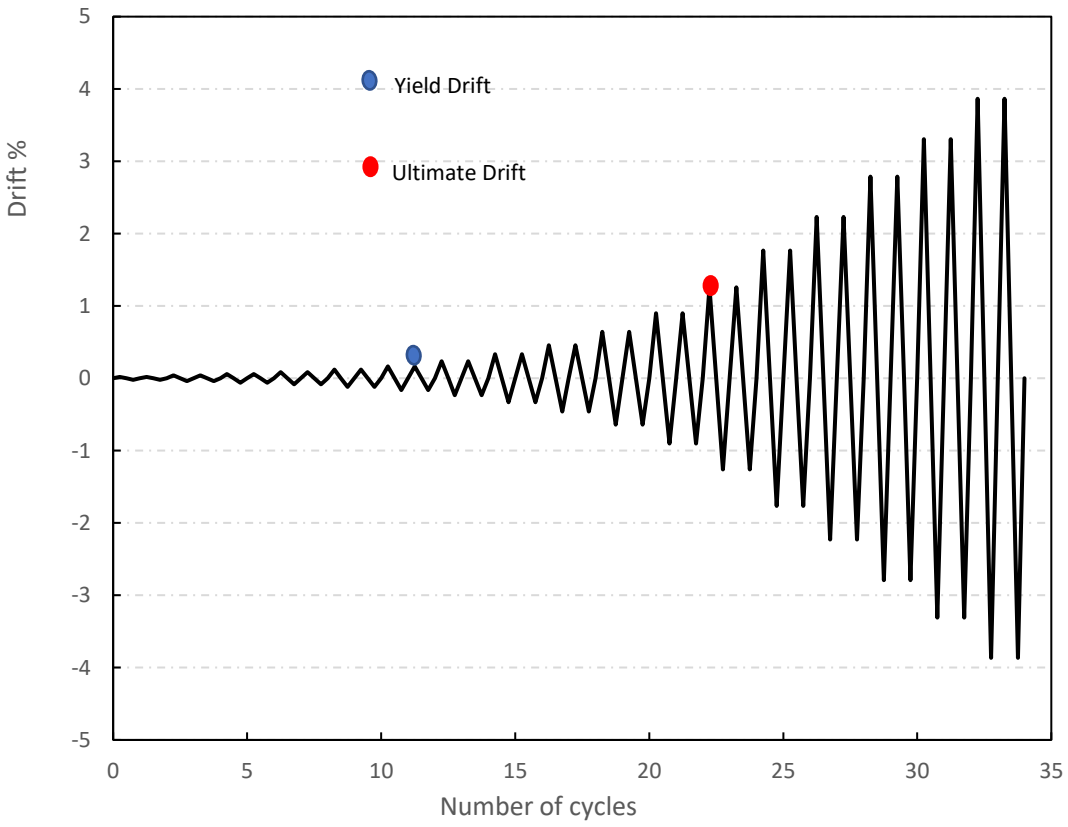


**Fig. 3.5.** Loading protocol.

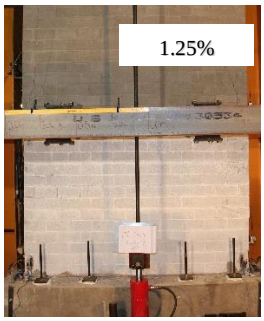
1.25%


2.80% drift

a) W1

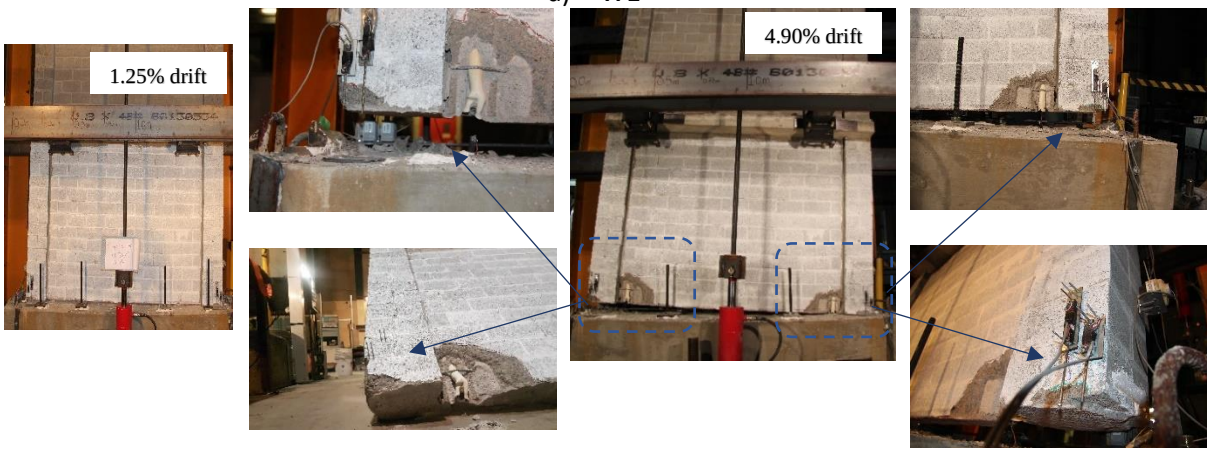
1.25% drift
4.90% drift

b) W2


1.25% drift
2.60% drift
McMaster University
McMaster University

c) W3

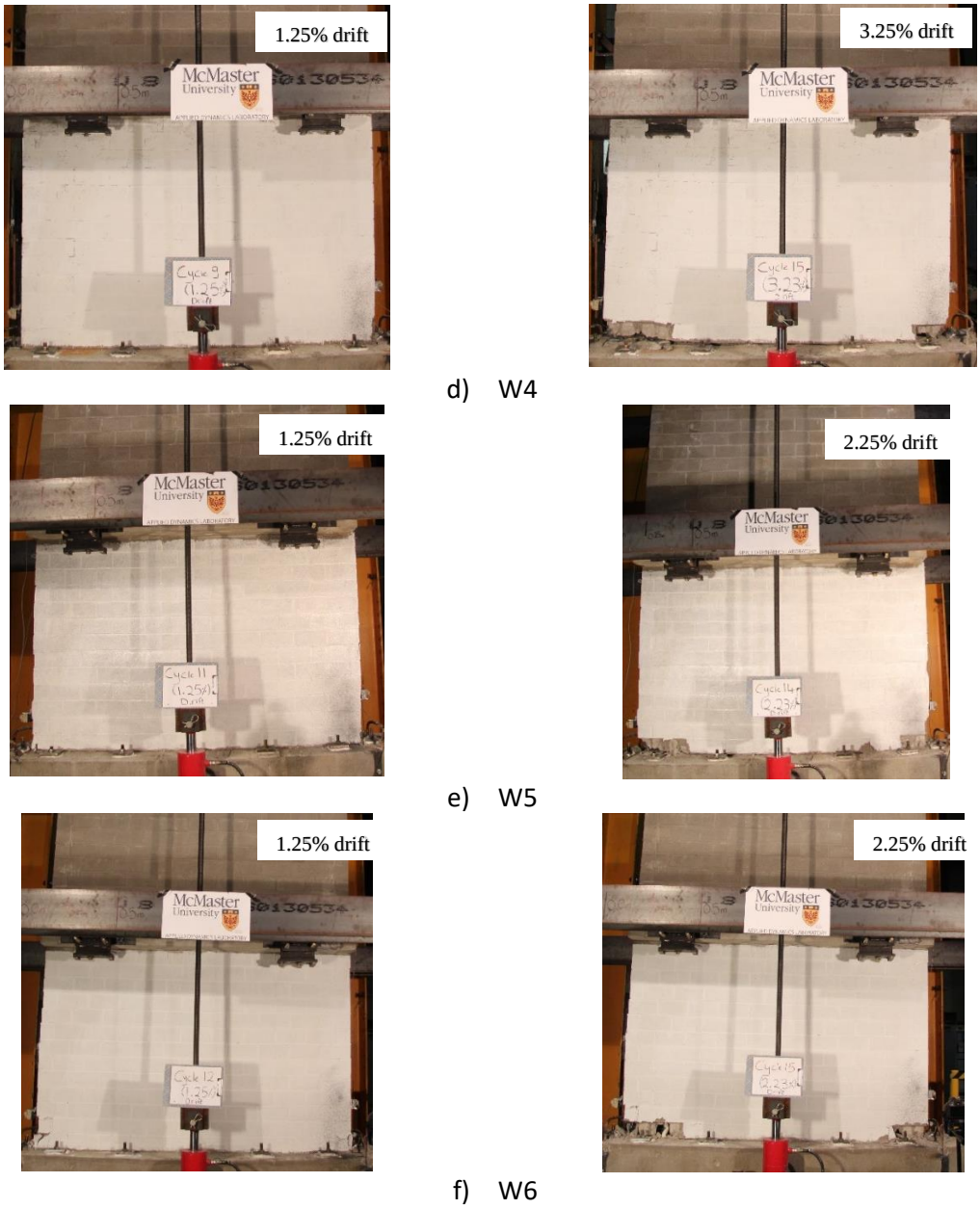


**Fig. 3.6.** Damage at 1.25% drift ratio and at last testing drift for all walls.

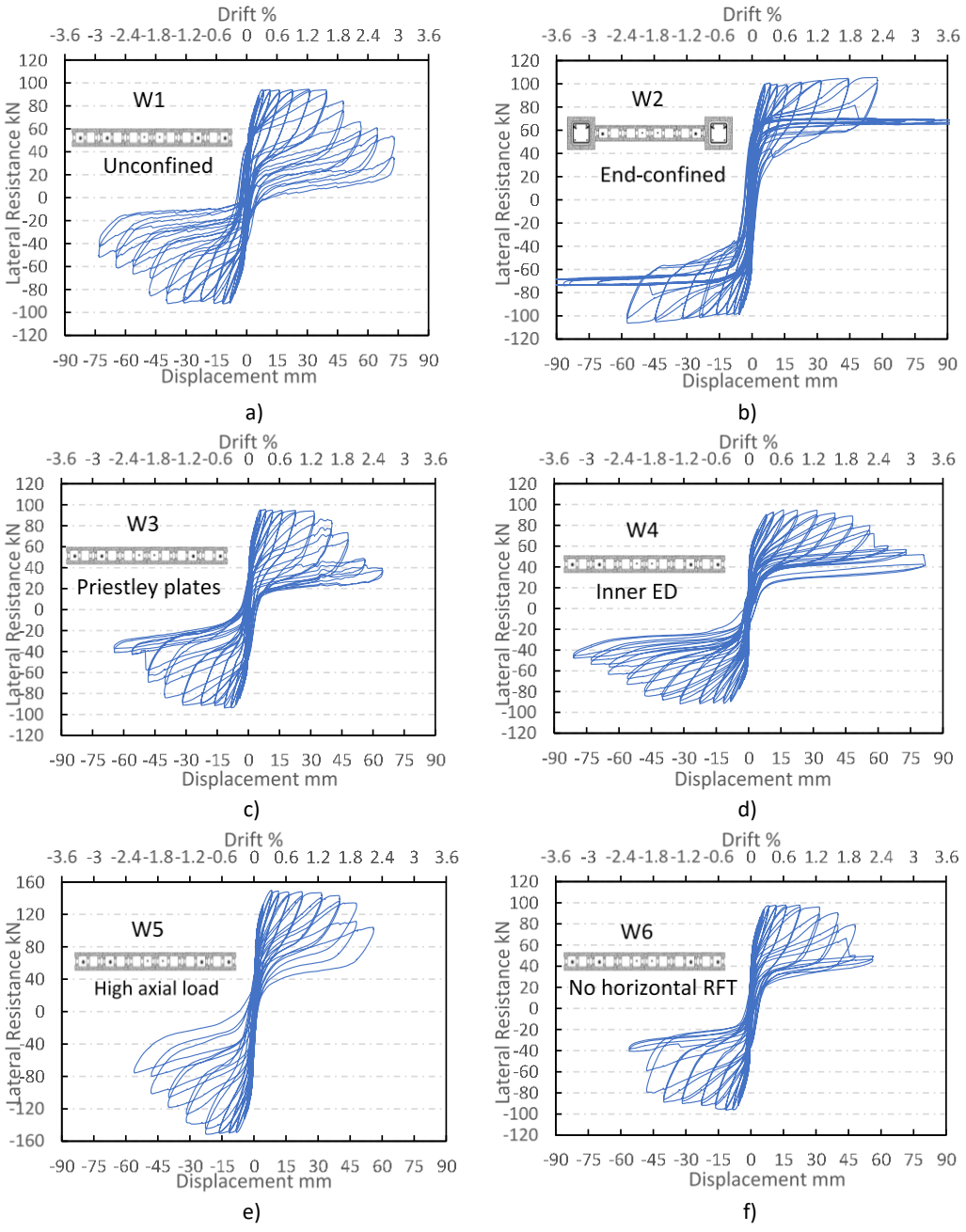


**Fig. 3.7.** Load-displacement hysteresis loops for all six walls

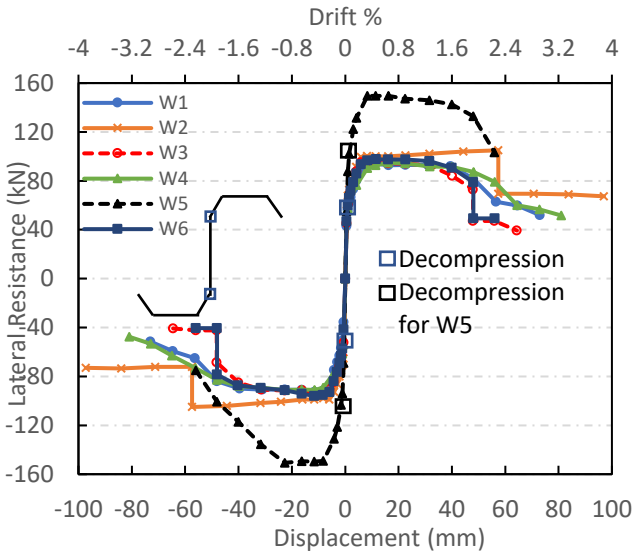


**Fig. 3.8.** Envelope response for all six walls

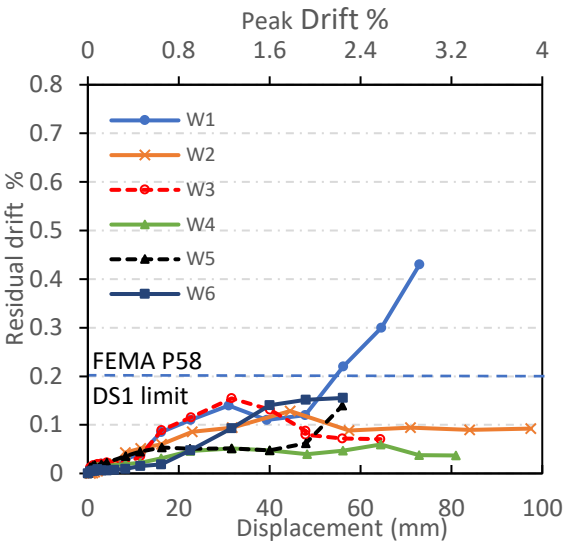


**Fig. 3.9.** Residual drift for all six walls

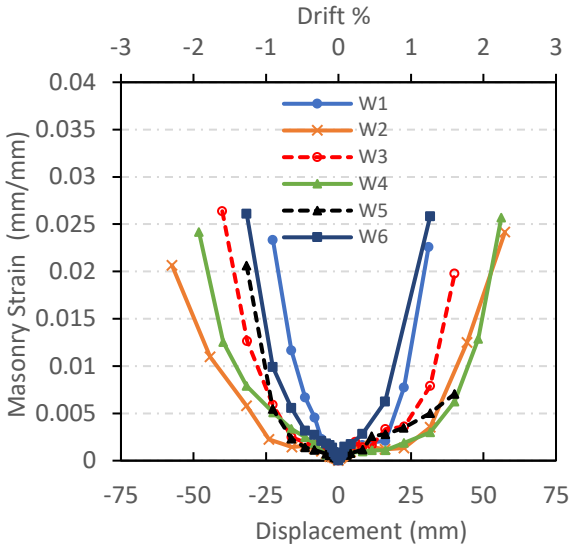


**Fig. 3.10.** Masonry compressive strains at different displacement amplitudes

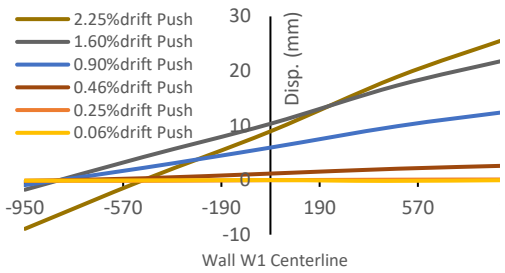
2.25%drift Push
1.60%drift Push
0.90%drift Push
0.46%drift Push
0.25%drift Push
0.06%drift Push
Disp. (mm)
Wall W1 Centerline

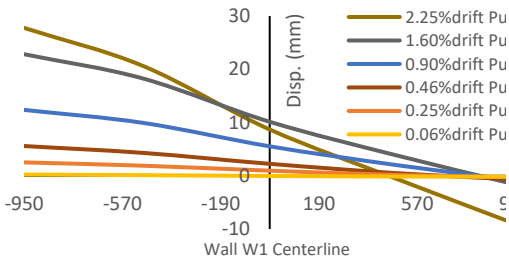
2.25%drift Pu
1.60%drift Pu
0.90%drift Pu
0.46%drift Pu
0.25%drift Pu
0.06%drift Pu
Disp. (mm)
Wall W1 Centerline

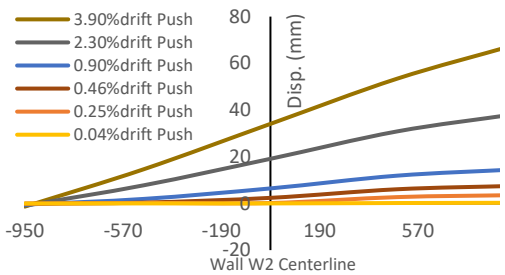
3.90%drift Push
2.30%drift Push
0.90%drift Push
0.46%drift Push
0.25%drift Push
0.04%drift Push
Disp. (mm)
Wall W2 Centerline

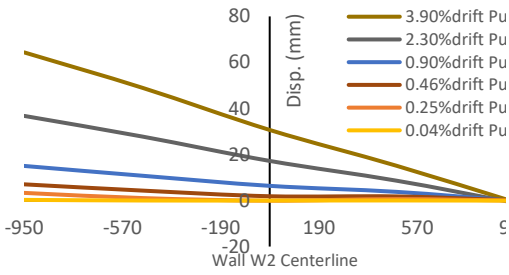
3.90%drift Pu
2.30%drift Pu
0.90%drift Pu
0.46%drift Pu
0.25%drift Pu
0.04%drift Pu
Disp. (mm)
Wall W2 Centerline

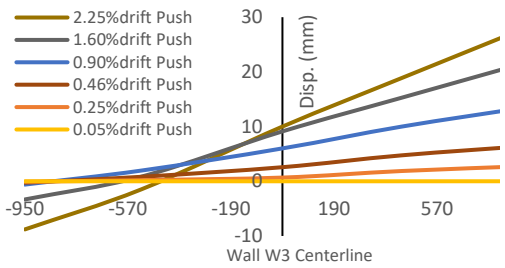
2.25%drift Push
1.60%drift Push
0.90%drift Push
0.46%drift Push
0.25%drift Push
0.05%drift Push
Disp. (mm)
Wall W3 Centerline

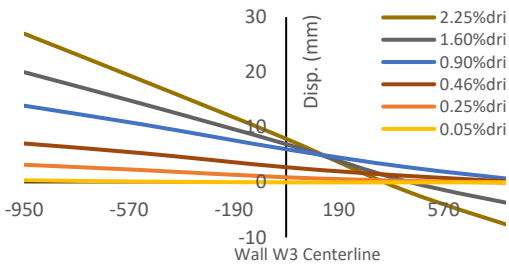
2.25%dri
1.60%dri
0.90%dri
0.46%dri
0.25%dri
0.05%dri
Disp. (mm)
Wall W3 Centerline

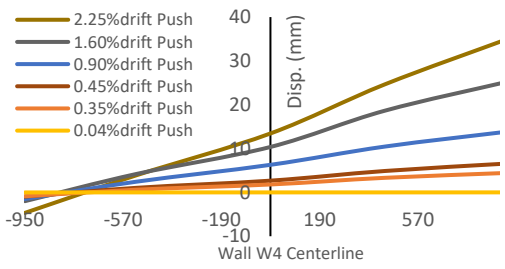
2.25%drift Push
1.60%drift Push
0.90%drift Push
0.45%drift Push
0.35%drift Push
0.04%drift Push
Disp. (mm)
Wall W4 Centerline

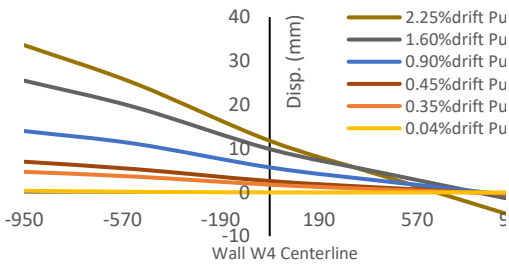
2.25%drift Pu
1.60%drift Pu
0.90%drift Pu
0.45%drift Pu
0.35%drift Pu
0.04%drift Pu
Disp. (mm)
Wall W4 Centerline

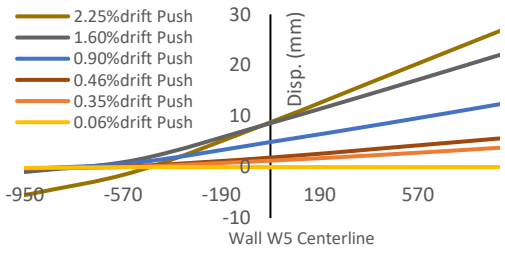
2.25%drift Push
1.60%drift Push
0.90%drift Push
0.46%drift Push
0.35%drift Push
0.06%drift Push
Disp. (mm)
Wall W5 Centerline

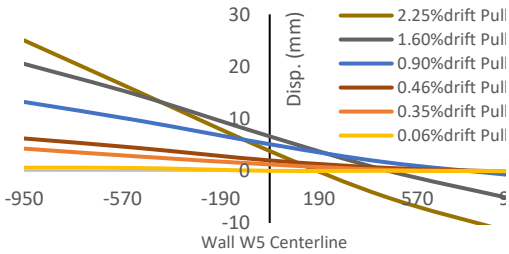
2.25%drift Pull
1.60%drift Pull
0.90%drift Pull
0.46%drift Pull
0.35%drift Pull
0.06%drift Pull
Disp. (mm)
Wall W5 Centerline

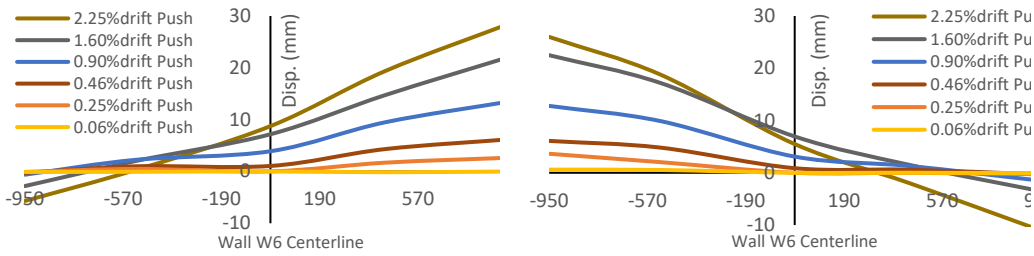


**Fig. 3.11.** Base crack profile for all six walls in both push and pull directions

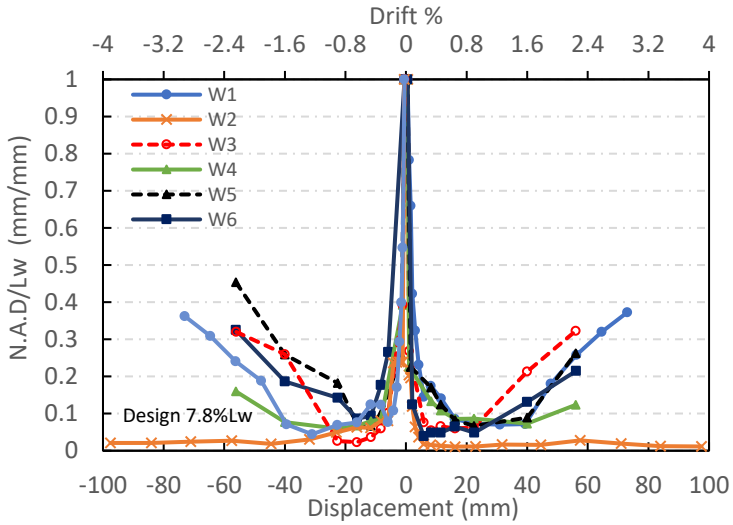


**Fig. 3.12.** Neutral axis depth variation with drift

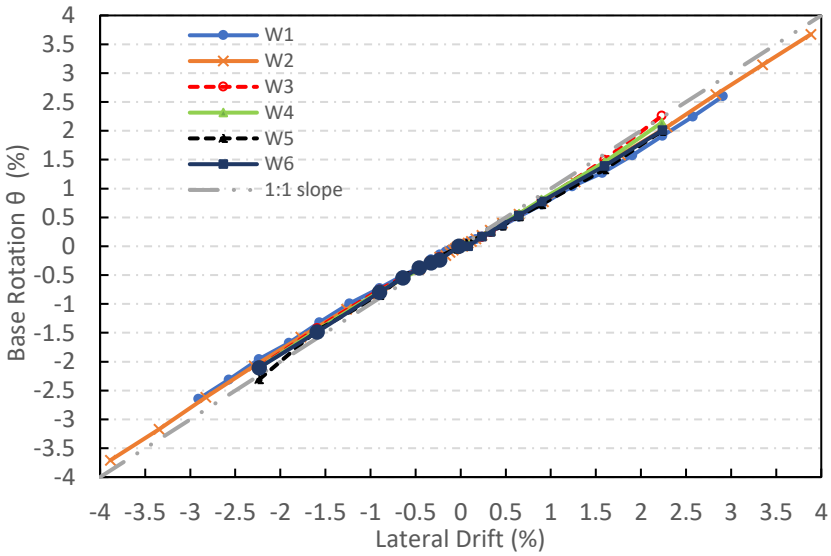


**Fig. 3.13.** Base rotation variation with lateral drift

# Chapter 4

# SEISMIC DESIGN AND PERFORMANCE EVALUATION OF CONTROLLED ROCKING MASONRY SHEAR WALLS WITHOUT POSTTENSIONING

## 4.1. ABSTRACT

Unbonded post-tensioned controlled rocking masonry walls (PT-CRMWs) have been increasingly studied in the last decades due to their promising results regarding seismic resilience. However, implementing post-tensioning (PT) has some drawbacks, such as construction challenges, PT losses, and yielding during a seismic event. In response, this study investigates a newly proposed energy dissipation-controlled rocking masonry wall (ED-CRMW), which eliminates the use of unbonded post-tensioned bars and relies instead on gravity loads to self-center the wall to its vertical plumb, while incorporating an energy dissipation (ED) device to limit seismic displacements. The study presents a design approach for the proposed system including the influence of higher mode effects. To assess the effectiveness of the design approach, a multi-spring macro model is developed using OpenSees and then validated against the experimental presented earlier in chapter 3. Next, as no distinct values are yet provided in ASCE 7, the seismic response modification factor is investigated using collapse risk analysis. Specifically, using the validated model, nonlinear static and dynamic analyses are performed to 20 ED-CRMW archetypes with different design configurations. The results demonstrate that the design objectives were achieved and that a seismic

response modification factor of 7 assigned to the selected design configurations meets the FEMA P695 acceptance criteria for seismic collapse risk under the maximum considered earthquake (MCE).

## 4.2. INTRODUCTION

Current codes aim to ensure that the life safety of occupants is preserved during major earthquakes, but economic losses due to damage to code-compliant buildings demonstrate a lack of seismic resilience. In this regard, rocking systems have been increasingly studied and are considered as a promising seismic force-resisting system for resilient buildings (Priestley et al. 1999; Rosenboom and Kowalsky 2004). This is attributed to their ability to withstand major earthquakes with minimal residual drifts and with limited structural damage concentrated at the rocking base interface (Kurama et al. 1999). This, in turn, is favorable for modern resilient cities because it minimizes the costs associated with service shutdown for structural repairs or replacement. Such behavior has been proven through several experimental studies of masonry walls, where unbonded post-tensioned controlled rocking masonry walls (PT-CRMWs) were tested under quasi-static (Laursen and Ingham 2004; Hassanli et al. 2016) and dynamic (Wight et al. 2006; Kalliontzis and Sritharan 2020) loading. In general, PT-CRMWs responded with a rocking behavior characterized by local damage at the wall toes coupled with low residual drifts.

In a controlled rocking masonry wall (CRMW), softening of the force-deformation response is achieved through an elastic gap opening mechanism (rocking at the base), thus replacing the typical yielding of reinforcement in a conventional fixed masonry shear wall. This rocking is initiated when the base overturning moment caused by lateral load exceeds the decompression moment capacity, and hence the wall uplifts from the foundation and a single horizontal crack at the wall-foundation interface is then formed. In a PT-CRMW, the restoring force of post-tensioning (PT) restores the wall to its vertical plumb alignment. This mechanism is called the self-centering ability of the system.

Despite the aforementioned advantages of using unbonded PT tendons, their implementation in masonry construction practice is challenging due to the high compression demand on the wall when the PT force is combined with dead and live loads, especially due to the low crushing strain of masonry compared to that of concrete due to lack of confinement. Also, PT losses and PT yielding reduce the self-centering ability (Hassanli et al. 2016). As such, a new controlled rocking wall system without PT, named energy dissipation-controlled rocking masonry walls (ED-CRMWs), was recently proposed by Yassin et al. (2021a). The ED-CRMWs are designed such that their gravity loads, instead of unbonded PT, are responsible for self-centering the system. In addition, to increase the energy dissipation (ED), strength and positive post-yield stiffness of the wall, an ED device is used. This configuration increases the seismic resilience of the system by concentrating major damage in the ED device while minor damage occurs in the masonry. Also,

minimum vertical bonded reinforcement that does not cross the rocking interface is used to maintain the wall integrity during rocking and satisfy the standard design requirements for seismic detailing. Such configuration was recently reported by Yassin et al. (2021a) by testing six ED-CRMWs with internal axial yielding unbonded ED bars, where all tested walls showed very low residual drifts and localized damage only at the wall toes, as shown in Fig. 4.1a.

Building on these promising results, the current chapter presents a seismic design approach for the newly proposed ED-CRMWs. Although some guidelines are available for controlled rocking concrete walls (ACI ITG-5.2 2009), no design approach for controlled rocking masonry walls is currently provided in relevant North American standards. In this regard, a detailed design approach for the ED-CRMWs system is presented, including consideration of higher mode effects. Subsequently, a numerical macro model is developed using OpenSees (McKenna et al. 2000) and validated against previous experimental results (Yassin et al. 2021a). Afterwards, 20 ED-CRMW archetypes, representing 4-, 6- and 8-story structures, with axial yielding ED bars are designed following the proposed design approach and subjected to a suite of 44 ground motions recommended by the FEMA P695 methodology (FEMA 2009) for collapse analysis. Finally, the design approach is evaluated and the influence of the response modification factor, $R$, the amount of ED, $\kappa$, and the level of axial compression, $\rho_P$ , on the collapse risk is reported.

## 4.3. DESIGN METHODOLOGY

This section presents a design approach and recommendations for ED-CRMWs, with the goal of achieving low residual drifts and localizing damage at the wall base rocking joint. The proposed design criteria are intended to achieve a nonlinear response only at the base rocking joint at the design earthquake (DE) level, corresponding to a 10% probability of exceedance in 50 years, while the wall body is designed to have localized damage at the rocking toes only. At this intensity level, the wall body vertical reinforcement (see Fig. 4.1b), and the masonry at the outermost fiber along the wall height both remain within the elastic range. Then, at the maximum considered earthquake (MCE) level, the wall body vertical reinforcement is allowed to yield in flexure due to higher mode effects if they produce sufficient demands, as the yielding will contribute to mitigating these effects. This is similar to the dual-plastic hinge concept proposed by Panagiotou and Restrepo (2009). To achieve this intended response, the wall base rocking joint including the ED is designed first, followed by designing of capacity-protected elements, similar to the design framework proposed by Wiebe and Christopoulos (2015a) for controlled rocking steel braced frames. A flow chart for the design is presented in Fig. 4.2.

### 4.3.1. DESIGN OF BASE ROCKING JOINT

To ensure rocking with self-centering behavior, the design starts by selecting a value for $\kappa$, which is defined by Kurama (2005) as the ratio of the moment

contribution of ED ($M_{ED}$) to the moment contribution due to restoring force (i.e., gravity load, $W$) ($M_W$). The selected value of $\kappa$ should be less than 1.0 to ensure self-centering after the lateral load is released, and more than 0.2 to ensure sufficient system damping (Smith et al. 2012). Next, the ED yielding force ($Q_{yED}$) is preliminarily calculated from Eq. 4.1, which assumes that the ED is located at the end of the wall length.

$$Q_{yED} = \kappa \frac{W}{2} \tag{4.1}$$

This equation satisfies the requirement of closing the rocking gap after the seismic motion (ACI ITG-5.2 2009), where the gravity load, $W$, is always greater than the maximum compressive force that develops in the ED. The value of $W$ is calculated from the critical load combination of 0.9D + 1.0E, as per ASCE/SEI 7-16 (ASCE/SEI 2016). The equivalent compression stress block depth, $a$, is then calculated from equilibrium using Eq. 4.2.

$$a = \frac{Q_{yED} + W}{\alpha f_m^{'} b} \tag{4.2}$$

where $\alpha$ is the equivalent stress block parameter (taken as 0.8 as per TMS 2016), $f_m^{'}$ is the masonry compressive strength, and $b$ is the wall thickness. Subsequently, the minimum wall length, $L_w$, is calculated using Eq. 4.3 to ensure that the base rocking joint moment capacity, $M_{Rock}$, is greater than or equal to the factored moment, $M_f$, calculated from structural analysis under the earthquake loads calculated using the $R$ value recommended at the end of this study.

$$L_w \geq \frac{2M_f}{W(1+\kappa)} + a\left(\frac{1+\kappa/2}{1+\kappa}\right) \tag{4.3}$$

Afterwards, the exact location of the ED force $Q_{yED}$ relative to the wall outermost compression fiber is selected and defined as $d_{ED}$. This allows a detailed verification of the ED design. For instance, the examples in this chapter use unbonded axial yielding ED bars as the ED device. In this case, the bar area, $A_{ED}$, is calculated to ensure that the base rocking joint moment capacity, $M_{Rock}$, is greater than the factored moment, $M_f$, as shown in Eq. 4.4:

$$M_{Rock} = M_{ED} + M_W = A_{ED} f_{yED}(d_{ED} - a/2) + W(\frac{L_w - a}{2}) \geq M_f \quad (4.4)$$

where $f_{yED}$ is the yield stress of the unbonded axial yielding ED bars.

The next step is to calculate the wall drift demands at the design level, $\Delta_d$, which corresponds to the DE level. This drift is determined using Eq. 4.5, and shall not exceed two-thirds of the maximum drift of 3% as per ACI ITG-5.2 (2009).

$$\Delta_d = \Delta_e \frac{RC_R}{I_e} \quad (4.5)$$

where $\Delta_e$ is the linear-elastic drift under the design base shear force, $V_d$, shown in Fig. 4.3 that represents a schematic for the backbone curve of wall response, while $I_e$ is the importance factor. The response modification factor $R$ is used instead of the deflection amplification factor, $C_d$, as recommended by FEMA P695 (FEMA 2009). In addition, considering that the equal displacement assumption is often not conservative for self-centering systems, this displacement is multiplied by a displacement ratio factor, $C_R$, found by regression for systems with a flag-shaped hysteresis and 5% initial stiffness proportional damping (Zhang et al. 2018) and calculated using Eq. 4.6:

$$C_R = 1+(R-1)^{0.515}\frac{0.184+0.119(1-\beta)^{1.173}}{T_1^{1.478}} \quad (4.6)$$

where $T_1$ is the initial period, $\beta$ is the ED ratio calculated as the ratio between twice the moment contribution due to ED ($M_{ED}$), and the total rocking moment due to gravity load ($M_W$) and ED ($M_{ED}$). The relation between $\beta$ and $\kappa$ is shown in Eq. 4.7.

$$\beta = \frac{2\kappa}{1+\kappa} \quad (4.7)$$

At the design-level drift, $\Delta_d$, the unbonded axial yielding ED bars are intended to reach a tensile strain $\varepsilon_{sD}$ of at least $4\varepsilon_y$ to ensure sufficient base rotation ductility and sufficient yielding before masonry crushing as per TMS (2016) for special reinforced masonry walls, while the outermost fiber of masonry rocking base toe has just reached the maximum usable strain of 0.0025. At the same time, $\varepsilon_{sD}$ must be less than a limiting strain of $0.85\varepsilon_{su}$, where $\varepsilon_{su}$ is the monotonic strain capacity at the peak strength of the ED bar, to prevent low cycle-fatigue fracture of ED bars before masonry crushing as per ACI ITG-5.2 (2009). To achieve these criteria, the unbonded length ($L_{un}$) of the axial yielding ED bars is calculated using Eq. 4.8:

$$L_{un} = \frac{(d_{ED}-c)\theta_d}{\varepsilon_{sD}} \quad \text{where, } 4\varepsilon_y \le \varepsilon_{sD} < 0.85\varepsilon_{su} \quad (4.8)$$

where $c$ is the length of compression zone which equals $a$ divided by 0.8 (TMS 2016), and $\theta_d$ is the base rotation at the design drift, assumed to be equal to $\Delta_d$ divided by the wall height based on several experimental (Yassin et al. 2021a; Hassanli et al. 2016) and analytical (Kalliontzis and Schultz 2017) studies. A development length beyond the unbonded length of the ED bars must be provided

and bonded with the surrounding grout region, as shown in Fig. 4.1b, to prevent bond slip failure. Finally, checks are needed to ensure positive post-yield rotational stiffness, $\gamma$, and gap closure. The post-yield rotational stiffness, $\gamma$, is calculated as the net difference between positive stiffness attained due to ED hardening, $\gamma_2$, and the negative wall stiffness that would occur if no ED were incorporated into the system, $\gamma_1$, as shown in Fig. 4.3. Both stiffnesses, $\gamma_1$ and $\gamma_2$, are calculated as shown in Eq. 4.9 and 4.10, respectively.

$$\gamma_1 = \frac{M_{decomp}}{\psi} = \frac{\left[W\, L_w/6\right]}{\left[0.5(L_w - a)/H\right]} = \frac{WL_wH}{3(L_w - a)} \tag{4.9}$$

$$\gamma_2 = \frac{M_d - M_y}{\theta_d - \theta_y} = \frac{(\varepsilon_{sD} - \varepsilon_y)E_2A_{ED}(d_{ED} - 0.5a)}{(\varepsilon_{sD} - \varepsilon_y)\dfrac{L_{un}}{(d_{ED} - 1.25a)}} = \frac{E_2A_{ED}}{L_{un}}(d_{ED} - 0.5a)(d_{ED} - 1.25a) \tag{4.10}$$

where $M_{decomp}$ is the moment resistance when the wall is about to uplift, $\psi$ is the instability base rotation angle based on the conservative assumption that the weight is concentrated at the top story, as shown in Fig. 4.3, $E_2$ is the post-yield steel modulus for the ED bars, and $M_d$ and $M_y$ are the moments at the design drift and onset of ED yielding, respectively, as shown in Fig. 4.3. In deriving Eq. 4.10, the equivalent stress block depth, $a$, is assumed to have the same value at the design and yielding stages.

Finally, to ensure that the gap closes in the return cycle, the maximum force developed in the ED, which is the bar ultimate tensile strength, $f_u$, multiplied by its cross-section area, $A_{ED}$, should be less than the minimum gravity load, $W$, as shown in Eq. 4.11, as per ACI ITG-5.2 (2009).

$$\frac{Q_{uED}}{W} = \frac{f_u A_{ED}}{W} < 1 \tag{4.11}$$

## *4.3.2.* DESIGN OF CAPACITY-PROTECTED ACTIONS

### 4.3.2.1 DESIGN OF WALL BODY VERTICAL REINFORCEMENT

To satisfy the intended performance, checks are performed at both the DE and the MCE levels. At the DE level, to constrain nonlinear behavior to the base rocking joint, both the vertical body bonded reinforcement and the outermost masonry fiber stress along the full wall height (except at the base rocking joint) should remain within the elastic range, so as to avoid any spread of damage into the wall body. To achieve this performance criterion, the demand moment at the DE level, $M_{demand}(z)$, must be less than the elastic moment capacity, $M_{pmc}$.

The demand moment is calculated at the critical location over the height ($z$) where the higher modes produce the maximum total overturning moment, $M_{demand}(z)$. Closed-form equations proposed by Wiebe and Christopoulos (2015b) for quantifying the contribution of higher modes to the overturning moment response in controlled rocking systems, assuming uniform mass and stiffness, are used in this chapter as presented in Eq. 4.12. Finally, the demand moment is the summation of the overstrength first mode and higher modes as shown in Eq. 4.13.

$$M_{2,\max}(\mathrm{z}) = 0.0282H\left(\frac{W_{trib}}{g}\right) S_a\left(\frac{T_1}{3}\right)\left|\sin\left(\frac{4.49z}{H}\right) + \left(\frac{0.976z}{H}\right)\right|$$

$$M_{3,\max}(\mathrm{z}) = 0.00384H\left(\frac{W_{trib}}{g}\right) S_a\left(\frac{T_1}{5}\right)\left|\sin\left(\frac{7.73z}{H}\right) - \left(\frac{0.991z}{H}\right)\right| \tag{4.12}$$

$$M_{demand}(z) = \Omega M_1(z) + \sqrt{M_2^2(z) + M_3^2(z)} \quad (4.13)$$

where $W_{trib}/g$ is the tributary seismic mass carried by the wall, $S_a$ is the elastic (i.e., $R$=1) spectral acceleration at the DE level, $z$ is the elevation along the wall height, $H$, starting from the base, $T_1/3$ and $T_1/5$ are estimates of the second-mode and third-mode periods $T_2$ and $T_3$, respectively, and $\Omega M_1(z)$ is the overstrength moment, defined as the maximum moment expected to develop over the height following the first-mode lateral load distribution (ASCE/SEI 7-16), where $M_1$ is the first mode demand moment (i.e., $M_1(z=0)$ is $M_f$).

The elastic moment capacity, $M_{pmc}$, is defined as the moment required to make the stress in the outermost vertical body bonded reinforcement bar reach $f_y$, or the stress in the outermost masonry compression fiber reach 45% of the masonry compressive strength, $f_m^{'}$, as recommended by TMS (2016). The value of $M_{pmc}$ is calculated using linear elastic sectional analysis at the critical height where the demand moment, $M_{demand}(z)$, is expected to be maximum at the DE level. This procedure ensures that adequate vertical reinforcement is provided to ensure no damage in the wall body occurs at the DE level.

At the MCE level, wall body vertical reinforcement yielding is allowed as a second source of nonlinearity at the critical location where $M_{demand}$ at the MCE level is maximum. In this case, $M_{demand}$ is calculated using Eq. 4.13, but with the second- and third-mode overturning moments $M_2$ and $M_3$ calculated using the elastic spectral acceleration at the MCE level in Eq. 4.12. In this regard, the nominal

moment capacity, $M_n$, is calculated and divided by the demand moment, $M_{demand}$, at the MCE level. The ratio $M_n / M_{demand}$ is checked to be equal to or more than unity so that yielding or crushing will occur only at the MCE level or higher intensities at the critical location where $M_{demand}$ is maximum.

Finally, to achieve the rocking mechanism at the wall-foundation interface and maintain the self-centering ability of the wall, the wall body vertical reinforcement is not extended into the foundation, similar to PT-CRMWs (Kalliontzis et al. 2019). Subsequently, vertical reinforcement is not considered as contributing to the wall lateral resistance until a distance of the development length, $L_d$, above the foundation interface, as shown in Fig. 4.1b. In this regard, the ED force and axial gravity load are considered to be the only resisting forces within a height of $L_d$ from the wall base, and thus the unbonded length of the ED bar, $L_{un}$, must be extended beyond $L_d$ of the vertical reinforcement as a curtailment requirement for the ED-CRMW system.

#### 4.3.2.2 DESIGN FOR SHEAR

The wall is capacity designed to prevent shear failure. In the TMS (2016) seismic provisions, the shear strength must be greater than both the shear demand under the DE level and the shear force corresponding to 1.25 times the wall nominal moment capacity, $M_n$. However, this requirement does not fully account for higher mode effects, as the base rocking joint in a rocking wall is the only source of nonlinearity at DE, and this only limits the first mode while the higher modes continue to increase with increasing seismic intensity (Yassin et al. 2020, Wiebe and

Christopoulos 2015b). In this chapter, the higher modes contributing to shear demand are accounted for at the MCE level (1.5 times the DE level). In the proposed procedure, the shear demand, $V_{demand}$, shown in Eq. 4.14, is the combination of the overstrength first mode, $\Omega V_1$, and the higher modes calculated using the closed-form equations introduced by Wiebe and Christopoulos (2015b) as shown in Eq. 4.15 using an elastic response spectrum (i.e., $R$=1) at the MCE level for $S_a(T)$.

$$V_{demand} = \Omega V_1 + \sqrt{V_2^2 + V_3^2} \tag{4.14}$$

$$V_{2,\max}(z) = 0.1265\left(\frac{W_{trib}}{g}\right) S_a\left(\frac{T_1}{3}\right)\left|\cos\left(\frac{4.49z}{H}\right) + 0.217\right|$$

$$V_{3,\max}(z) = 0.0297\left(\frac{W_{trib}}{g}\right) S_a\left(\frac{T_1}{5}\right)\left|\cos\left(\frac{7.73z}{H}\right) - 0.1283\right| \tag{4.15}$$

Finally, the nominal shear strength, $V_n$, calculated based on TMS (2016), should be greater than the shear demand, $V_{demand}$.

## 4.4. MODELING OF ED-CRMW SYSTEM

### 4.4.1. MODEL DESCRIPTION

To evaluate the ability of the design approach to ensure the intended seismic performance of ED-CRMWs, a numerical macro model is developed using *OpenSees* (McKenna et al. 2000) and then validated with previous experimental results (Yassin et al. 2021a). Following several previous studies (Buddika and Wijeyewickrema 2016; Pennucci et al. 2009) that have used a multi-spring macro-modeling approach for controlled rocking concrete shear walls, the multi-spring

macro-model described by Yassin et al. (2020) was adapted for the current study. The most significant differences here are that no PT is needed and that nonlinear beam-column elements are used instead of elastic elements to model the wall body, as shown in Fig. 4.4. This facilitates investigating the nonlinearity that is expected to develop in the wall body vertical reinforcement at the MCE level.

The uplift due to rocking is modeled using a bed of zero-length spring elements with a no-tension material model (Concrete01). The displacement of the nonlinear zero-length spring elements at peak strength is defined as the strain at the maximum compressive stress in masonry multiplied by the equivalent height of inelastic deformations as discussed by Yassin et al. (2020).

The ED bars are modeled as truss elements using the Hysteretic-Material material model. The model was defined using three points in the tension and compression stress-strain curves that correspond to: 1) the yield strength of 450 MPa and yield strain of 0.0025; 2) the end of the yield plateau at 450MPa and 0.005 mm/mm; and 3) the ultimate strength of 650 MPa and ultimate strain of 0.085. These values were taken from uniaxial tension testing of the ED bars, except that the ultimate strain was taken as 85% of the test result (0.1 mm/mm) to approximate the effects of low cycle fatigue. PinchX and PinchY values of 0.5 and damage1 and damage2 values of 0.035 and zero were used to capture ED bar damage due to buckling. The length of the truss element is equal to the unbonded length, $L_{un}$, of the ED bars.

The wall body is modeled using one force-based distributed plasticity element for each story, with the fiber section representation having five integration points along each member length. The wall section is discretized into a number of fibers that matches the number of springs at the base to prevent numerical instability. The concrete fibers are modeled using Concrete06, which includes parameters to define strength and stiffness degradation. Values of -0.003 and 0.0008 were assigned to represent the strains at peak compressive and tensile strengths, respectively. The compressive shape factor was taken as 2, the post-peak compressive shape factor as 1, and the parameters for compressive and tensile plastic strain definition were 0.32 and 0.08, respectively. The exponent of the tension stiffening curve and the tensile strength were 4 and 0.1 MPa, respectively. Wall body vertical reinforcement is modeled using a Giuffre-Menegotto-Pinto model (Steel02 in OpenSees). The model was defined using the experimentally measured yield strength of 470 MPa and strain hardening ratio of 1.0%. The initial elastic modulus was 200 GPa and other constants that control the transition from elastic to plastic zone were $R_0$, $CR_1$, and $CR_2$, which were taken as 20, 0.925, and 0.15, respectively.

When modeling buildings with ED-CRMWs, the P-Delta effects from the gravity system were accounted for using a leaning column modeled with elastic beam-column elements. To ensure that the leaning column does not contribute to the stiffness of the wall, a very small rotational spring stiffness is introduced at the end of the leaning column. Only horizontal degrees of freedom for wall nodes and

the corresponding leaning column nodes are constrained to transfer the lateral forces.

### 4.4.2. MODEL VALIDATION

The numerical model developed in the current study was validated against the experimental results of six ED-CRMWs that were tested by Yassin et al. (2021a). These walls were half-scale with the same length (1895 mm), thickness (90 mm) and height (2660 mm), representing two-storey walls. All walls were subjected to an axial load of 200 kN ($6.5\%A_g f_m^{/}$) to represent the floor gravity loads, except that wall W5 had an axial load of 400 kN ($13\%A_g f_m^{/}$) to investigate the effect of higher gravity loads. Table 4.1 presents the complete test matrix with the wall reinforcement details. All walls were tested under quasi-static reversed cyclic loading with an observed rocking response. Each test was terminated when either the wall reached 50% strength degradation, or the maximum stroke of the hydraulic actuator was reached. The test matrix included an unconfined wall (W1), a confined wall with boundary elements and closed stirrups (W2), a confined wall with Priestley plates (W3), a wall with ED close to the wall centerline (W4), a wall with high axial stress level (W5), and finally a wall with no horizontal reinforcement (W6). All these walls were fully grouted and had unbonded axial yielding M10 bars with an unbonded length, $L_{un}$, of 900 mm installed internally across the wall-foundation interface as a source of supplemental ED. The ED bars were located at 250 mm from the wall ends for walls W1, W2, W3, and W5 to protect the bars from

the crushing zone, whereas the ED bars for W4 were located at 140 mm from the wall centerline.

As shown in Fig. 4.5, there is good agreement between the experimental and numerical hysteresis loops for all five walls. The model was able to simulate the experimental results such as the initial stiffness, ultimate strength, stiffness degradation, strength deterioration, and hysteretic loop shape and size at different drift levels. Regarding W2, the sudden strength degradation at 2.4% drift was due to ED bar fracture, and this behavior is captured accurately by the model through the MinMax material available in OpenSees using a fracture strain of 0.04. In addition, the hysteretic shape of W4 compared to W1 is relatively pinched due to the ED bar location, which is also captured by the numerical model. More details about the modeling evaluation are provided by Yassin et al. (2021b).

## 4.5. DESIGN EXAMPLES

In this chapter, the proposed approach was used to design 20 fully grouted ED-CRMWs for buildings with 4, 6 and 8 stories located on a site of high seismicity in the western USA. The site has a seismic design category (SDC) $D_{max}$ with short period $T_s$ and spectral acceleration $S_S$ equal to 0.6 sec and 1.5g, respectively, while the one-second spectral acceleration, $S_1$, is equal to 0.6g as per ASCE/SEI 7-16 (ASCE/SEI 2016). The 20 archetypes address different design parameters such as response modification factor value, gravity load intensity, amount and location of ED, and structure period domain, so as to investigate how each design parameter

influences the collapse risk. The current study adopts the same buildings as in NIST GCR 10-917-8 (2010) in terms of load intensities, floor plans, and story heights, but the wall thickness and masonry compressive strength were kept the same for all buildings with values of 305 mm and 21.5 MPa, respectively. Full details of the slab load intensities and typical floor plans of the example buildings are provided in Appendix A of the GCR 10-917-8 study (NIST 2010).

Table 4.2 shows all the design parameters for the base rocking joints of each of the 20 designed archetypes, including the wall length $L_w$, response modification factor $R$, level of gravity loads, and the ED unbonded length $L_{un}$ and ratio $\kappa$. In addition, the base rotation $\theta_{b,EDy}$ at incipient ED bar yielding and the vertical and horizontal body reinforcement ratios ($\rho_v$ and $\rho_h$) are also listed. No distinct seismic response modification factors are yet provided in North American building codes and design standards for ED-CRMWs. Therefore, the designs were conducted with different values of $R$ (i.e., 5, 7 and 9) as a design parameter, as shown in Table 4.2, so as to evaluate what response modification factors could be suitable for low-rise to mid-rise structures. The evaluation was based on collapse risk assessment through achieving an acceptable collapse margin ratio between the median collapse spectral intensity of a suite of ground motions and the spectral intensity of the MCE as per the FEMA P695 methodology (FEMA 2009). An initial value of $R$ equal to 5 was considered, which is the same value assigned for special reinforced masonry walls in the ASCE-7 (2016). The effect of axial load level in design was also considered with walls having different levels of axial stress, ranging between a

lower bound of 0.41 MPa for $\rho_{min}$ and an upper bound of 1.81 MPa for $\rho_{max}$ based on the tributary area, as shown in Table 4.2. In addition, to consider the effect of ED on the collapse margin ratio, different hysteretic ED ratios, $\kappa$, were used. In this regard, two values of ED ratios (i.e., $\kappa_{min}$ and $\kappa_{max}$) were considered for each archetype, where a lower bound of 0.2 was used for $\kappa_{min}$ to ensure that the system has sufficient damping and an upper bound of 0.9 was used for $\kappa_{max}$ to ensure self-centering considering maximum force developed in ED at ultimate strength, as shown in Table 4.2. Different combinations of $R$, $\rho$, $\kappa$ were used for short period domain walls (i.e., with $T<T_s$), represented by 4-story walls, and long period domain walls (i.e., with $T>T_s$), represented by 8-story walls, where $T_s$ is the boundary between the constant acceleration and constant velocity regions of the design spectrum. All the ED bars were located 250 mm from the archetype ends, except for the 6-story wall 6S-R5-$\rho_{max}$-ED$_{min}$I, where ED bars were placed at the wall centerline to investigate the effect of ED location on the wall performance.

## 4.6. NONLINEAR ANALYSES

Nonlinear static and dynamic analyses were performed on all 20 archetypes to validate the proposed design approach.

### 4.6.1. PUSHOVER ANALYSIS

The nonlinear static pushover analyses were performed using the code-prescribed first-mode lateral force distributions (ASCE/SEI 2017) used to design the base rocking joint. The pushover analysis was used to compute the overstrength factor

$\Omega$, and the period-based ductility, $\mu_T$, for each ED-CRMW archetype, with the results shown in Table 4.3. The period-based ductility, $\mu_T$, is the ratio between the lateral displacement at 20% strength degradation, $\delta_u$, and the effective yield displacement, $\delta_{y,eff}$, as per the FEMA P695 methodology (FEMA 2009). The stress in the outermost wall body vertical bonded reinforcement was verified not to exceed the yield strength during the pushover analysis for all archetypes. The pushover curves for all 20 ED-CRMW archetypes are shown in Fig. 4.6. For the 4-story and 8-story archetypes, increasing the response modification factor, $R$, reduces the decompression load and generally leads to a larger period-based ductility, $\mu_T$. Conversely, increasing the axial load level generally reduces the period-based ductility, $\mu_T$, ultimate displacement, and the system post-yield stiffness. Finally, as the ED ratio, $\kappa$, increases, both the pre-yield and post-yield stiffness increase. The decompression load and yield displacement are the same since the same unbonded length is used, but the ultimate displacement is reduced, leading to a reduction of the period-based ductility, $\mu_T$. For the 6-story archetypes, placing the ED at the wall centerline reduces the strain demand on the ED bar, delaying the yielding stage as seen in Fig. 4.6c. Moreover, the compression demand on the crushing toe also increases as double the area of ED is required at the wall centerline to achieve the same strength. This leads to a reduction of the period-based ductility, $\mu_T$, as seen in Fig. 4.6c. The post-yield stiffness depends significantly on the location of ED, $d_{ED}$, as presented in Eq. 4.10, hence reducing $d_{ED}$ reduces $\gamma_2$, leading to a negative net slope $\gamma$ representing the post-yield

rotational stiffness. The same behavior was experimentally observed with wall W4 reported by Yassin et. al (2021a). Hence, it is recommended to place the ED near the wall ends rather than the wall centerline.

### 4.6.2. DYNAMIC ANALYSIS

Nonlinear dynamic analyses were performed on the 20 ED-CRMWs using the set of 44 far-field ground motion records (i.e., 22 pairs of horizontal components) specified for collapse assessment of structures in FEMA P695 (FEMA 2009). The ground motions were normalized by their peak ground velocity to reduce any inherent variability before scaling, then their median was scaled to match the MCE elastic spectrum at the code-based period, $T$, for the 4-story, 6-story and 8-story archetypes. The resulting scaling factors were 2.00, 2.49 and 2.50 for the 4-story, 6-story and 8-story archetypes, respectively. The code-based period $T$ was calculated for all archetypes using $C_u T_a$, but subject to the lower bound value of 0.25 sec, as recommended in FEMA P695 (FEMA 2009), and a modal analysis was conducted to calculate the values of $T_1$. The seismic base shear coefficient, $V/W_s$ (where $V$ is the base shear and $W_s$ is the seismic weight), code-based period $T$, and modal analysis period $T_1$ are shown in Table 4.3. In the current study, initial stiffness-proportional Rayleigh damping was used with a damping ratio of 5% in the first and third modes, with no damping associated with the zero-length spring elements.

In this study, collapse was defined as the point when the wall first reaches one of two conditions: (1) masonry crushing, considered to occur when 15% of the cross section reached a crushing strain of 0.006; (2) an inter-story drift of 3.0%.

## 4.7. DYNAMIC ANALYSIS RESULTS

The results of the nonlinear response time history analyses for one 4-story wall (4S-R5-$\rho_{max}$-$ED_{max}$) and one 8-story wall (8S-R5-$\rho_{max}$-$ED_{max}$) are presented here as representative examples of the design approach validation. The median values of the peak response indicators from the 44 ground motions are depicted in Fig. 4.7 and 8 for both walls and discussed below.

Fig. 4.7 presents the median response at the DE level and MCE level and the closed-form equation at MCE level for the story shear, overturning moment envelopes and inter-story drifts. As shown in Fig. 4.7 a and c for 4-and 8-story walls, respectively, the base shear at the MCE level is less than the nominal shear capacity, which conforms to the design objective of no diagonal shear failure at the MCE level. While the closed-form equation accurately estimates the MCE-level base shear for the four-story wall, it underestimates that shear for the eight-story wall by 20%. As shown in Fig. 4.7 b and d, the overturning moment envelope at the MCE level is reduced compared to the closed-form equation. This is because of vertical body reinforcement yielding, as permitted in design and confirmed by the body vertical reinforcement values as will be discussed later. As shown in Fig. 4.7 e and f for the 4 and 8-story walls, respectively, the drifts at DE are much less than

the two-thirds of maximum drift of 3%, and the drifts at MCE are less than the maximum allowed drift of 3%. Also, as shown in Fig. 4.7 e and f, Eq. 4.5 accurately estimates the design-level drifts with an error of 10% and 13% for the 4- and 8-story walls, respectively.

For each ground motion, Fig. 4.8 presents the maximum stress in the outermost vertical reinforcement bar and in the outermost masonry fibre at the first floor of the 4-story archetype, and at the second floor of the 8-story archetype (corresponding to maximum demand overturning envelope moment), along with the median response at the DE and MCE levels. As shown in Fig. 4.8 a and b, the median stress in the outermost vertical reinforcement bar for the 4-story and the 8-story archetypes at DE level is well within the elastic range. This conforms to the performance criterion, where the ED-CRMWs were designed to have no damage due to bar yielding at the design earthquake. In addition, the median stress in the outermost vertical reinforcement bar in the 4-story archetype is far from yielding at the MCE level, while the 8-story archetype median stress at the MCE level is near yielding, with many ground motions causing yield. This is mainly attributed to the effect of higher modes being more pronounced in long-period structures (Yassin et al. 2020; Rutenberg 2013).

To check the condition of the masonry, similarly, the outermost masonry fibre stress is traced at different intensities. Fig. 4.8 c and d show that the 4-story and the 8-story archetype median masonry stresses at the DE level are still in the elastic zone of the masonry stress-strain curve, considered here as less than 0.45

$f_m^{'}$ (TMS 2016). This confirms that the design procedure used was effective in avoiding damage to the wall body at the DE level. At the MCE level, the median masonry stress is still in the elastic zone for the 4-story archetype due to the smaller effect of higher modes, while the 8-story archetype is 13% more than the elastic limit, with many ground motions far exceeding that limit.

To check the self-centering performance, the residual drift at the end of each ground motion is shown in Fig. 4.8 e and f. The residual roof drifts for the 4- and 8-story archetypes are less than 0.02% under the DE level ground motions and less than 0.045% under the MCE level ground motions. These residual roof drifts are much less than an acceptable limit of 0.2% residual drift to avoid structural repairs as per FEMA P-58 (2018).

## 4.8. SYSTEM COLLAPSE RISK EVALUATION

This section evaluates the influence of certain design parameters on the collapse performance. The multiple stripes analysis (MSA) method (Jalayer 2003) was used to reduce the number of analyses required compared to the full incremental dynamic analysis (IDA) (Vamvatsikos and Cornell 2002). The MSA allows the fragility parameters to be computed from the observed data by counting the number of collapses at each scaled intensity measure (Baker 2015). In this regard, ground motion records were scaled from 50% to 400% of the MCE spectral intensity with an increment of 50%, leading to 8 stripes in total. The median collapse spectral intensity, $S_{CT}$, was determined for each archetype assuming a lognormal

distribution using the maximum likelihood method (Baker 2015). As per the FEMA P695 methodology (FEMA 2009), the collapse margin ratio (CMR) is the ratio between the median collapse spectral intensity, $S_{CT}$, and the MCE spectral acceleration, $S_{MT}$, at the fundamental code-based period, $T$, as shown in Eq. 4.16. Table 4.4 summarizes all values of CMR calculated from the dynamic analyses.

$$CMR = \frac{S_{CT}}{S_{MT}} \tag{4.16}$$

The system is then assessed through the adjusted collapse margin ratio (ACMR), computed as the product of the collapse margin ratio (CMR) and the spectral shape factor (SSF) as per the FEMA P695 methodology (FEMA 2009). The spectral shape factor (SSF) is defined based on the period-based ductility, $\mu_T$, obtained from the pushover analyses, and the fundamental code-based period, $T$. Next, the obtained values of the ACMR are compared with the acceptable values given in FEMA P695 (FEMA 2009). Each design archetype is considered as an individual building as per Appendix F of FEMA P695 (FEMA 2009), so the acceptable value ($ACMR_{10\%}$) for each building is based on a probability of collapse of 10% or less. The acceptable value of the adjusted collapse margin ratio $ACMR_{10\%}$ is determined from the total system uncertainty, $\beta_{TOT}$, calculated from Eq. (4.17).

$$\beta_{TOT} = \sqrt{\beta_{RTR}^2 + \beta_{DR}^2 + \beta_{TD}^2 + \beta_{MDL}^2} \tag{4.17}$$

where $\beta_{RTR}$ is the record-to-record uncertainty of the collapse data arising from variations in frequency content of the different ground motions, and where $\beta_{DR}$, $\beta_{TD}$

and $\beta_{MDL}$ are the additional uncertainty attributed to the robustness of the design requirements, robustness of the test data used to define the system, and the robustness of the numerical models used in predicting the system collapse behavior, respectively. A value of 0.4 was used for $\beta_{RTR}$ because the period-based ductility, $\mu_T$, for all ED-CRMW archetypes is greater than 3.0 (FEMA 2009). The factors $\beta_{DR}$ and $\beta_{MDL}$ were categorized as B-good with a value of 0.2, while $\beta_{TD}$ was categorized as C-fair with a value of 0.35 as this is a newly proposed system that has a very limited number of tests performed to date. Based on the above, the $\beta_{TOT}$ was calculated as 0.602. Hence, the acceptable value of the adjusted collapse margin ratio $ACMR_{10\%}$, is taken as 2.17 (FEMA 2009).

### 4.8.1. INFLUENCE OF DESIGN PARAMETERS ON COLLAPSE RISK

The results of the performance evaluation are shown in Table 4.4, where the ACMR values for all archetypes are compared with the acceptable $ACMR_{10\%}$ for the 20 ED-CRMW archetypes. As can be seen from Table 4.4, the response modification factor, *R*, amount of ED, $\kappa$, and the level of axial compression, $\rho_P$ , influenced the collapse margin ratio of ED-CRMWs.

For the nine four-story archetypes (representing short-period structures), Table 4.4 shows that the calculated ACMR values satisfy the acceptable ACMR limits whether using an *R* factor of 5, 7 or 9. Conversely, for the nine eight-story archetypes (representing long-period structures), the acceptable ACMR limit is satisfied when using an *R* factor of 5 or 7, while a high axial stress leads to the

archetype failing if *R* of 9 is adopted. In general, increasing the response modification factor, *R*, while keeping the same ED ratio, $\kappa$, and axial compression load, $\rho_P$, reduces the ACMR and increases the probability of collapse. As shown in Table 4.4, the ACMR is reduced by 22% and 30% on average when *R* is increased from 5 to 7 and 9, respectively. Similarly, a higher level of axial compression, $\rho_P$, with the same design forces (i.e., using the same *R* value) decreases the ACMR in all of the considered cases. This is mainly because increasing the axial compression leads to an increased strain demand on the crushing toes. For example, comparing 8S-7R-$\rho_{max}$-$ED_{max}$ and 8S-7R-$\rho_{min}$-$ED_{max}$ archetypes, the ACMR is reduced by 12.5% when $\rho_P$ increases from 0.87 to 1.65 MPa. Conversely, increasing the hysteretic ED ratio, $\kappa$, while maintaining the same design forces (i.e., using the same *R* value), increases the ACMR in all of the considered cases. This is mainly because increasing the ED reduces the displacement demand on self-centering systems (Seo and Sause 2005; Zhang et al. 2018). For instance, comparing 8S-R5-$\rho_{max}$-$ED_{min}$ and 8S-R5-$\rho_{max}$-$ED_{max}$ archetypes, the ACMR increased by 9.5% when $\kappa$ increased from 0.25 to 0.51. Finally, the ACMR for 6S-R5-$\rho_{max}$-$ED_{min}$ and 6S-R5-$\rho_{max}$-$ED_{min}$I show that the location of ED affects the collapse margin ratio, as placing the ED near the wall centerline reduced the ACMR by 8%. This is mainly attributed to the increased demand on the crushing toes when double the amount of ED was required to have the same wall strength.

## 4.9. CONCLUSIONS

This chapter presented a detailed seismic design approach for a newly proposed system, namely energy dissipation-controlled rocking masonry walls (ED-CRMWs). Afterwards, a multi-spring numerical model using OpenSees was validated against recent experimental tests. Using this model, nonlinear pushover and dynamic analyses were performed to evaluate the seismic design and performance of ED-CRMWs. This study used the FEMA P695 (FEMA 2009) methodology to evaluate the collapse risk of 20 archetype ED-CRMWs with different seismic response modification factors, amounts of energy dissipation (ED), and levels of axial stress.

The intended performance was confirmed, in that all nonlinearity was from the base rocking joint at the design earthquake (DE) level, leading to an essentially damage-free system with no yielding of vertical body reinforcement or masonry exceeding the elastic limit. At the maximum considered earthquake (MCE) level and above, another source of nonlinearity was allowed in the form of vertical body reinforcement yielding. The design criteria were confirmed to mitigate the effects of the higher modes on overturning moments by allowing limited vertical reinforcement yielding, which significantly reduced the overturning moment demands. The self-centering capability of the walls was also confirmed with residual roof drifts for the 4- and 8-story archetypes that averaged less than 0.02%

under the DE-level ground motions and less than 0.045% under the MCE-level ground motions.

Considering the seismic evaluation of ED-CRMW archetypes with 4 and 8 stories, an *R* value of 7 fully met the acceptance criteria of the FEMA P695 (FEMA 2009) methodology for the considered archetypes. As such, comparing this system with special reinforced masonry walls, ED-CRMWs can allow a higher value of *R* and add the benefits of self-centering capability and limited damage, even without the need for post-tensioning (PT). In addition, the influence of design parameters such as the response modification factor (*R* of 5, 7 and 9), the level of axial stress, and the ED amount and location were investigated for the 20 considered ED-CRMW archetypes. Increasing the value of the response modification factor reduced the ACMR, indicating a higher probability of collapse. Similarly, increasing the axial stress level reduced the ACMR, while increasing the amount of ED increased the ACMR. The collapse analysis also indicated that it is preferable to place the ED at the wall ends, rather than at the wall centerline, as this reduces the compression demand on the wall toes and increases the post-yield stiffness for the system.

While these results are promising, further research studies are still needed to experimentally investigate the dynamic behavior of the ED-CRMWs under the proposed design approach, and to increase the number of tested walls in order to reduce the uncertainty level.

## 4.10. ACKNOWLEDGMENTS

The financial support for this project was provided through the Canadian Concrete Masonry Producers Association (CCMPA), the Canada Masonry Design Centre (CMDC), the Natural Sciences and Engineering Research Council (NSERC) and the Ontario Centres of Excellence (OCE).

## 4.11. REFERENCES

ACI (American Concrete Institute). (2009). "Requirements for Design of a Special Unbonded Post-Tensioned Precast Shear Wall Satisfying ACI ITG-5.1 & Commentary." ACI ITG-5.2-09, Farmington Hills, MI.

ASCE/SEI (Structural Engineering Institute). (2016). "Minimum design loads for buildings and other structures." ASCE/SEI 7-16, Reston, VA.

Baker J. (2015). "Efficient analytical fragility function fitting using dynamic structural analysis." Earthquake Spectra, 31(1), 579–599

Buddika, H., and Wijeyewickrema, A. (2016). "Seismic Performance Evaluation of Posttensioned Hybrid Precast Wall-Frame Buildings and Comparison with Shear Wall-Frame Buildings." J. Struct. Eng., 142(6): 04016021

FEMA. (2009). "Quantification of building seismic performance factors." FEMA P695, Washington, DC.

FEMA. (2018). "Seismic performance assessment of buildings" FEMA-P58, Washington, DC.

Hassanli, R., ElGawady, M., and Mills, J. (2016). "Experimental investigation of in-plane cyclic response of unbonded-posttensioned masonry walls." Journal of Structural Engineering, 142(5), 04015171-1-15.

Jalayer, F. (2003). "Direct probabilistic seismic analysis: implementing non-linear dynamic assessments." PhD Thesis, Department of Civil and Environmental Engineering, Stanford University.

Kalliontzis, D., and Schultz, A. E. (2017). "Improved estimation of the reverse-cyclic behavior of fully-grouted masonry shear walls with unbonded post-tensioning." Engineering Structures, 145, 83–96.

Kalliontzis, D., Sritharan, S., and Schultz, A. E. (2019). "Improving Performance of Unbonded Post-Tensioned Masonry Walls with the Use of Rubber Interface" 13th North American Masonry Conference, June 16-19, Salt Lake City, USA

Kalliontzis, D., and Sritharan, S. (2020). "Dynamic response and impact energy loss in controlled rocking members." Earthquake Engineering & Structural Dynamics, 49(4), 319-338.

Kurama, Y., Pessiki, S., Sause, R., and Lu, L.W. (1999). "Seismic behavior and design of unbonded post-tensioned precast concrete walls." PCI Journal, 44(3), 72-89.

Kurama, Y. (2005). "Seismic Design of Partially Post-Tensioned Precast Concrete

Walls." PCI Journal, 50(4), 100–125.

Laursen, P. T. and Ingham, J. M. (2004). "Structural testing of large-scale posttensioned concrete masonry walls." Journal of Structural Engineering, 130(10), 1497-1505.

McKenna, F., Fenves, G. L., and Scott, M. H. (2000). "Open system for earthquake engineering simulation." University of California, Berkeley, CA.

NIST (National Institute of Standards and Technology). (2010). "Evaluation of the FEMA P695 methodology for quantification of building seismic performance factors." NIST GCR 10-917-8, Gaithersburg, MD.

Panagiotou, M., and Restrepo, J. (2009). "Dual-plastic hinge design concept for reducing higher-mode effects on high-rise cantilever wall buildings." Earthquake Engineering & Structural Dynamics, 38(12), 1359-1380.

Pennucci, D., Calvi, G. M., and Sullivan, T. J. (2009). "Displacement-based design of precast walls with additional dampers." Journal of Earthquake Engineering, 13(1), 40-65.

Priestley, M. J. N., Sritharan, S., Conley, J. R., and Pampanin, S. (1999). "Preliminary results and conclusions from the PRESSS five-story precast concrete test building." PCI Journal, 44(6), 42-67.

Rosenboom, O. A., and Kowalsky, M. J. (2004). "Reversed in-plane cyclic behavior of posttensioned clay brick masonry walls." J. Struct. Eng.,

10.1061/(ASCE)0733-9445(2004)130:5(787), 787–798.

Rutenberg, A. (2011). "Seismic shear forces on RC walls: review and bibliography." Bulletin of Earthquake Engineering, 11(5),1726‑1751.

Seo, C., Sause, R. (2005). "Ductility demands on self-centering systems under earthquake loading." ACI Journal, 102(2), 275–285.

Smith, B., Kurama, Y., and McGinnis, M. (2012). "Hybrid Precast Wall Systems for Seismic Regions." Structural Engineering Research Report #NDSE-2012-01, University of Notre Dame, IN, Notre Dame, IN.

TMS (The Masonry Society). (2016). "Building Code Requirements and Specification for Masonry Structures." TMS 402/602-16, Longmont, CO.

Vamvatsikos, D., and Cornell, A. (2002). "Incremental dynamic analysis." Earthquake Eng. Struct. Dyn., 31(3), 491–514.

Wiebe, L., and Christopoulos, C. (2015a). "Performance-Based Seismic Design of Controlled Rocking Steel Braced Frames. I: Methodological Framework and Design of Base Rocking Joint." J. Struct. Eng., 141(9), 04014226-1-11.

Wiebe, L., and Christopoulos, C. (2015b). "A cantilever beam analogy for quantifying higher mode effects in multistorey buildings." Earthquake Engineering & Structural Dynamics, 44(11), 1697-1716.

Wight, G. D., Ingham, J. M., and Kowalsky, M. J. (2006). "Shake table Testing of Rectangular Post-Tensioned Concrete Masonry Walls." PCI Journal, 103(4),

587-595.

Yassin, A., Ezzeldin, M., Steele, T., and Wiebe, L. (2020). "Seismic collapse risk assessment of post-tensioned controlled rocking masonry walls." J. Struct. Eng., 146(5), 04020060-1-16.

Yassin, A., Ezzeldin, M., and Wiebe, L. (2021a). "Large-Scale Testing of Controlled Rocking Masonry Shear Walls without Post-Tensioning." In progress

Yassin, A., Ezzeldin, M., and Wiebe, L. (2021b). "Numerical Modelling of the Seismic Performance of Controlled Rocking Masonry Walls without Post-Tensioning" 17th WCEE, Sept 27-Oct 2, Sendai, Japan.

Yassin, A. (2021). "Development of controlled rocking reinforced masonry walls" PhD Thesis, McMaster University.

Zhang, C., Steele, T., and Wiebe, L. (2018). "Design-level estimation of seismic displacements for self-centering SDOF systems on stiff soil" Engineering Structures, 177, 431–443.

## 4.12. TABLES

**Table 4.1.** ED-CRMW Dimensions and Properties for Model Validation

| Specimen | Wall type | Wall dimension LxH (mm) | Wall Body bonded vertical reinforcement | Axial yielding unbonded ED bars | Shear reinforcement | Axial stress (MPa) |
|---|---|---|---|---|---|---|
| W1 | Unconfined | 1895 x 2660 | 6D7 | 1M10 @710 mm from C.L. | D4 every other course | 1.17 |
| W2 | Boundary elements | 1895 x 2660 | 4D7@Web, 8D7 @ Ends | 1M10 @710 mm from C.L. | D4 every other course | 1.17 |
| W3 | Priestley plates | 1895 x 2660 | 6D7 | 1M10 @710 mm from C.L. | D4 every other course | 1.17 |
| W4 | Inner ED | 1895 x 2660 | 6D7 | 1M10 @140 mm from C.L. | D4 every other course | 1.17 |
| W5 | High axial stress | 1895 x 2660 | 6D7 | 1M10 @710 mm from C.L. | D4 every other course | 2.34 |
| W6 | No Hz RFT | 1895 x 2660 | 6D7 | 1M10 @710 mm from C.L. | none | 1.17 |

**Table 4.2.** Design parameters, dimensions, and reinforcement details of ED-CRMW archetypes

| Archetype ID | Length (mm) | $R$ | Gravity loads $\rho_P$ (MPa) | ED ratio $\kappa$ | ED amount per side | $L_{un}$ (mm) | $\theta_{b,EDy}$ (%) | $\rho_v$ (%) | Horizontal RFT. (mm) | $\rho_h$ (%) |
|---|---|---|---|---|---|---|---|---|---|---|
| 4S-R5-$\rho_{max}$-$ED_{max}$ | 9750 | 5 | 0.70 | 0.54 | 1#11 | 3000 | 0.08 | 0.103 | #5@600 | 0.109 |
| 4S-R5-$\rho_{max}$-$ED_{min}$ | 9750 | 5 | 0.70 | 0.25 | 1#8 | 3000 | 0.08 | 0.103 | #5@800 | 0.082 |
| 4S-R5-$\rho_{min}$-$ED_{max}$ | 9750 | 5 | 0.42 | 0.90 | 2#8 | 3600 | 0.09 | 0.103 | #5@800 | 0.082 |
| 4S-R7-$\rho_{max}$-$ED_{max}$ | 7500 | 7 | 0.81 | 0.60 | 1#11 | 2100 | 0.07 | 0.146 | #5@400 | 0.164 |
| 4S-R7-$\rho_{max}$-$ED_{min}$ | 7500 | 7 | 0.81 | 0.21 | 1#7 | 2100 | 0.07 | 0.146 | #5@600 | 0.109 |
| 4S-R7-$\rho_{min}$-$ED_{max}$ | 8500 | 7 | 0.44 | 0.80 | 1#10 | 3300 | 0.10 | 0.128 | #5@600 | 0.109 |
| 4S-R9-$\rho_{max}$-$ED_{max}$ | 6500 | 9 | 0.90 | 0.61 | 1#11 | 2100 | 0.08 | 0.200 | #5@400 | 0.164 |
| 4S-R9-$\rho_{max}$-$ED_{min}$ | 6500 | 9 | 0.90 | 0.23 | 1#7 | 2100 | 0.08 | 0.200 | #5@600 | 0.109 |
| 4S-R9-$\rho_{min}$-$ED_{max}$ | 7500 | 9 | 0.41 | 0.90 | 1#10 | 3000 | 0.10 | 0.173 | #5@600 | 0.109 |
| 8S-R5-$\rho_{max}$-$ED_{max}$ | 9750 | 5 | 1.42 | 0.51 | 3#9 | 2100 | 0.06 | 0.191 | #5@800 | 0.082 |
| 8S-R5-$\rho_{max}$-$ED_{min}$ | 9750 | 5 | 1.42 | 0.25 | 2#8 | 2100 | 0.06 | 0.144 | #5@800 | 0.082 |
| 8S-R5-$\rho_{min}$-$ED_{max}$ | 9750 | 5 | 0.84 | 0.81 | 3#9 | 2100 | 0.06 | 0.191 | #5@800 | 0.082 |
| 8S-R7-$\rho_{max}$-$ED_{max}$ | 7500 | 7 | 1.65 | 0.48 | 2#10 | 2100 | 0.08 | 0.309 | #5@600 | 0.109 |
| 8S-R7-$\rho_{max}$-$ED_{min}$ | 7500 | 7 | 1.65 | 0.22 | 1#10 | 2100 | 0.08 | 0.221 | #5@600 | 0.109 |
| 8S-R7-$\rho_{min}$-$ED_{max}$ | 8500 | 7 | 0.87 | 0.61 | 2#9 | 2100 | 0.07 | 0.272 | #5@600 | 0.109 |
| 8S-R9-$\rho_{max}$-$ED_{max}$ | 6500 | 9 | 1.81 | 0.51 | 2#10 | 2100 | 0.10 | 0.356 | #5@600 | 0.109 |
| 8S-R9-$\rho_{max}$-$ED_{min}$ | 6500 | 9 | 1.81 | 0.20 | 1#9 | 2100 | 0.10 | 0.255 | #5@600 | 0.109 |
| 8S-R9-$\rho_{min}$-$ED_{max}$ | 7500 | 9 | 0.82 | 0.74 | 2#9 | 2100 | 0.08 | 0.309 | #5@600 | 0.109 |
| 6S-R5-$\rho_{max}$-$ED_{min}$ | 9750 | 5 | 1.08 | 0.28 | 1#10 | 2100 | 0.06 | 0.090 | #5@800 | 0.082 |
| 6S-R5-$\rho_{max}$-$ED_{min}$I* | 9750 | 5 | 1.08 | 0.28 | 2#10* | 2100 | 0.13 | 0.090 | #5@800 | 0.082 |

* ED located at wall centerline.

**Table 4.3.** Summary of ED-CRMW archetype parameters

| Archetype ID | Number of stories | Period domain | *T (s)* | $T_1$ (s) | $V/W_s$ | Overstrength ($\Omega$) | Period-based ductility ($\mu_T$) |
|---|---|---|---|---|---|---|---|
| 4S-R5-$\rho_{max}$-$ED_{max}$ | 4 | Short period domain $T < Ts$ | 0.45 | 0.14 | 0.20 | 1.33 | 23.4 |
| 4S-R5-$\rho_{max}$-$ED_{min}$ | 4 | | 0.45 | 0.14 | 0.20 | 1.30 | 29.2 |
| 4S-R5-$\rho_{min}$-$ED_{max}$ | 4 | | 0.45 | 0.13 | 0.20 | 1.37 | 32.7 |
| 4S-R7-$\rho_{max}$-$ED_{max}$ | 4 | | 0.45 | 0.20 | 0.14 | 1.33 | 35.2 |
| 4S-R7-$\rho_{max}$-$ED_{min}$ | 4 | | 0.45 | 0.20 | 0.14 | 1.29 | 47.9 |
| 4S-R7-$\rho_{min}$-$ED_{max}$ | 4 | | 0.45 | 0.16 | 0.14 | 1.39 | 61.5 |
| 4S-R9-$\rho_{max}$-$ED_{max}$ | 4 | | 0.45 | 0.24 | 0.11 | 1.34 | 43.3 |
| 4S-R9-$\rho_{max}$-$ED_{min}$ | 4 | | 0.45 | 0.24 | 0.11 | 1.30 | 58.4 |
| 4S-R9-$\rho_{min}$-$ED_{max}$ | 4 | | 0.45 | 0.20 | 0.11 | 1.41 | 52.2 |
| 8S-R5-$\rho_{max}$-$ED_{max}$ | 8 | Long period domain $T > Ts$ | 0.75 | 0.46 | 0.16 | 1.27 | 9.6 |
| 8S-R5-$\rho_{max}$-$ED_{min}$ | 8 | | 0.75 | 0.46 | 0.16 | 1.28 | 12.2 |
| 8S-R5-$\rho_{min}$-$ED_{max}$ | 8 | | 0.75 | 0.45 | 0.16 | 1.30 | 21.2 |
| 8S-R7-$\rho_{max}$-$ED_{max}$ | 8 | | 0.75 | 0.68 | 0.11 | 1.26 | 16.8 |
| 8S-R7-$\rho_{max}$-$ED_{min}$ | 8 | | 0.75 | 0.68 | 0.11 | 1.27 | 19.4 |
| 8S-R7-$\rho_{min}$-$ED_{max}$ | 8 | | 0.75 | 0.55 | 0.11 | 1.27 | 32.1 |
| 8S-R9-$\rho_{max}$-$ED_{max}$ | 8 | | 0.75 | 0.84 | 0.08 | 1.25 | 21.8 |
| 8S-R9-$\rho_{max}$-$ED_{min}$ | 8 | | 0.75 | 0.84 | 0.08 | 1.28 | 23.3 |
| 8S-R9-$\rho_{min}$-$ED_{max}$ | 8 | | 0.75 | 0.69 | 0.08 | 1.27 | 45.5 |
| 6S-R5-$\rho_{max}$-$ED_{min}$ | 6 | $T = Ts$ | 0.60 | 0.27 | 0.20 | 1.29 | 18.0 |
| 6S-R5-$\rho_{max}$-$ED_{min}$I | 6 | | 0.60 | 0.27 | 0.20 | 1.24 | 13.2 |

**Table 4.4.** Nonlinear dynamic analysis results and collapse capacity evaluation.

| Archetype ID | $S_{MT}$ (g) | $S_{CT}$ (g) | Period domain | CMR | *SSF* | ACMR | Acceptance check | |
|---|---|---|---|---|---|---|---|---|
| | | | | | | | $ACMR_{10\%}$ | Pass/Fail |
| 4S-R5-$\rho_{max}$-$ED_{max}$ | 1.50 | 4.37 | Short period domain $T < Ts$ | 2.91 | 1.33 | 3.87 | 2.17 | Pass |
| 4S-R5-$\rho_{max}$-$ED_{min}$ | 1.50 | 4.07 | | 2.71 | 1.33 | 3.60 | 2.17 | Pass |
| 4S-R5-$\rho_{min}$-$ED_{max}$ | 1.50 | 4.52 | | 3.01 | 1.33 | 4.00 | 2.17 | Pass |
| 4S-R7-$\rho_{max}$-$ED_{max}$ | 1.50 | 3.41 | | 2.27 | 1.33 | 3.02 | 2.17 | Pass |
| 4S-R7-$\rho_{max}$-$ED_{min}$ | 1.50 | 3.26 | | 2.17 | 1.33 | 2.89 | 2.17 | Pass |
| 4S-R7-$\rho_{min}$-$ED_{max}$ | 1.50 | 3.75 | | 2.50 | 1.33 | 3.33 | 2.17 | Pass |
| 4S-R9-$\rho_{max}$-$ED_{max}$ | 1.50 | 3.06 | | 2.04 | 1.33 | 2.71 | 2.17 | Pass |
| 4S-R9-$\rho_{max}$-$ED_{min}$ | 1.50 | 2.94 | | 1.96 | 1.33 | 2.61 | 2.17 | Pass |
| 4S-R9-$\rho_{min}$-$ED_{max}$ | 1.50 | 3.29 | | 2.19 | 1.33 | 2.91 | 2.17 | Pass |
| 8S-R5-$\rho_{max}$-$ED_{max}$ | 1.20 | 2.54 | | 2.12 | 1.39 | 2.95 | 2.17 | Pass |
| 8S-R5-$\rho_{max}$-$ED_{min}$ | 1.20 | 2.33 | | 1.94 | 1.39 | 2.70 | 2.17 | Pass |
| 8S-R5-$\rho_{min}$-$ED_{max}$ | 1.20 | 2.63 | | 2.19 | 1.39 | 3.04 | 2.17 | Pass |
| 8S-R7-$\rho_{max}$-$ED_{max}$ | 1.20 | 1.97 | Long period domain $T > Ts$ | 1.64 | 1.39 | 2.28 | 2.17 | Pass |
| 8S-R7-$\rho_{max}$-$ED_{min}$ | 1.20 | 1.93 | | 1.61 | 1.39 | 2.23 | 2.17 | Pass |
| 8S-R7-$\rho_{min}$-$ED_{max}$ | 1.20 | 2.22 | | 1.85 | 1.39 | 2.57 | 2.17 | Pass |
| 8S-R9-$\rho_{max}$-$ED_{max}$ | 1.20 | 1.89 | | 1.57 | 1.39 | 2.17 | 2.17 | **Fail** |
| 8S-R9-$\rho_{max}$-$ED_{min}$ | 1.20 | 1.72 | | 1.43 | 1.39 | 1.98 | 2.17 | **Fail** |
| 8S-R9-$\rho_{min}$-$ED_{max}$ | 1.20 | 1.99 | | 1.66 | 1.39 | 2.30 | 2.17 | Pass |
| 6S-R5-$\rho_{max}$-$ED_{min}$ | 1.50 | 3.78 | $T = Ts$ | 2.52 | 1.36 | 3.42 | 2.17 | Pass |
| 6S-R5-$\rho_{max}$-$ED_{min}$I | 1.50 | 3.52 | | 2.35 | 1.36 | 3.20 | 2.17 | Pass |

## 4.13. FIGURES

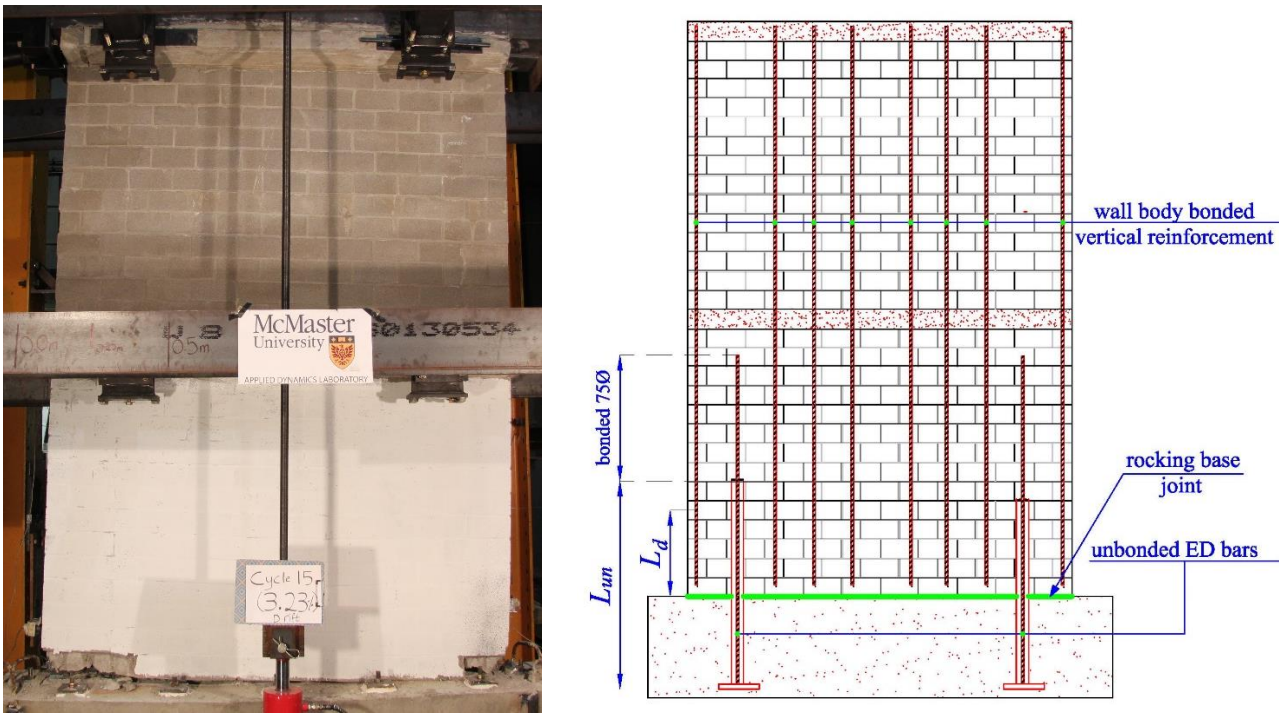


**Fig. 4.1.** ED-CRMW a) at 3.25% drift with limited damage, b) system curtailment.

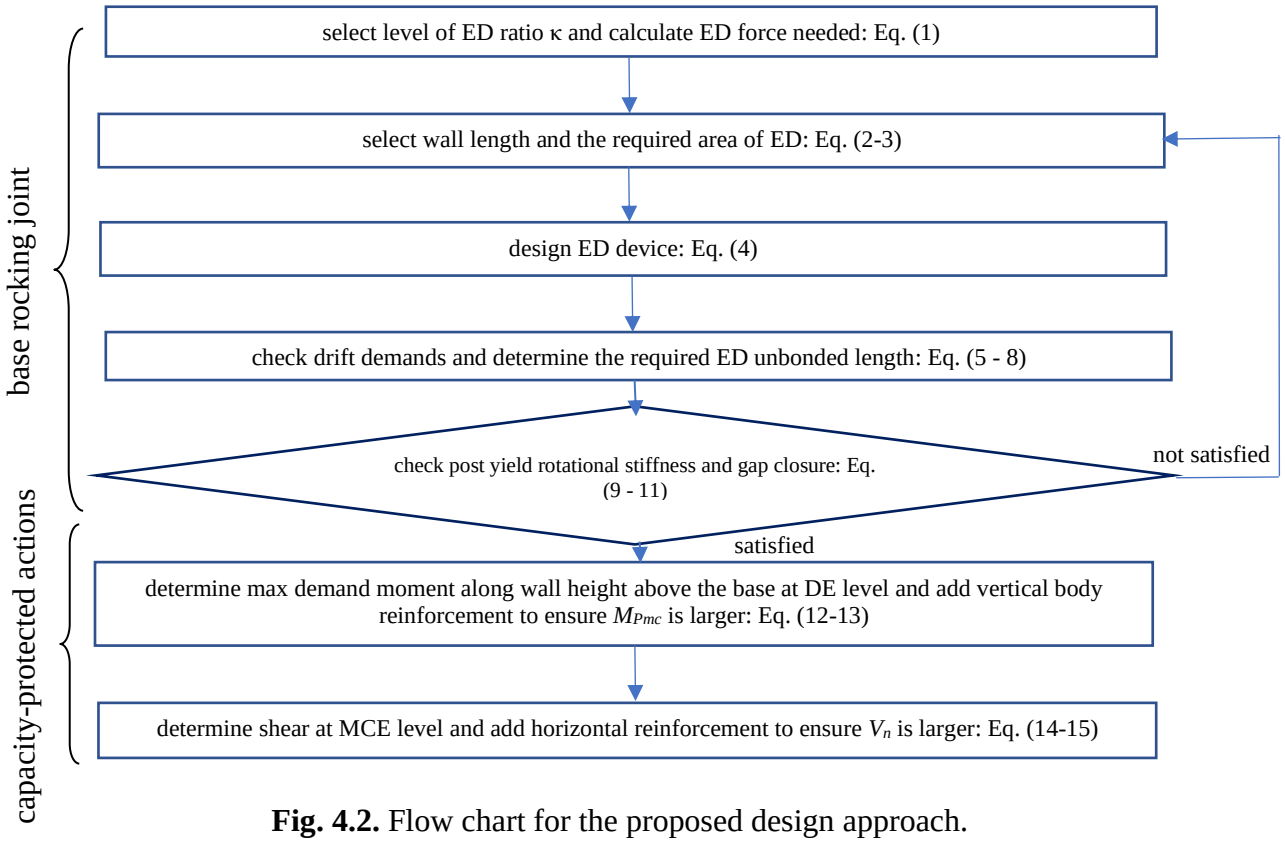


**Fig. 4.2.** Flow chart for the proposed design approach.

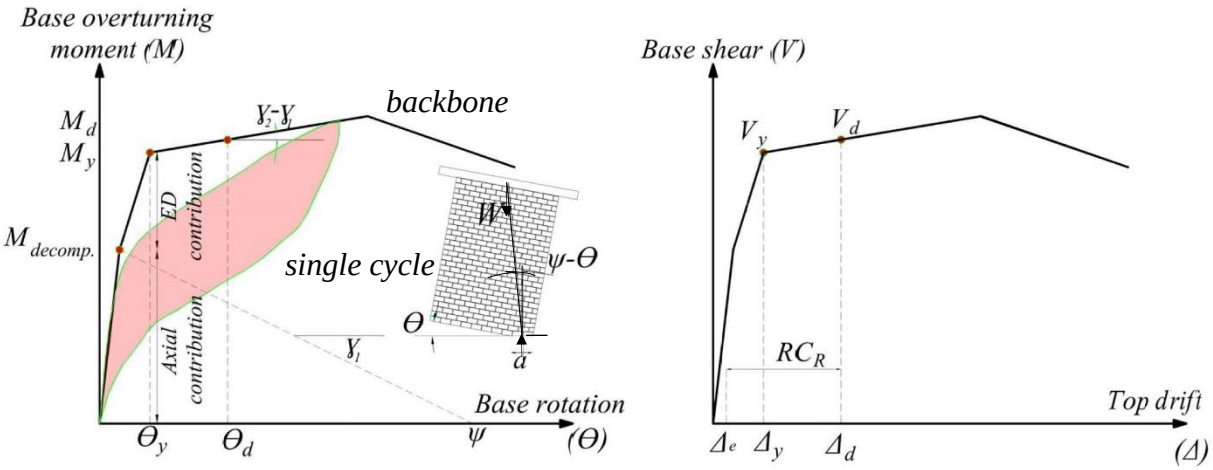


**Fig. 4.3.** System limit states.

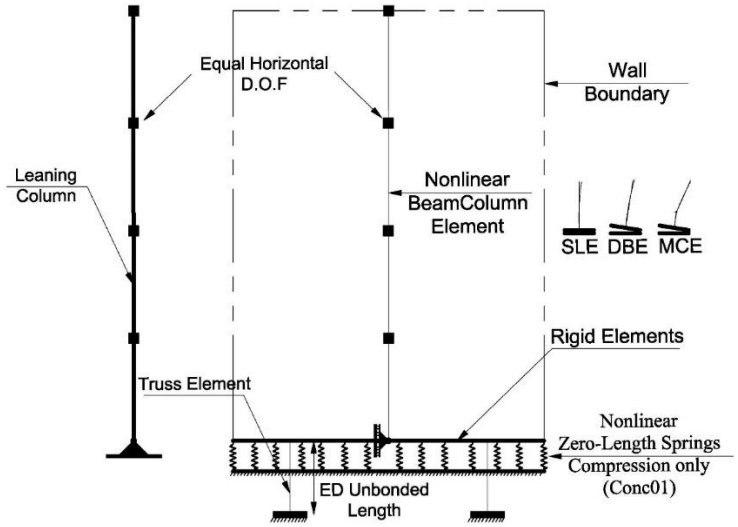


**Fig. 4.4.** A schematic diagram for the model.

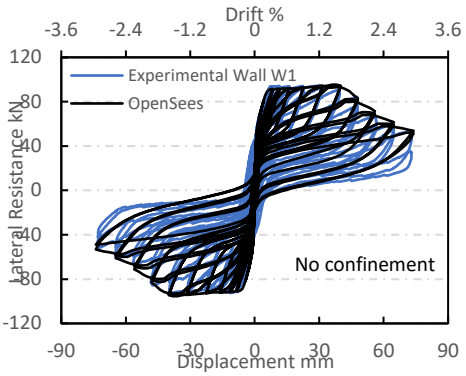
Drift %
-3.6 -2.4 -1.2 0 1.2 2.4 3.6
Experimental Wall W1
OpenSees
No confinement
Lateral Resistance kN
Displacement mm
-90 -60 -30 0 30 60 90

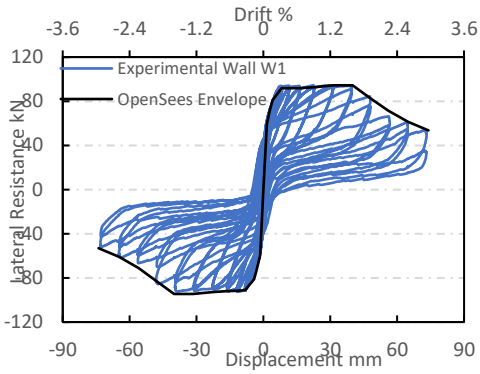
Drift %
-3.6 -2.4 -1.2 0 1.2 2.4 3.6
Experimental Wall W1
OpenSees Envelope
Lateral Resistance kN
Displacement mm
-90 -60 -30 0 30 60 90

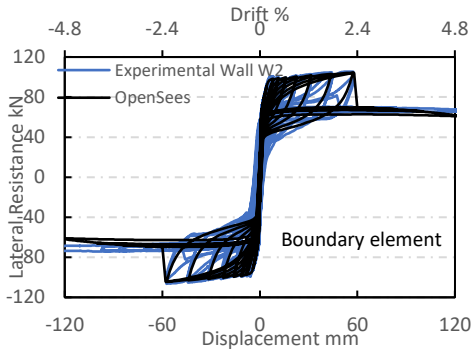
Drift %
-4.8 -2.4 0 2.4 4.8
Experimental Wall W2
OpenSees
Boundary element
Lateral Resistance kN
Displacement mm
-120 -60 0 60 120

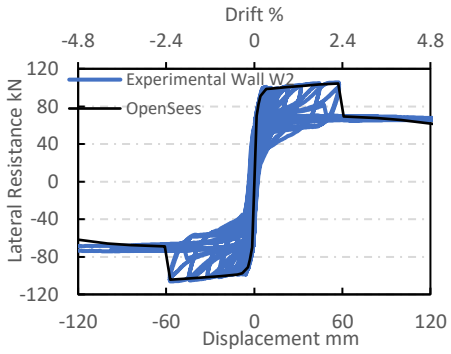
Drift %
-4.8 -2.4 0 2.4 4.8
Experimental Wall W2
OpenSees
Lateral Resistance kN
Displacement mm
-120 -60 0 60 120

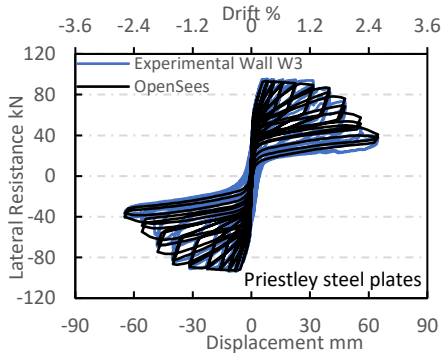
Drift %
-3.6 -2.4 -1.2 0 1.2 2.4 3.6
Experimental Wall W3
OpenSees
Priestley steel plates
Lateral Resistance kN
Displacement mm
-90 -60 -30 0 30 60 90

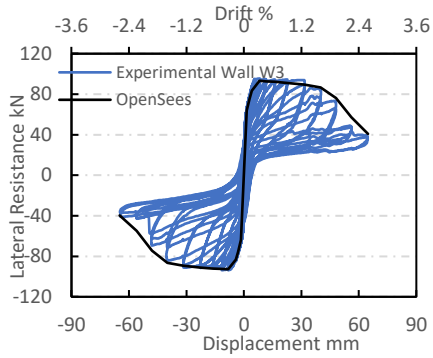
Drift %
-3.6 -2.4 -1.2 0 1.2 2.4 3.6
Experimental Wall W3
OpenSees
Lateral Resistance kN
Displacement mm
-90 -60 -30 0 30 60 90

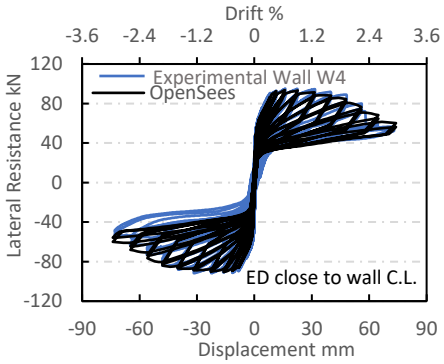
Drift %
-3.6 -2.4 -1.2 0 1.2 2.4 3.6
Experimental Wall W4
OpenSees
ED close to wall C.L.
Lateral Resistance kN
Displacement mm
-90 -60 -30 0 30 60 90

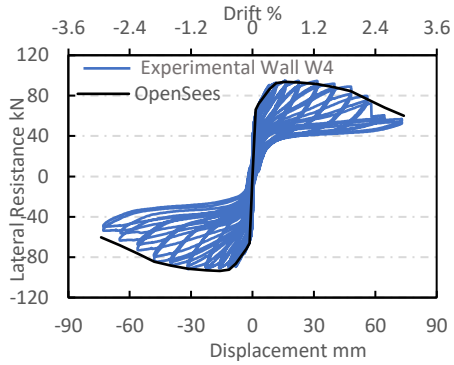
Drift %
-3.6 -2.4 -1.2 0 1.2 2.4 3.6
Experimental Wall W4
OpenSees
Lateral Resistance kN
Displacement mm
-90 -60 -30 0 30 60 90

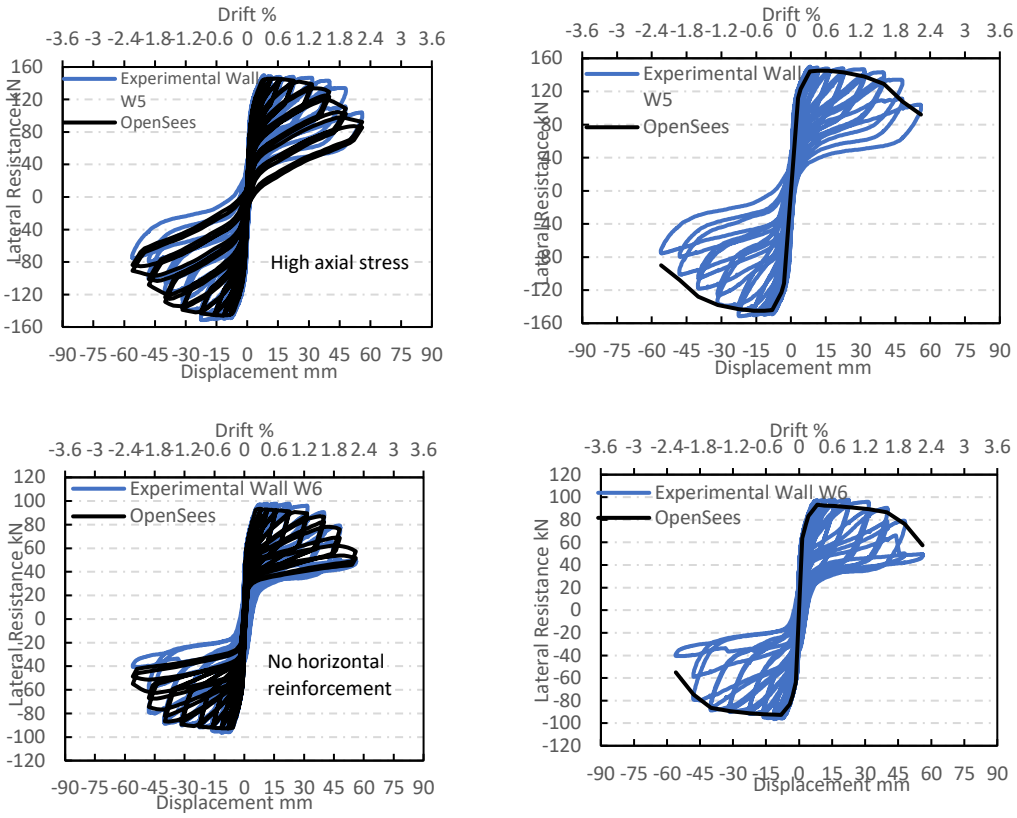


**Fig. 4.5.** Experimental and numerical cyclic responses

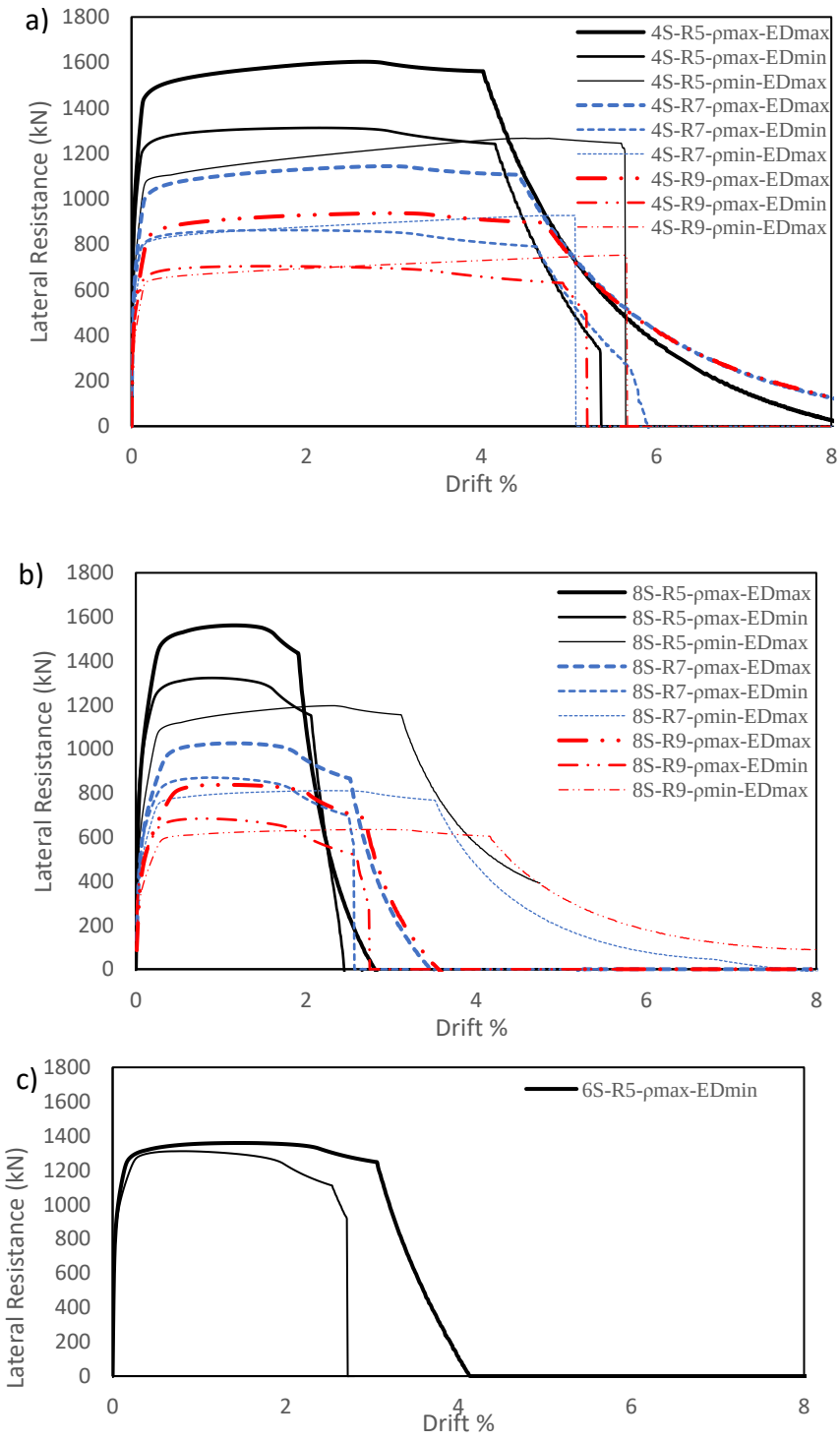


**Fig. 4.6.** Archetype pushover curves for a) 4-story, b) 8-storey, and c) 6-story archetypes

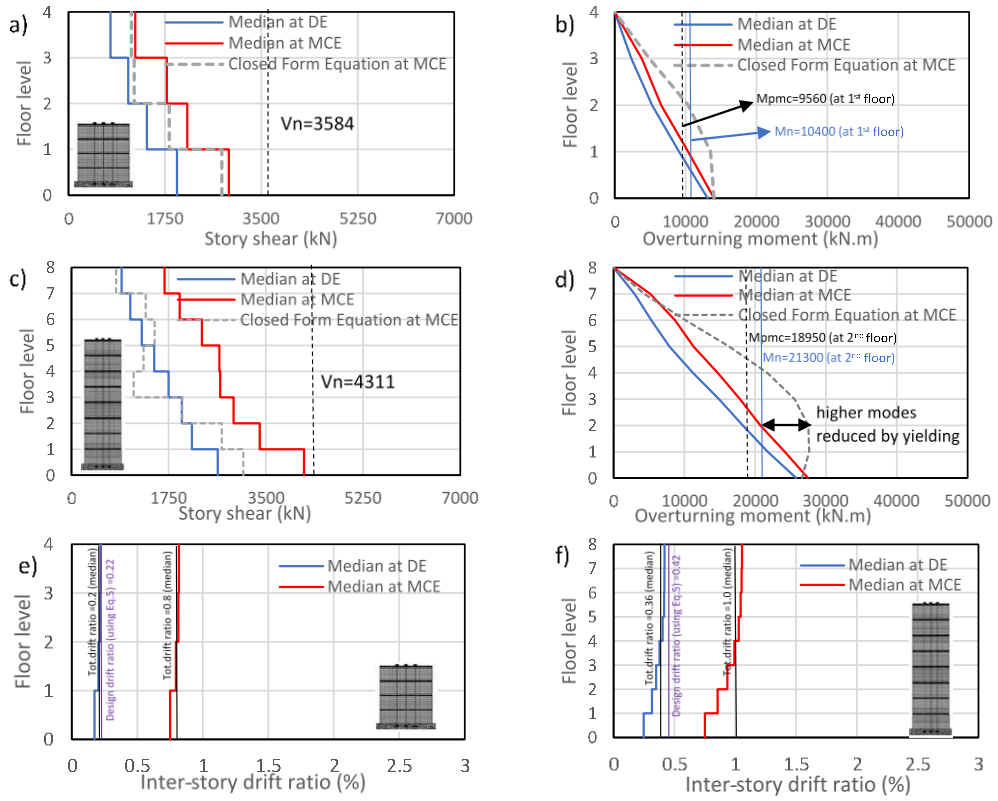


**Fig. 4.7.** Story shear, overturning moments and inter-story drift envelops for a), b), e) 4-story and c), d), f) 8-story walls

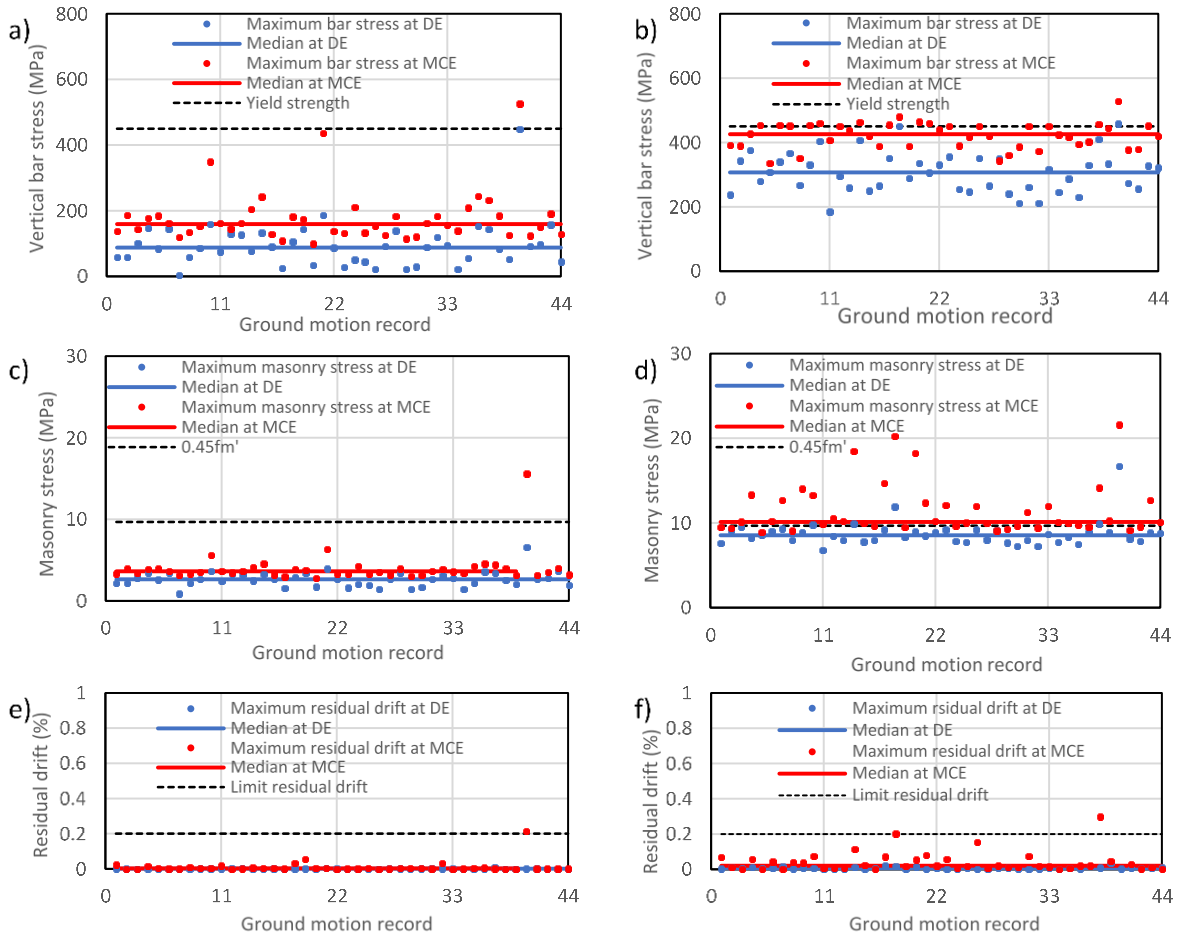


**Fig. 4.8.** Outermost vertical bar stress at a) 1st floor of 4-story wall and b) 2nd floor of 8-story wall; Outermost masonry fiber stress at c) 1st floor of 4-story wall and d) 2nd floor of 8-story wall; and residual drifts for e) the 4-story wall and b) the 8-story wall

# Chapter 5

# EXPERIMENTAL ASSESSMENT OF RESILIENT CONTROLLED ROCKING MASONRY WALLS WITH REPLACEABLE ENERGY DISSIPATION

## 5.1. ABSTRACT

In recent years, several studies have been conducted to evaluate the seismic response of controlled rocking masonry walls (CRMWs) that depend on utilizing unbonded post-tensioning (PT) tendons. The current chapter describes the experimental testing of a proposed controlled rocking masonry walls but without PT and with externally attached energy dissipation (ED-CRMWs). The proposed external ED is a flexural yielding device, named a flexural arm, that is bolted to the wall through a special steel hollow block to allow simple and fast replacement after a seismic event. As such, this wall system overcomes the limitation of internal energy dissipation (ED) devices (e.g., unbonded axial yielding bars) of being unreachable and unreplaceable after damage due to yielding or fracturing. In addition, the chapter reports the retesting of the proposed controlled rocking wall after being repaired and subsequently compares the results to the original wall in order to evaluate the wall seismic resilience, defined herein as the ability of the wall to quickly recover following seismic events. The experimental results are discussed in terms of the failure modes and damage pattern, force-displacement response, wall lateral load capacity, residual drifts, displacement ductility, and ED capacity. The results showed that using a special hollow steel block strategy produced a high

drift capacity of 5.0% drift without strength degradation and preserved the intended self-centering with a maximum residual drift of 0.2% at 3.7% lateral drift. The flexural arm also had significant ductility capacity, where the walls reached 5.0% drift without buckling or fracturing of the arms. Both the original and repaired walls exhibited limited and localized damage at the wall toes, thus presenting the proposed ED-CRMWs as a resilient system in masonry construction practice. Finally, the chapter presents design equations for the introduced ED-CRMWs with flexural arms to be implemented in future relevant standards (e.g., TMS and ACI-ITG 5.2).

## 5.2. INTRODUCTION

Conventional reinforced shear walls (i.e., fixed base walls) are typically designed to dissipate seismic energy through inelastic behavior by yielding their bonded reinforcement while special detailing is maintained to fulfill ductility requirements. This comes at the expense of accepting residual drifts and permanent damage in potential plastic hinge zones. This design approach hinders the overall resilience of such walls because of the costs and time associated with the loss of operation and service shutdown after an earthquake. Conversely, a self-centering mechanism reduces permanent deformations and structural damage during an earthquake event. Therefore, controlled rocking wall systems with such a mechanism are favorable for modern resilient cities because the costs associated with service shutdown (e.g.,

for structural repairs or replacement) are minimized by facilitating rapid recovery of performance. In this respect, controlled rocking wall systems with vertical unbonded post-tensioning (PT) initially received attention through the Precast Seismic Structural Systems (PRESSS) project (Priestley et al. 1999) using reinforced precast concrete shear walls. The experimental results of the PRESSS project showed that the damage was localized and limited to the wall toes with a single crack at the wall-foundation rocking interface. In addition, controlled rocking concrete walls achieved a desirable self-centering response, with almost zero residual drift at the end of the experimental test. These promising results led several researchers to perform further investigations to explore the potential of using masonry walls instead of concrete counterparts (Laursen and Ingham 2001; 2004a; 2004b).

The first study of controlled rocking masonry walls with unbonded post-tensioning (PT-CRMWs) was reported by Laursen (2002), where six fully-grouted walls, one partially-grouted and one ungrouted wall were tested under quasi-static cyclic loading. The experimental results demonstrated that the behavior of fully-grouted walls was similar to that of precast concrete walls regarding self-centering ability and localization of damage at the wall base. Similarly, Rosenboom and Kowalsky (2004) conducted experimental tests using clay masonry blocks instead of concrete blocks. In addition, Hassanli et al. (2016) tested four fully-grouted concrete masonry walls with different configurations of unbonded PT bars and initial stresses. A recent study on the collapse risk of PT-CRMWs has also been

conducted by Yassin et al. (2020) to quantify the collapse margin of safety when such walls were subjected to the maximum considered earthquake level.

Although the PT-CRMW system is considered promising because of the low damage associated with the wall and its ability to self-center, the problems of PT losses and yielding affect the self-centering capability of the system (Hassanli et al. 2016). Moreover, the difficulty of PT implementation during construction continues also to be challenging in practical masonry applications. To address these concerns, six controlled rocking masonry shear walls with internally axial yielding energy dissipation (ED-CRMWs) were recently tested by Yassin et al. (2021a) as a new alternative technique for controlled rocking. In this *Phase I* study, the six ED-CRMWs had no PT tendons, and subsequently, these walls were designed such that the axial load from the tributary slab provided the self-centering ability to the system. This study investigated the effects of PT elimination, adoption of different confining strategies for wall toes, location of the internal energy dissipation (ED) device, and axial stress level on the overall behavior of ED-CRMWs. Yassin et al. (2021a) in *Phase I* reported that all walls achieved a high level of self-centering capability with less than 0.15% residual drift, except for one wall with no confinement at the toes that had a residual drift of 0.45% after loading to 2.1% drift. In addition, the response of all walls was dominated by rocking deformation, and damage was minimized and localized only within the wall toes with no shear or tension cracks. Finally, one wall with boundary elements (i.e., confined using

closed ties) achieved the highest drift capacity (i.e., 2.40% drift) before strength degradation was observed.

Despite the aforementioned promising results of these ED-CRMWs in *Phase I*, one limitation of this system is that the internal ED is unreachable and unreplaceable after a seismic event. Therefore, the current chapter presents *Phase II*, which is a further research investigation towards the possibility of using a replaceable ED device to achieve the intended structural seismic resilience. Specifically, a flexural, rather than axial, ED device named a flexural arm, was externally attached through a bolted connection to a fully-grouted masonry rocking wall and tested under displacement-controlled cyclic loading. This wall had similar dimensions and strength to the six ED-CRMWs tested in *Phase I* to facilitate direct comparison. The geometry of the flexural arms resembled that of the cantilever arms tested by Toranzo et al. (2009) and recently by Li (2019). The connection of the flexural arm to the wall is intended to allow for quick and simple replacement after seismic events. Another observation from *Phase I* (Yassin et al. 2021a) is that the damage in all rectangular walls (i.e., except the wall with boundary elements) always propagated inward, as shown in Fig. 5.1a, after crushing of both wall toes, leading to a reduction in the moment resistance arm and hence strength degradation. In this regard, a hollow steel block was used during the construction, as shown in Fig. 5.1b. This hollow steel block, located only at the second last block of the first course at both wall ends, was used to connect the steel flexural arm directly to the rocking masonry wall through a pin connection as will be discussed in detail later.

It was assembled of small steel plates welded together to have the same dimensions and shape of masonry blocks used. The steel block had also a very high compressive strength and subsequently had the potential for strong confinement for the filling core grout. Finally, after the original wall was tested, the flexural arms were replaced and the wall was repaired and retested to evaluate the system resilience following seismic events.

In this respect, the chapter presents a description of the experimental program, test setup, instrumentation, and repair process. Next, the chapter focuses on comparing the damage sequence, the load-displacement hysteretic behavior, displacement ductility, self-centering capability, and stiffness degradation for the original tested wall (WF) and the repaired wall (WFR), with reference to two walls tested in *Phase I* with internal ED bars (W1 and W2). Finally, a design process for ED-CRMWs with flexural arms is presented as a critical step towards a codified design approach.

## 5.3. EXPERIMENTAL PROGRAM

The experimental program of the current study was designed to evaluate the lateral response of ED-CRMWs without unbonded PT tendons and with external flexural arms using special hollow steel blocks as a confining strategy. The test matrix for the original wall (WF) and its repaired version (WFR) is presented in Table 5.1. Wall WF was designed to have the same lateral resistance as the previously tested ED-CRMWs (W1 and W2) with internal ED (Yassin et al. 2021a). This was performed for comparison purposes to investigate the effect of the new parameters

introduced, namely, the type of the ED device (flexure yielding instead of axial yielding), and the confining strategy (using steel confining block). Further details are provided in the following subsections.

### 5.3.1. WALL SPECIFICATION AND SELECTION CRITERIA

Wall WF was a two-story fully grouted wall and capacity designed to fail in flexure due to toe crushing with adequate horizontal shear reinforcement. Wall WF was constructed with a length of 1895 mm, corresponding to 4000 mm length in full-scale, using half-scale blocks (90 x 90 x 185 mm) that are true replicas of the full-scale concrete blocks (190 x 190 x 390 mm) widely used in North America. The wall rectangular cross-section was 10 courses long and the wall was 13 courses high per story. Two hollow steel blocks, with exact dimensions of the half-scale blocks (i.e., 90 x 90 x 185 mm), were fabricated in the lab by welding small steel plates. These steel blocks were internally roughed (i.e., having small groves) using a grinder to achieve a bond with the grouting core, as shown in Fig. 5.2. The two steel blocks were then used to connect the flexural arms to the wall and also provide confinement. Each block was placed at the second last corner block of the first course, as shown in Fig 5.1b.

The cross-section and reinforcement details of all walls are shown in Fig. 5.3. Horizontal reinforcement was provided at every other course because previous studies (Hassanli et al. 2016, Laursen 2002) reported major diagonal shear cracks due to the absence of minimum horizontal reinforcement. A reinforced concrete (RC) slab was constructed at each story level to exactly follow the construction

procedure of the ED-CRMWs tested in *Phase I*. Minimum vertical bonded D7 bars (area=50 $mm^2$) were provided according to the TMS 402/602 (2016) inside the walls to maintain wall integrity during rocking and to satisfy the standard seismic detailing requirements; however, these D7 bars were terminated at the wall-foundation interface without any connection to the foundation. To transfer the force between the external flexural arm and the masonry wall, 2 M10 bars were welded to the steel block base and extended 800 mm upwards (see Fig. 5.2) inside the wall to ensure an adequate development length under tension, with a lap splice connection above that level.

Walls WF and WFR were subjected to an axial stress of 1.17 MPa, representing normal intensity slab gravity loads and following the axial stress used for *Phase I* walls. As shown in Figs. 2 and 3, four externally attached ED flexural arms (two on each side), which can be replaced after a seismic event, were connected to the wall through the special steel hollow block. Each flexural arm had a thickness of 15.8 mm and a total length of 600 mm which included: i) 230 mm for fixing the arm through a bolted connection with a plate that was embedded in the foundation; ii) 315 mm for the yielding length, $L_o$, that was tapered with a 1:3 slope; and iii) 55 mm for the pin connection with the steel hollow block. All flexural arm dimensions were selected based on the detailed experimental work of Li (2019). Specifically, the yielding length, the tapering slope, and the plate thickness were selected to ensure sufficient base rotation capacity with enough yielding before masonry crushing, where the concentration of plasticity should occur in the

middle of the yielding length as will be presented in detail later in the flexural arm design section. The ED devices were connected to the wall at $\pm$700 mm from the wall centerline, similar to the location of unbonded ED bars used in *Phase I*.

### 5.3.2. CONSTRUCTION

The wall construction was executed using half-scale 5 mm thick mortar joints to represent the 10 mm common full-scale joints. Full details pertaining to the use of scaled masonry units and scaled reinforcement bars in testing models can be found in Harris and Sabnis (1999). Wall WF was built by a professional mason in a running bond pattern with face shell mortar bedding. Two RC slabs, each with 90 mm thickness, were used and reinforced by 3 and 8 M10 bars in the longitudinal and transverse directions, respectively. The wall footing (500 mm thickness x 500 mm width x 2300 mm long) was reinforced by top and bottom M10 bars every 200 mm in both orthogonal directions. A rigid steel loading beam, composed of two 150 mm equal leg angles, was connected to the second story slab by 8 M20 shear studs. Stoppers at a 45° angle were mounted on the footing at the wall ends to prevent sliding at the wall base.

D4 bars (area=25 $mm^2$) were used as horizontal reinforcement at every other course in wall WF. The D4 bars formed 180° hooks around the outermost vertical bonded bars, with a 200 mm return leg that extended to the third-last cell, as shown in Fig. 5.3. Priestley plates (Priestley and Elder 1983) of 1.58 mm thickness were used to protect the wall toes and were placed within the 5 mm bed joint for the first

five courses at both corners, as reported by Yassin et al. (2021a) for *Phase I*. This construction detail ensured encasement of the horizontal reinforcement along with confining plates, steel block, and the grout through the entire length of the wall.

To construct wall WF, steel plates with threaded holes were first placed inside the footing which was then cast. Afterward, the flexural arms were connected to the threaded plate through a group of bolts to form a fixed connection that prevented rotation of the arm, as shown in Fig. 5.4. The construction then followed the typical procedure for reinforced masonry walls that started by placing the masonry blocks of the first course, including the two steel blocks. The integrity of the steel blocks with the surrounding masonry blocks was secured through the horizontal reinforcement being placed starting from the first course in addition to the 2M10 vertical bars that were welded to the steel block base and bonded with the filling grout. The first six courses of the first story were constructed and fully grouted using a high-slump grout with a maximum aggregate size of 5 mm. The remaining seven courses of the wall were then constructed and fully grouted. After the first story was completed, the RC slab formwork was set and reinforcement was placed followed by concrete casting. The same process was repeated for the second story without using the steel blocks.

### 5.3.3. MATERIAL PROPERTIES

The average compressive strength for the half-scale blocks, having a net area of 8,490 $mm^2$, was 35.2 MPa with a coefficient of variation (COV) = 6.5%, complying

with CSA A165-14 (CSA 2014a). For mortar joints, Type S ready mix was used with an average flow of 123% and an average compressive strength of 21.9 MPa (COV = 7.4%) according to CSA A179-14 (CSA 2014d). Grout cylinders were tested as per CSA A179-14 (CSA 2014d) and resulted in an average compressive strength of 21.3 MPa (COV = 10.2%). The footing and story slabs had average concrete compressive strengths of 30.0 MPa (COV=7.3%) and 33.0 MPa (COV=8.9%), respectively. Twelve fully grouted masonry prisms, each composed of four blocks high by one block long (375 mm high x 185 mm long x 90 mm thick), were tested in accordance with CSA S304-14 (CSA 2014c) and yielded an average compressive strength of 19.3 MPa (COV = 9.2%).

Tension tests were performed on the coupons and bars according to CSA G30.18-09 (CSA 2014b). The average yield and ultimate strengths of six coupons, taken from the same plate used to cut the flexural arms, were 435 MPa (COV = 2.4%) and 512 MPa (COV=1.1%), respectively. For the M10 bars used to transfer the tension forces between the ED and wall WF, the average yield strength was 476 MPa (COV = 4.2%). The D7 bars (50 $mm^2$), used as minimum vertical bonded reinforcement, had a yield strength of 461 MPa (COV = 3.2%), while the D4 bars (25 $mm^2$) used for horizontal reinforcement, had 489 MPa (COV = 5.8%). The confining steel plates used at the wall ends were grade 350W with a thickness of 1.58 mm. Also, the steel block was composed of welded small grade 350W steel plates.

### 5.3.4. TEST SETUP

The lateral cyclic load was applied at the second-floor slab using a hydraulic actuator with a capacity of 500 kN and a maximum stroke of ±250 mm. The test setup components and connections are shown in Fig. 5.5. To constrain the wall in the out-of-plane direction, a guidance frame system was used with supports at four points on each slab. Constant axial load, simulating gravity loading, was applied using two hydraulic jacks that were attached at the top of the wall by two 26-mm diameter high-strength rods. These rods were anchored to a steel box section which was attached to the double angle steel loading beam.

### 5.3.5. INSTRUMENTATION

As presented in Fig. 5.6, displacement potentiometers and strain gauges were used to monitor the wall lateral displacements, vertical deformations, uplift, and sliding at the base. Five vertical potentiometers (V1 to V5) were placed to track the gap opening of the base rocking joint (i.e., wall-foundation interface) at the wall ends, centerline, and at 25% of the wall length from both ends. Two linear potentiometers (L1 and L2) were used to monitor the vertical deformations due to masonry axial compression at the wall corners. Lateral displacement potentiometers (H1 to H4) were attached at each slab and mid-story to measure the wall lateral drifts, and two others (H5 and H6) were attached at the footing and wall base to capture any sliding.

Finally, strain gauges (S1-S13) were also used to monitor the strains in both the flexural arms and the M10 bars. The flexural arm was designed to have the

yielding section at the middle of the yielding length, $L_o$. In this regard, two strain gauges (S1-S2 and S5-S6) were placed (bottom and top) at the middle of the yielding length, $L_o$, to track the initiation of yielding in tension and compression. In addition, to track the spread of yielding along $L_o$, another two strain gauges (S3-S4) were placed at the bottom at 0.75 and 0.25 $L_o$ from the pinned end. Moreover, one strain gauge (S7-S10) was placed on each M10 bar at 100 mm from the welded surface with the steel block base, as shown in Fig. 5.6. This strain gauge is mainly to check that the crack width was controlled inside the masonry by ensuring no yielding in the vertical M10 bars in order to limit the wall damage. Finally, strain gauges (S11-S13) were attached to the outermost vertical bonded bars and the horizontal reinforcement.

### 5.3.6. LOADING PROTOCOL

To allow for direct comparison, the FEMA 461 (2007) quasi-static testing protocol, used in *Phase I* (Yassin et al. 2021a), was adopted herein. In this loading protocol, each cycle was repeated twice, and the displacement amplitude was increased by 40% from the previous amplitude. Each test was terminated when either the actuator reached its full stroke capacity or the wall lost 50% of its lateral load resistance, $Q_u$.

## 5.4. TEST RESULTS

### 5.4.1. DAMAGE SEQUENCE AND FAILURE MODES

This section discusses the observed sequence of damage for the original wall (WF) and the repaired wall (WFR). The drift is defined herein as the lateral displacement measured at the horizontal potentiometer, H1, normalized by 2.51 m (i.e., the height from the top face of the footing to H1). Generally, both walls showed a pure rocking response characterized by a gap opening at the base rocking joint. In addition, no sliding was observed between the wall and the foundation at any time throughout the test.

#### 5.4.1.1 Wall WF

The base joint started opening at a drift ratio of 0.06% when the wall started to rock, and this rocking joint opening extended along half the wall length at a drift ratio of 0.13%. Afterward, the flexural arms started to yield at 0.45% drift. At this drift level, no evidence of any tension horizontal cracks was observed over all the bed joints at the location of the 2 M10 bars. This was confirmed through the strain gauge readings (only 25% of the yield strain) at those bars. Minor vertical cracks started to initiate only at both wall corners of the first course at a drift ratio of 0.65%. Subsequently, face shell peeling initiated at these corners at a drift ratio of 0.90%, without propagation of vertical cracking inward. After that, face shell spalling was observed at a drift ratio of 1.25% drift, while the rest of the wall was free of any tension or diagonal shear cracks, as shown in Fig. 5.7. Beyond this drift, crushing

of the compression toe in both corner blocks was observed with a slight degradation in the wall resistance followed by a distinctive behavior, where the wall rocking toe shifted to be the second last block (i.e., steel block). At 1.80% drift, the strain in the top and bottom fibers of the flexural arms reached approximately seven times the yield strain, indicating extensive yielding, but with no lateral torsional buckling. At this drift, the strain in the 2M10 bars was 80% of the yield strain, confirmed by no tension cracks at the bed joints. At 2.80% drift, the strain in the top and bottom fibers of the flexural arms reached twelve times the yield strain, still without lateral torsional buckling being observed. However, at this drift level, the strain in the 2M10 bars reached the yield strain, while no tension cracks were noticed at the bed joints and no strength degradation was observed. Finally, at 5.0% drift, the flexural arm achieved 16 times the yield strain without lateral torsional bucking (see Fig. 5.7) and with stable and full cycles, while the 2M10 bars reached 1.5 times the yield strain with only hairline tension cracks observed at the top of the steel blocks. The blocks remained intact with the wall without any separation, and no strength degradation was observed up to 5% drift. This indicates the effectiveness of the steel block in preserving the wall integrity and strength at high drift levels, and also preventing the propagation of damage inward to the wall centerline as reported in *Phase I* walls (Yassin et al. 2021a). The test was terminated at 5.0% drift due to the actuator stroke limit. At the end of the test, wall WF had damage only at the masonry corner toes of the first course and extensive yielding of the flexural arms,

with no shear cracks or wide tension cracks (i.e., only minor cracks at the top of steel blocks, which closed when the wall was unloaded).

#### 5.4.1.2 Repairing Wall WF

To evaluate the resilience of the proposed system (ED-CRMWs) following seismic events, wall WF was repaired by replacing the four damaged flexural arms with new counterparts, and the corner blocks only of the first course were repaired using a grout batch. As shown in Fig. 5.8, the repairing process started by unbolting the connection to remove the damaged flexural arms. Next, the remained grout at the wall corners was chipped off, followed by surface roughening and cleaning using air blowing to remove any particles that could affect bonding. Afterward, a batch of low water to cement ratio (i.e., w/c 0.45) grout was cast at the corner areas and cured for three days. Finally, the new flexural arms were connected to the wall using the same original bolted connection. After 14 days, the three grout batch cylinders had an average compressive strength of 29.7 MPa, indicating the readiness of the repaired wall WFR to be retested.

#### 5.4.1.3 Wall WFR

The damage of wall WFR followed the same sequence and pattern of wall WF. Specifically, the wall rocking started at a drift ratio of 0.06%, followed by yielding of the flexural arms at 0.45% drift; however, hairline tension cracks occurred above the steel blocks. Vertical cracks started to initiate only at the wall ends at a drift ratio of 0.90%. Subsequently, initiation of crushing was observed at 1.25% drift, while the wall was still free of any diagonal shear cracks. Similar to wall WF,

beyond 1.25% drift, a distinctive behavior occurred as the wall rocking toe shifted to the second last block (i.e., steel block). At 1.80% drift, complete crushing of the wall ends occurred, as shown in Fig. 5.9, and the strain in the flexural arms reached five times the yield strain, thus indicating extensive yielding but without lateral torsional buckling. At 2.80% drift, the strain in the flexural arms reached ten times the yield strain without lateral torsional buckling being observed, and horizontal line cracks (about 0.3mm wide) were observed at the top of the steel blocks, which were still fully intact with the wall. Finally, at 5.0% drift, the flexural arms reached 16 times the yield strain without lateral torsional bucking, and no strength degradation was observed (see Fig. 5.9). These results confirm the efficiency of the steel blocks, which preserved the connection with the flexural arms and prevented the propagation of damage at high drifts even after the wall was retested. After the test, an inspection of the steel block showed that the grout inside the steel block was fully confined without crushing and the 2M10 rebars were fully bonded to the block, as shown in Fig. 5.9.

### 5.4.2. FORCE-DISPLACEMENT RESPONSE

The force measured by the load cell of the hydraulic actuator is plotted against the lateral displacement of the horizontal string potentiometer, H1, for each wall in Fig. 5.10. As shown in the figure, walls WF and WFR had stiffness degradation starting from 0.65% drift to 1.30% drift. Beyond 1.30% drift, no stiffness degradation was observed in either wall, and no in-cycle strength or stiffness degradation (i.e., repeated cycles are essentially identical) was observed in either wall until the end

of the test at 5% drift. This is because, at the first stage (i.e., from 0.65% to 1.30% drift), the degradation was due to the deterioration of the crushing toes at the wall ends. While in the second stage (beyond 1.30% drift), the wall did not have any further deterioration because the rocking was shifted on the strong steel blocks. Another observation is that a reduction in wall WFR strength in the push (+ve) and pull (-ve) directions occurred at 1.25% drift due to crushing of the right corner block, and similarly, wall WF in the push (+ve) direction, leading to a reduction in the moment resistance arm, while the tension in the flexural arms is the same given that same uplift value on the pull side. Afterward, the rocking pivoted on the steel blocks, which sustained more compression than the masonry units. This led to a gradual increase in the resistance of the walls, as larger forces were developed inside the arms as drift increased, as shown in Fig. 5.10a and b. Both observations confirm the efficiency of the steel blocks on the wall response.

As shown in Fig. 5.10c, d and e, walls WF and WFR have very similar hysteretic loops, with deviations in the enclosed areas of 14.8%, 12.7%, and 8.1% at drifts of 0.9%, 2.8%, and 5.0%, respectively. This reflects the success of the repairing technique and the efficacy of the replaced flexural arms in restoring the system's supplemental damping.

### 5.4.3. LATERAL LOAD CAPACITY AND DISPLACEMENT CHARACTERISTICS

Figure 5.11 compares the envelopes of the load-displacement relationships for: 1) walls WF and WFR with external flexural arms; and 2) walls W1 and W2 with

internal axial yielding unbonded bars tested in *Phase I* (Yassin et al. 2021a). Wall WF was designed to have approximately the same lateral resistance as walls W1 and W2. This facilitated the comparison between the different ED systems. Comparing the response of walls WF and WFR shown in Fig. 5.11, the maximum deviations in the wall resistance are 6% and 10% in the push (+ve) and pull (-ve) directions, respectively. This indicates that the repairing technique was successful to keep the strength of wall WFR at least 90% of that of wall WF throughout the test. Both walls reached the decompression stage at 0.06% drift, where the decompression strength, $Q_o$, was 60 kN and 56 kN for walls WF and WFR, respectively. The next stage was the yielding of the flexural arms, where wall WF exhibited yielding at a strength, $Q_y$, of 95 kN on average, while wall WFR reached yielding at a strength, $Q_y$, of 89 kN on average.

Comparing walls WF and WFR (*Phase II*) to walls W1 and W2 (*Phase I*), Fig. 5.11 shows that flexural arms with steel blocks addressed two issues from *Phase I*. The first issue was the fracturing of the axial yielding bar due to low cycle fatigue that occurred in wall W2, which subsequently caused a sudden drop in the strength at 2.3% drift, whereas the flexural arms provided a stable response up to 5% drift. The second issue was the crushing of the toe that propagated inward and resulted in gradual strength degradation in wall W1, whereas the steel block in wall WF prevented this damage propagation up to 5% drift.

### 5.4.4. SELF-CENTERING

The ratio between the moment contribution from ED and the moment contribution from restoring forces (i.e., gravity load) was assumed to be 0.35 as reported in *Phase I* to allow for direct comparison. To quantify the self-centering capability, Fig. 5.12 plots the average residual drift of the push and pull directions, $d_r$, taken at the end of the first cycle at each displacement level with zero lateral force against the corresponding peak drift of that cycle. The residual drifts for wall WF remained less than 0.2% (5 mm) after every cycle up to a drift ratio of 3.7%, after which the strain hardening of the ED reduced the self-centering capability. A residual drift of 0.2% is considered acceptable as it represents the limit for damage state (DS1) as per FEMA P58 (2018), where no structural realignment or repair is required even though non-structural repair may be required. Similarly, wall WFR had residual drifts less than 0.2% until a drift ratio of 3.5%, thus demonstrating the adequacy of the repairing technique in preserving the wall self-centering capability. In comparison, wall W1 in *Phase I* reached 0.2% residual drift after a drift ratio of only 2.1% due to the toe deterioration, while wall W2 preserved a unique self-centering capability as the residual drifts remained less than 0.12% after every cycle due to the fracture of ED bars and the confinement of the crushing toes with closed ties within the boundary element region.

### 5.4.5. DISPLACEMENT DUCTILITY

Since walls WF and WFR did not reach 20% strength degradation until the end of the test, the displacement ductility, $\mu_{\Delta u}$, is defined herein as the ratio between the displacement corresponding to wall ultimate resistance and the displacement corresponding to the onset of ED bar yielding (confirmed by strain gauge readings), without any idealization of the load-displacement relationship.

As shown in Table 5.2, the drifts attained by walls WF and WFR at peak resistance were 250 and 200% higher than those of walls W1 and W2, respectively. While the axial unbonded bars yielded at 0.22% drift, the yielding of the flexural arm of walls WF and WFR were delayed to 0.45% drift. The net effect of both delayed yield and high displacement capacity resulted in an enhancement in the displacement ductility, $\mu_{\Delta u}$, compared to wall W1, of about 90% on average. Conversely, early yielding of wall W2 led to a slightly higher displacement ductility relative to walls WF and WFR, as presented in Table 5.2.

### 5.4.6. ENERGY DISSIPATION AND HYSTERETIC DAMPING

Energy dissipation is reported to compare the efficiency of the hysteretic damping of the new supplemental ED devices that were implemented in this study (flexure yielding versus axial yielding). In this regard, the ED in this chapter is defined by the area enclosed by the load-displacement curve passing through the envelope values (Hose and Seible 1999). The increase in cumulative ED with drift is shown in Fig. 5.13a for walls with flexural arms (WF and WFR) and for walls with axial

yielding bars (W1 and W2). As shown in this figure, walls W1 and W2 provided more ED at lower drifts as yielding occurred at the early stages of loading; however, the flexural arms had much higher displacement capacities than the axial yielding bars, resulting in higher cumulative ED from walls WF and WFR beyond about 3% drift. This is because the axial yielding bars were susceptible to low cycle fatigue that caused bars fracturing at 2.85% drift for W1 and 2.3% drift for W2. Regarding the repair method, as shown in Fig. 5.13a, the maximum deviation in cumulative ED of wall WRF is 12.1%, which indicates the effectiveness of the repairing technique in restoring the system supplemental damping, indicating high structural resilience.

The equivalent viscous damping ratio, $\xi_{eq}$, is used in the current study to facilitate the comparison between both yielding devices in terms of the wall damage under cyclic loading (Priestley et al. 2007). In this regard, this parameter is obtained by equating the elastic strain energy dissipated by a system with the energy dissipated from nonlinear behavior (Jacobsen 1930), and calculated as shown in Eq. (5.1):

$$\xi_{eq} = \frac{E_d}{4\pi E_s} \tag{5.1}$$

where $E_d$ is the dissipated energy of the cycle, and $E_s$ is the stored strain energy of the cycle. As shown in Fig. 5.13b, walls with flexural arms (WF and WFR) experienced a high level of stable and increasing damping as drift levels increased, which would be expected to reduce seismic demands at high drifts. This is due to

the high ductility through reaching high levels of inelastic strain compared to walls with axial yielding (W1 and W2).

## 5.5. DESIGN RECOMMENDATIONS FOR WALLS WITH FLEXURAL ARMS

In this section, the design approach is based on the design guidelines proposed by Yassin et al. (2021b) with the inclusion of flexural arm dimensions selection to satisfy the design requirement at design level earthquake. Similar to the unbonded length selection in axial yielding bar ED (Yassin et al. 2021b), the yielding deflection of the flexural arm, $\delta_{yield}$, is essential for the flexural arm design selection and implementation to the wall. Hence an equation, based on the flexural arm dimensions and material strength, is proposed in the current study to predict the yielding deflection of the flexural arm and is subsequently validated with the experimental test results of walls WF and WFR. The equation provided here is initially based on the work of Ma et al. (2010) that used butterfly fuses with double curvature end conditions, and the experimental testing and analysis conducted by Li (2019). The simplest form of the proposed equation for yielding deflection, $\delta_{yield}$, of the flexural arm is shown in Eq. 5.2. In this equation, the in-plane dimensions of the arm ($L_o$, $y_1$) are linked to the wall uplift demand at the yielding stage as shown in Fig. 5.14.

$$\delta_{yield} = \frac{2}{3}\frac{L_o^2}{y_1}\varepsilon_y \tag{5.2}$$

where $L_o$ is the flexural arm yielding length, $y_1$ is the minimum tapered dimension of the flexural arm, and $\varepsilon_y$ is the yield strain of the steel arm (see Fig. 5.14). This equation derivation is based on reaching the maximum bending stress at the middle of the flexural arm yielding length (where yielding is initiated) and the ratio between the minimum and maximum tapered dimension ($y_1$/ $y_2$) must be 1/3 to satisfy the yielding location.

To measure the robustness of the proposed Eq. 5.2, it is validated with the experimental test results of walls WF and WFR. As shown in Table 5.2, the maximum deviation was 6% between the predicted yield deflection, $\delta_{yield\text{-}Pred}$, and the measured uplift of the flexural arm pin connection with the wall at yielding, $\delta_{exp.}$, based on strain gauges yielding at the middle of the flexural arm yielding length.

The wall drift demands (see Fig. 5.14) at design level $\Delta_d$ is calculated as proposed by Yassin et al. (2021b), and then the base rotation at the design level, $\theta_d$, is calculated as the top drift ratio at the design level over the wall height, $\Delta_d/H_w$, as the total response is governed by rocking based on experimental studies (Yassin et al. 2021a; Hassanli et al. 2016). Afterwards, similar to the unbonded axial yielding bar ED design (Yassin at al. 2021b), at the design-level drift $\Delta_d$, the flexural arm yielding is intended to reach at least tensile strain, $\varepsilon_{sD}$, of $4\varepsilon_y$ to ensure sufficient base rotation ductility and sufficient yielding before masonry crushing as per TMS (2016) for special reinforced masonry walls. In this regard, the design-level drift, $\Delta_d$, is assumed to be equal at least twice the wall yielding drift, $\Delta_y$, based on the

experimental results of walls WF and WFR, where the arm deflection was twice the flexural arm yielding deflection, $\delta_{yield}$, when the strain in the bottom middle of the arm reached $4\varepsilon_{y.}$ Therefore, to link the wall drift demands at the design-basis earthquake level with the required in-plane dimensions of the flexural arm ($L_o$, $y_1$), Eq. 5.3 is used.

$$\chi\delta_{yield} = (d_{ED} - c)\theta_d \quad \text{, where} \quad \chi \geq 2 \quad \text{for} \quad \varepsilon_{sD} \geq 4\varepsilon_y \tag{5.3}$$

where $d_{ED}$ is the location of the ED from the arm pin connection to the outermost compression fiber of the wall. From Eqs. 2 and 3, the in-plane dimensions ($L_o$, $y_1$) of the flexural arm were calculated by assuming one unknown and calculating the other.

As per the design guideline proposed by Yassin et al. (2021b), to calculate the base rocking joint moment capacity, $M_{Rock}$, the ED yielding force, $Q_{yED}$, is required, which is calculated based on achieving self-centering. To satisfy the required ED force contribution from the flexural arm, the thickness of the flexural arm plate, $t_p$, is calculated as shown in Eq. 5.4. This equation is based on the yielding moment, $M_y$, which is the moment required to cause the stresses to be maximum at $0.5L_o$ and equal to yield stress, $\sigma_y$. From Eq. 5.2 and Eq. 5.4, it is clear that the selection of the thickness of the flexural arm, $t_p$, affects the yield strength but not the yielding deflection. It should be noted that Eq. 5.4 is based on assuming the flexural arm is prismatic, and this assumption is allowed with the limitation of the tapering angle, $\psi$, given in Eq. 5.5, where the error in stress calculation is less than 5% (Hibbeler 2016). In the current study, the flexural arm dimensions $L_o$, $y_1$,

$y_2$, and $t_p$ are 315 mm, 32 mm, 96 mm, 15.875 mm, respectively, yielding a tapering angle, $\psi$, of 5.8°.

$$Q_{yED} = \frac{M_y}{L_o} = \frac{4}{3}\frac{y_1^2 t_p}{L_o}\sigma_y \tag{5.4}$$

$$\mathrm{Tan}^{-1}\psi = \frac{y_2 - y_1}{2L_o} \quad \leq 15^{\circ} \tag{5.5}$$

The flexural strength prediction for ED-CRMWs is calculated using the TMS 402/602 (2016) expression, where the equivalent rectangular stress block, $a$, is calculated from Eq. 5.6. The strength predictions were carried out without material or strength reduction factors applied as shown in Eq. 5.7.

$$a = \frac{W + Q_{yED}}{0.8 f_m^{'} b} \tag{5.6}$$

$$M_n = W(\frac{L_w - a}{2}) + Q_{yED}(d_{ED} - a/2) \tag{5.7}$$

where $W$ is the gravity loads, $f_m^{'}$ is the masonry compressive strength, $b$ is the wall thickness, and $L_w$ is wall length. The predicted flexural strength of ED-CRMWs is equal to the nominal moment capacity, $M_n$, provided in Eq. 5.7 divided by the wall height. The flexural strength predictions according to TMS 402/602 (2016) are presented in Table 5.2, by which the predicted and measured strength are denoted by $V_{pr}$ and $V_{exp}$ respectively. In general, the results in Table 5.2 indicate that the use of TMS 402/602 (2016) resulted in accurate flexural strength predictions of ED-CRMWs for both configurations (i.e., flexural arms and axial yielding bars) with a deviation of 9% for the original wall WF. This indicates that the proposed system

category can be easily adopted in North American codes with almost no modifications to the existing strength calculation clauses pertaining to PT-CRMWs.

## 5.6. CONCLUSIONS

This chapter reported the experimental results of controlled rocking masonry walls with externally attached energy dissipation (ED-CRMWs). The newly proposed connection for externally attached flexural arms used special hollow steel blocks that had the advantage of quick and simple arm replacement after seismic events through bolted connections. Original wall (wall WF) with flexural arms was tested under quasi-static cyclic loading up to 5% drift. Repairing and retesting of the same wall (wall WFR) was then reported and results were compared to those of wall WF to quantify the system resilience and the efficiency of the restoration technique. Finally, this chapter presented design guidelines for the newly introduced flexural energy dissipation (ED) to facilitate the implementation of this wall system in future relevant design standards. The experimental results of walls WF and WFR were compared to two previously tested ED-CRMWs (W1 and W2) that had internally attached axial yielding ED. The experimental work presented in this chapter led to the following observations and conclusions for the ED-CRMW system with externally attached flexural arms:

1- The use of only two hollow steel blocks at the wall corners fully preserved the integrity of the wall while being fully intact with the surrounding blocks up to 5% drift. The steel blocks prevented the propagation of damage inwards toward the wall centerline and limited the damage to occur only in

the corner masonry blocks, which were easily repaired. In addition, no strength degradation was observed until the end of the tests at 5% drift, and no stiffness degradation or in-cycle stiffness degradation occurred. Moreover, wall WF reached a drift of 3.7% with a residual drift less than 0.2% (5 mm), thus reflecting the high self-centering capability of the proposed system at high drift levels.

2- The flexural arms had the advantage of achieving high deformations (e.g. 16 times the yield strain at 5% drift) with stable hysteretic loops and without fracturing or lateral torsional buckling, unlike axial yielding bars that suffered from buckling and fracturing at 2.85% drift. Also, the flexural arm had the advantage of being easy to reach and replace after seismic events, thus allowing for much simpler system recovery than for walls with internally attached axial yielding bars.

3- The resistance of the wall was restored after testing to 5% drift and repair, with average deviations of 3.5% and 7.8% in the push (+ve) and pull (-ve) directions, respectively, at different drift levels. In addition, the repaired wall WFR was able to achieve again a high drift capacity of 5% without strength degradation or in-cycle stiffness degradation. Also, the damage was limited to the flexural arms and the wall corners within the first course only. Moreover, wall WFR reached a drift of 3.5% with a residual drift of less than 0.2%. This indicates the adequacy of the repairing technique which restored the wall self-centering capability.

4- The proposed equations for calculating the yield displacement of the flexural arms showed a good estimate with a maximum deviation of 6%. Also, wall strength predictions based on TMS (2016) expression were accurate with an 8% deviation, showing that the proposed system can be easily adopted in North American codes with almost no modifications to the existing strength calculation clauses pertaining to PT-CRMWs.

## 5.7. ACKNOWLEDGMENTS

The financial support for this project was provided through the Canadian Concrete Masonry Producers Association (CCMPA), the Canada Masonry Design Centre (CMDC), the Natural Sciences and Engineering Research Council (NSERC) and the Ontario Centres of Excellence (OCE).

## 5.8. REFERENCES

ACI ITG-5.2 (American Concrete Institute). (2009). "Requirements for Design of a Special Unbonded Post-Tensioned Precast Shear Wall Satisfying ACI ITG-5.1 & Commentary." ACI ITG-5.2-09, Farmington Hills, MI.

CSA (Canadian Standards Association). (2014a). "Standards on concrete masonry units." CSA A165-14, Mississauga, ON, Canada.

CSA (Canadian Standards Association). (2014b). "Carbon steel bars for concrete reinforcement." CSA G30.18-09, Mississauga, ON, Canada.

CSA (Canadian Standards Association). (2014c). "Design of masonry structures." CSA S304-14, Mississauga, ON, Canada.

CSA (Canadian Standards Association). (2014d). "Mortar and grout for unit masonry." CSA A179-14, Mississauga, ON, Canada.

FEMA. (2007) ."Interim testing protocols for determining the seismic performance characteristics of structural and nonstructural components." FEMA 461, Washington, DC.

FEMA. (2018). "Seismic performance assessment of buildings" FEMA-P58, Washington, DC.

Harris, H., and Sabnis, G.M. (1999). "Structural Modeling and Experimental Techniques (2nd ed.)". CRC Press. https://doi.org/10.1201/9780367802295

Hassanli, R., ElGawady, M., and Mills, J. (2016). "Experimental investigation of in-plane cyclic response of unbonded-posttensioned masonry walls." Journal of Structural Engineering, 142(5), 04015171-1-15.

Hibbeler, R C. (2016). Mechanics of Materials. Upper Saddle River, N.J: Pearson Education

Hose, Y., and Seible, F. (1999). "Performance evaluation database for concrete bridge components, and systems under simulated seismic loads." PEER Rep. No. 1999/11, Pacific Earthquake Engineering Research Center, College of Engineering, Univ. of California, Berkeley, CA.

Jacobsen, L. S. (1930). "Steady forced vibrations as influenced by damping." ASME Transactione, 52(1), 169–181.

Laursen, P. T. and Ingham, J. M. (2001). "Structural Testing of Single-Story Post-Tensioned Concrete Masonry Walls." The Professional Journal of The Masonry Society, 19(1), 69-82.

Laursen, P. T. and Ingham, J. M. (2004a). "Structural testing of enhanced post-tensioned concrete masonry walls." ACI Journal, 101(6), 852-862.

Laursen, P. T. and Ingham, J. M. (2004b). "Structural testing of large-scale posttensioned concrete masonry walls." Journal of Structural Engineering, 130(10), 1497-1505.

Laursen, P. T. (2002). "Seismic analysis and design of post-tensioned concrete masonry walls." PhD Thesis, Department of Civil and Environmental Engineering, University of Auckland.

Li, J. (2019) Development of a flexural yielding energy dissipation device for controlled rocking masonry walls, MASc Thesis: McMaster University.

Ma, X., Borchers, E., Pena, A., Krawinkler, H., Billington, S., and Deierlein, G. G. (2010). "Design and behaviour of steel shear plates with openings as energy-dissipating fuses." The John A. Blume Earthquake Engineering Center (2010), Report No.173.

Priestley, N., Calvi, G., and Kowalsky, M. (2007). Displacement-based seismic design of structures, IUSS, Pavia, Italy.

Priestley, M. J. N., and Elder, D. M. (1983). "Stress-strain curves for unconfined and confined concrete masonry." ACI Journal, 80(19), 192–201.

Priestley, M. J. N., Sritharan, S., Conley, J.R., and Pampanin, S. (1999). "Preliminary results and conclusions from the PRESSS five-story precast concrete test building." PCI Journal, 44(6), 42–67.

Rosenboom, O. A., and Kowalsky, M. J. (2004). "Reversed in-plane cyclic behavior of posttensioned clay brick masonry walls." Journal of Structural Engineering, 10.1061/(ASCE)0733-9445(2004)130:5(787), 787–798.

TMS (The Masonry Society). (2016). "Building Code Requirements and Specification for Masonry Structures." TMS 402/602-16, Longmont, CO.

Toranzo, L. A., Restrepo, J. I., Mander, J. B., and Carr, A. J. (2009). "Shake-table tests of confined-masonry rocking walls with supplementary hysteretic damping." Journal of Earthquake Engineering, Vol. 13, No.6, pp. 882-898.

Yassin, A., Ezzeldin, M., Steele, T., and Wiebe, L. (2020). "Seismic collapse risk assessment of post-tensioned controlled rocking masonry walls." J. Struct. Eng., 146(5), 04020060-1-16.

Yassin, A., Ezzeldin, M., and Wiebe, L. (2021a). "Experimental Assessment of Controlled Rocking Masonry Shear Walls without Posttensioning." Submitted.

Yassin, A., Ezzeldin, M., and Wiebe, L. (2021b). "Seismic Design and Performance Evaluation of Controlled Rocking Masonry Shear Walls without Posttensioning." Submitted.

## 5.9. TABLES

**Table 5.1.** Test matrix and specimen details of ED-CRMWs.

| Specimen | Wall type (ED used) | Wall dimension LxH (mm) | Vertical reinforcement | Shear reinforcement | Axial stress (MPa) | Confinement |
|---|---|---|---|---|---|---|
| WF | Original Wall (External flexural arms) | 1895 x 2660 | 6D7 + 4M10 | D4 every other course | 1.17 | 2 Hollow steel blocks + Priestley plates |
| WFR | Repaired Wall (External flexural arms) | 1895 x 2660 | 6D7 + 4M10 | D4 every other course | 1.17 | 2 Hollow steel blocks + Priestley plates |
| W1[a] | Unconfined (Internal axial yielding bars) | 1895 x 2660 | 6D7 + 2M10 | D4 every other course | 1.17 | None |
| W2[a] | End-Confined (Internal axial yielding bars) | 1895 x 2660 | 4D7+ 2M10 @Web, 8D7 @ Ends | D4 every other course | 1.17 | D4 closed ties every other course |

[a] Yassin at al. 2021a

**Table 5.2.** Summary of Displacements, Displacement Ductility, Predicted and Measured Strength.

| Wall | Wall type | Direction | $\Delta_y$ (mm) | $\Delta_u$ (mm) | $\mu_{\Delta u}$ | $\delta_{yield\text{-}Pred}$ (mm) | $\delta_{exp}$ (mm) | $y_{yield\text{-}Pred}/y_{exp}$ | $V_{pr}$ (kN) | $V_{exp}$ (kN) | $V_{pr}/V_{exp}$ |
|---|---|---|---|---|---|---|---|---|---|---|---|
| WF | Main Wall | Push | 11.2 | 125.0[a] | 11.2[a] | 4.65 | 4.83[b] | 0.96 | 113.9 | 105.1 | 1.08 |
| | | Pull | 10.9 | 125.0[a] | 11.5[a] | 4.65 | 4.88[b] | 0.95 | 113.9 | 103.6 | 1.09 |
| WFR | Repaired Wall | Push | 11.3 | 125.0[a] | 11.0[a] | 4.65 | 4.90[b] | 0.94 | 113.9 | 106.4 | 1.07 |
| | | Pull | 11.1 | 125.0[a] | 11.2[a] | 4.65 | 4.94[b] | 0.94 | 113.9 | 97.8 | 1.16 |
| W1 | Unconfined | Push | 5.7 | 32.1 | 5.6 | N.A. | N.A. | N.A. | 92.3 | 92.5 | 0.99 |
| | | Pull | 5.9 | 38.5 | 6.5 | N.A. | N.A. | N.A. | 92.3 | 93.0 | 0.99 |
| W2 | End-Confined | Push | 4.7 | 58.1 | 12.4 | N.A. | N.A. | N.A. | 97.5 | 104.1 | 0.94 |
| | | Pull | 4.5 | 58.2 | 12.9 | N.A. | N.A. | N.A. | 97.5 | 104.5 | 0.93 |

[a] limited by actuator stroke capacity

[b] average reading of flexural arms

## 5.10. FIGURES

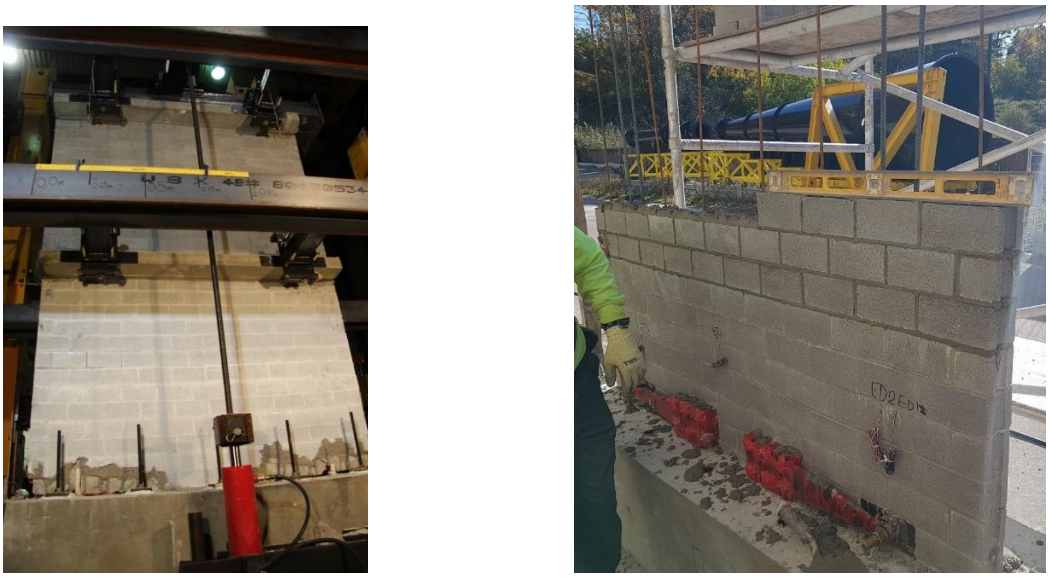

a) b)

**Fig. 5.1.** a) W1 Damage propagation inward for ED-CRMW with internal energy dissipation (Yassin et al. 2021a), b) Hollow steel block located at the second last block connected with flexural arms


**Fig. 5.2.** Hollow steel block internal connection with flexural arms

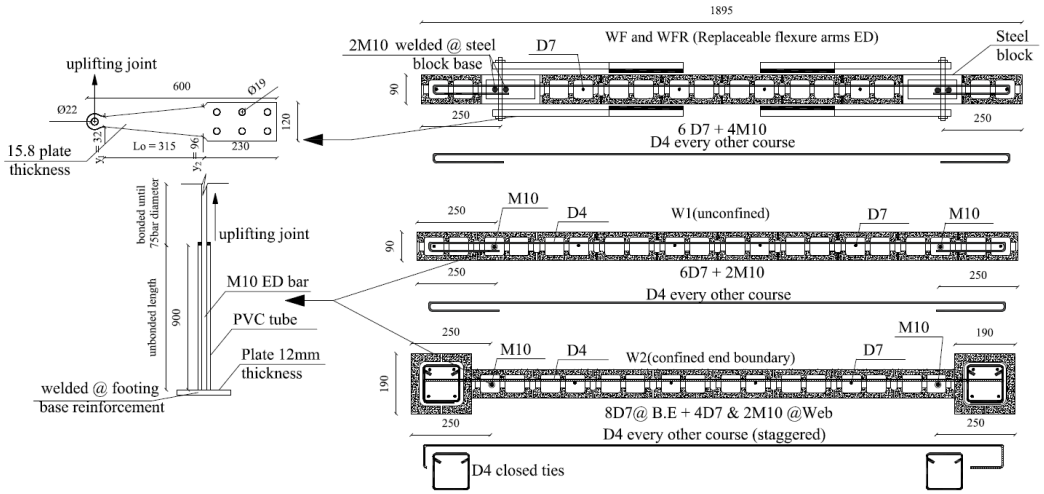


**Fig. 5.3.** ED-CRMWs cross-section and reinforcement details (all dimensions are in mm)

a) b)

**Fig. 5.4.** a) Placing of the threaded plate into the footing, b) Connecting the flexural arms with the threaded plate

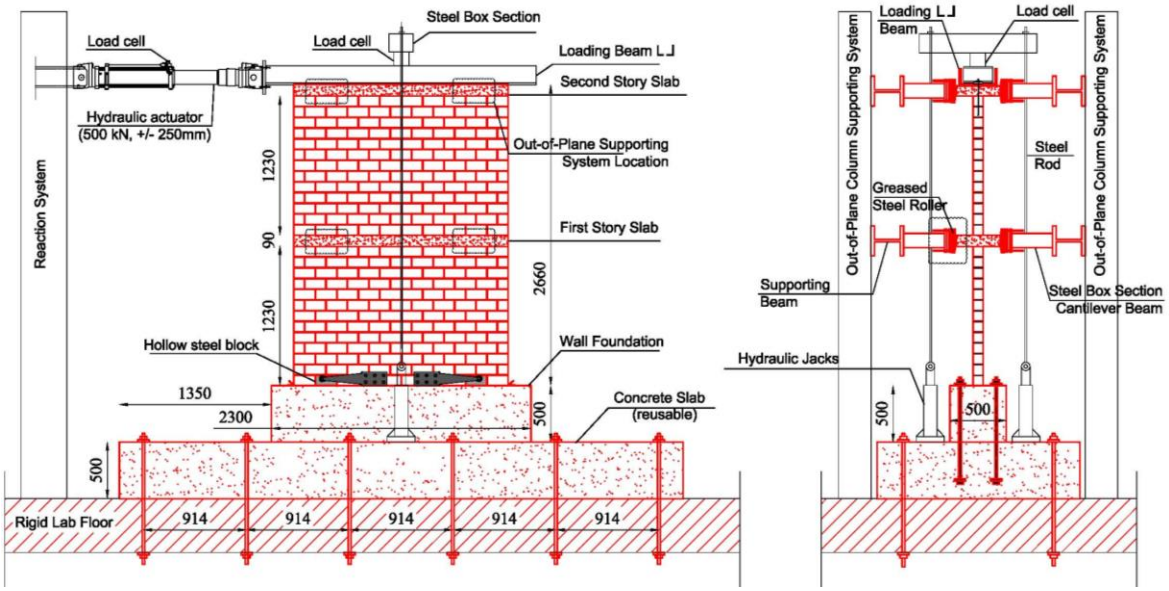


**Fig. 5.5.** Test setup

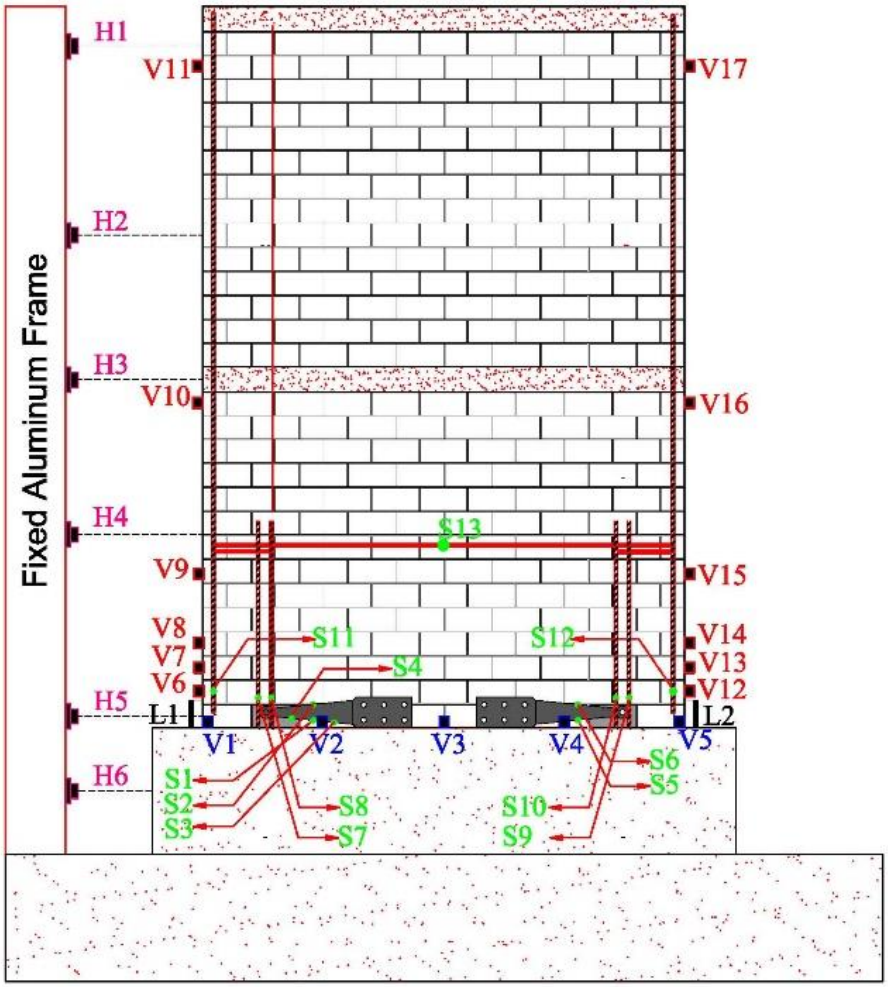


**Fig. 5.6.** Typical wall instrumentation

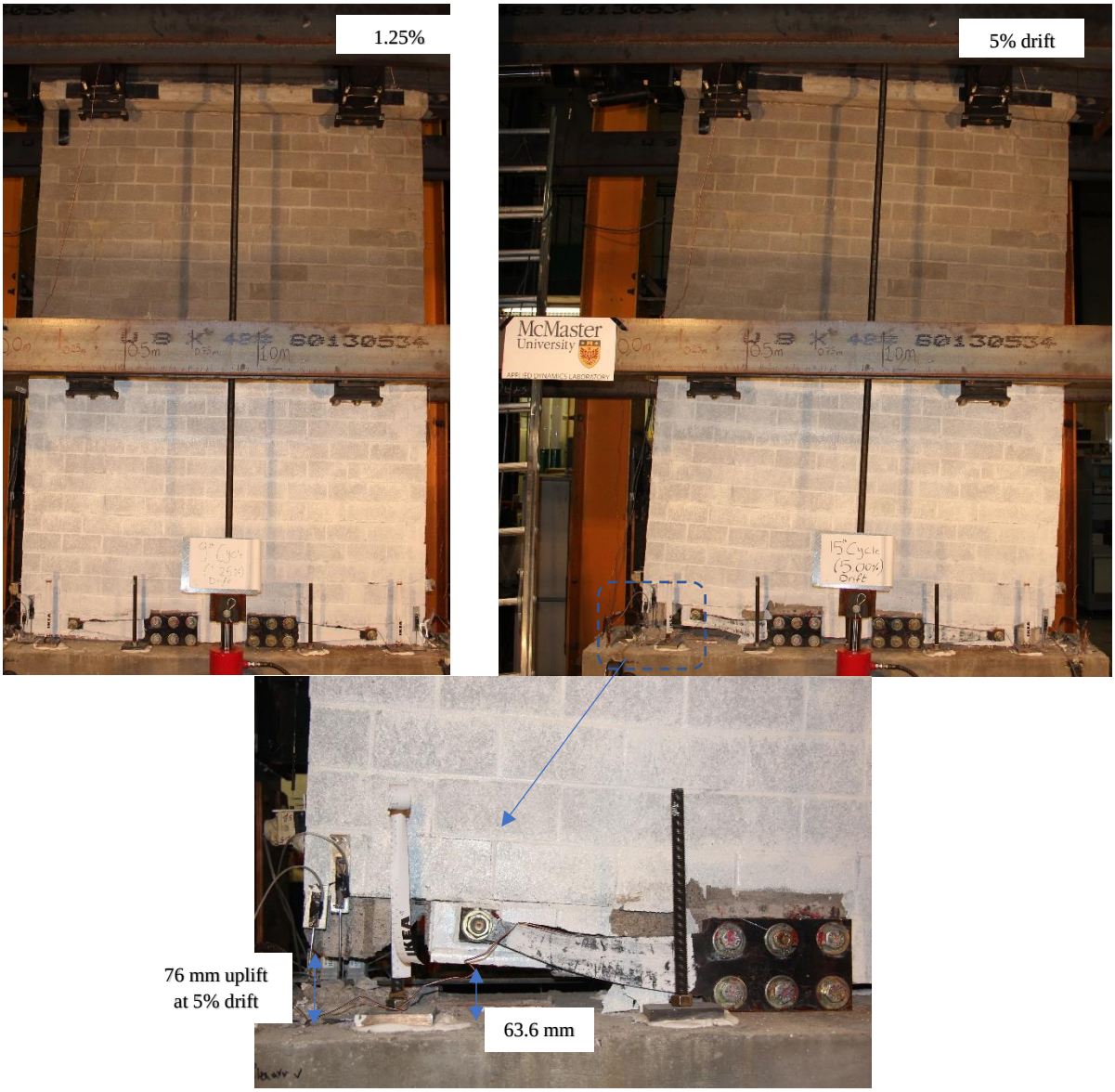


**Fig. 5.7.** Damage of wall WF


**Fig. 5.8.** Repairing stages of wall WF


**Fig. 5.9.** a) Damage of wall WFR, b) Steel block condition after testing wall WFR

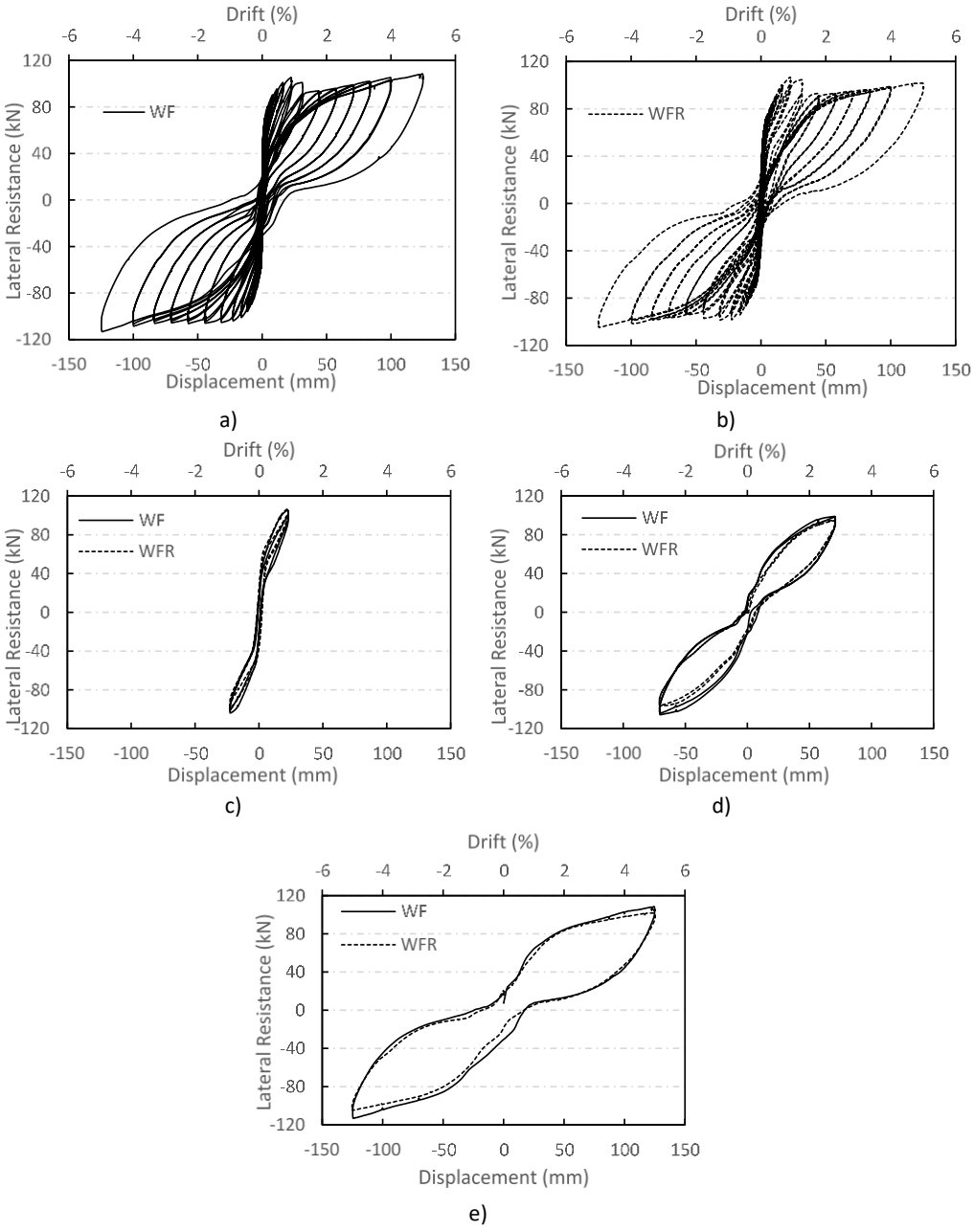


**Fig. 5.10.** Load-displacement hysteresis loops for a) wall WF, b) wall WFR, both walls at c) 0.9% drift, d) 2.8% drift, and e) 5% drift.

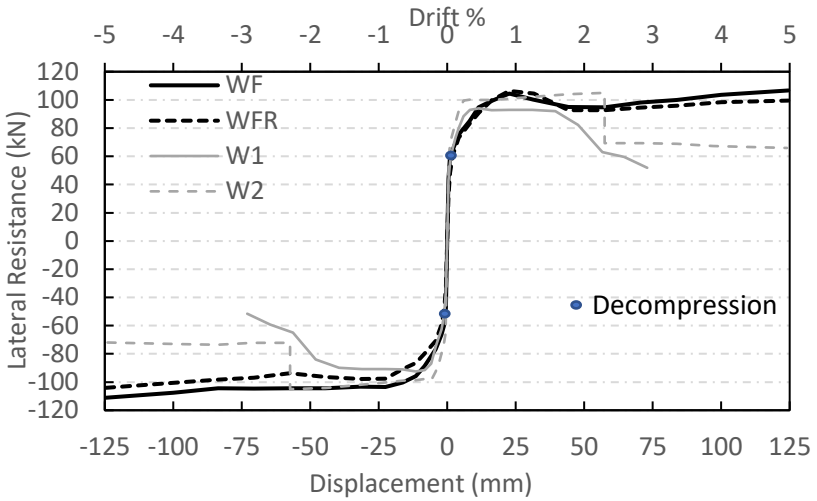


**Fig. 5.11.** Envelope response for ED-CRMWs with external flexural arms (WF and WFR) and with internal axial yielding bars (W1 and W2)

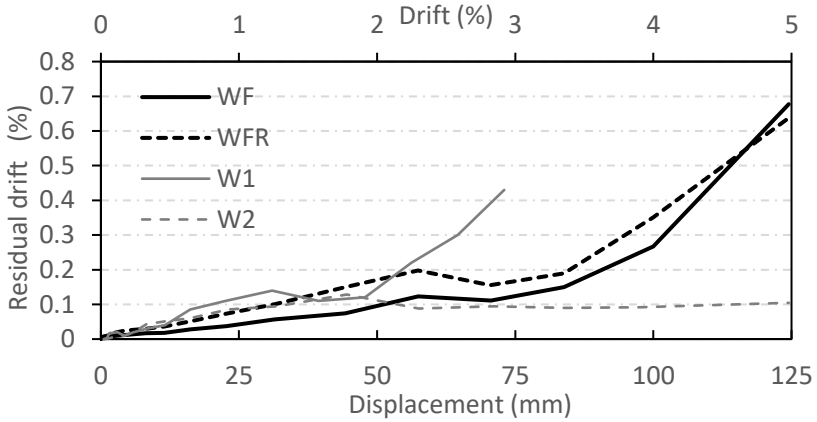


**Fig. 5.12.** Residual drift for ED-CRMWs with external flexural arms (WF and WFR) and with internal axial yielding bars (W1 and W2)

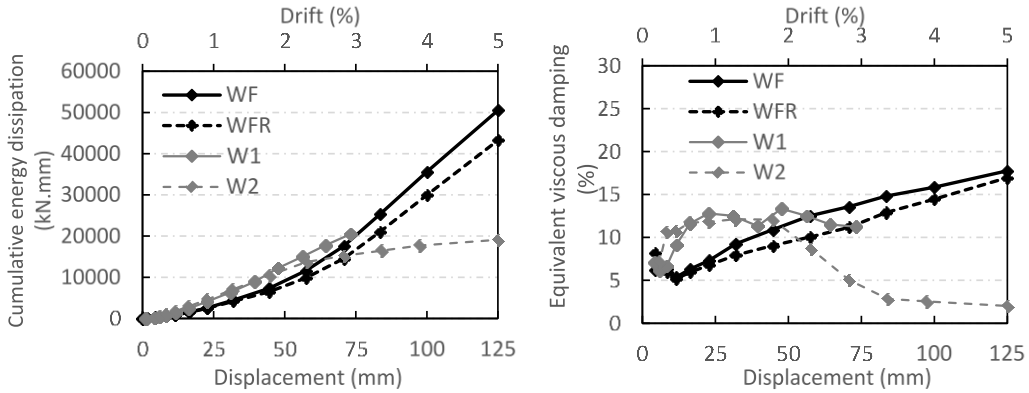


**Fig. 5.13.** a) Cumulative energy dissipation, and b) Equivalent viscous damping, for ED-CRMWs with external flexural arms (WF and WFR) and with internal axial yielding bars (W1 and W2)

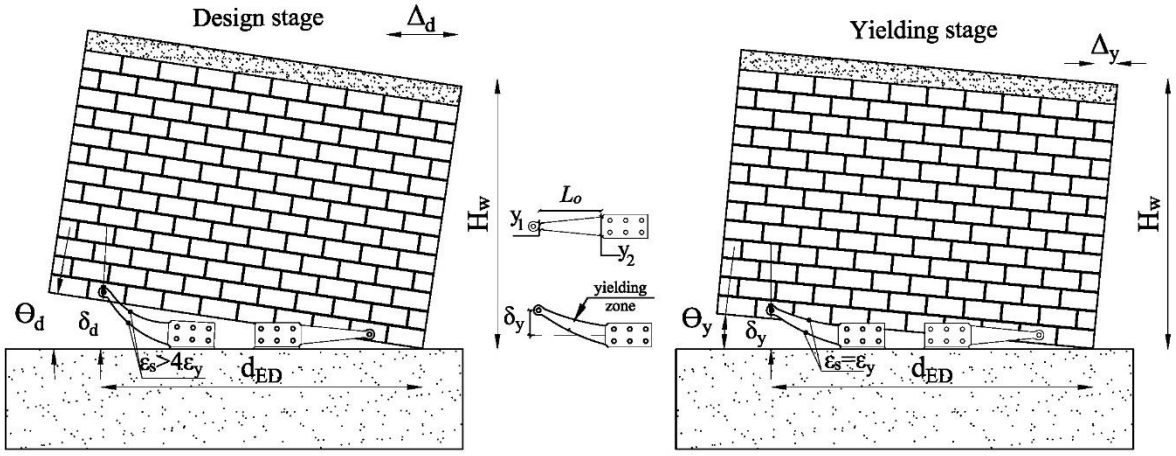


**Fig. 5.14.** Wall and flexural arm deformation relationship at design and yielding stages.

# Chapter 6

## SUMMARY, CONCLUSIONS, AND RECOMMENDATIONS

## 6.1. SUMMARY

This dissertation focused on investigating the development of controlled rocking masonry walls without the use of unbonded post-tensioning. The main objective of this dissertation is to facilitate the adoption of Energy Dissipation Controlled Rocking Masonry Walls (ED-CRMWs) in the future editions of masonry standards (e.g., CSA S304 and TMS 402) as a resilient seismic force-resisting system opposing to unbonded post-tensioned controlled rocking masonry walls (PT-CRMWs). This dissertation started by evaluating PT-CRMWs to identify their seismic performance and compare it to SRMWs. In this respect, a seismic collapse risk simulation was performed first on PT-CRMWs to evaluate their seismic collapse margin ratios. Following this, experimental results were presented for six half-scaled two-story ED-CRMWs. The six walls had different parameters such as confining techniques (i.e., boundary elements or steel plates), level of axial compression, location of unbonded axial yielding energy dissipation bars and horizontal reinforcement ratio. The ED-CRMWs were tested under quasi-static displacement-controlled cyclic loading representing seismic loading. Based on the experimental results, a detailed design approach and seismic performance evaluation for the newly proposed ED-CRMWs was presented, which incorporate the effect of higher modes. Finally, an enhanced ED-CRMW using externally

attached energy dissipation (i.e., flexural arms) was presented and experimentally tested and then the flexural arms were replaced with new arms and the wall was retested to quantify the system resilience and inspect the repair quality. Finally, design guidance for this wall type was presented.

## 6.2. CONCLUSIONS

The dissertation provided both numerical and experimental results to support the future inclusion of ED-CRMWs in seismic design codes and standards. The following conclusions highlight the main findings and contributions of the research presented in the previous chapters:

Within the context of the current North American codes and standards, there is no clear and unique seismic response modification factor *R* for unbonded posttensioned rocking masonry shear walls. The ASCE/SEI 7-16 (ASCE/SEI 2016) assigns a small value of 1.5 for prestressed masonry walls, considering them as ordinary unreinforced masonry walls and neglecting the rocking behavior. Conversely, the seismic collapse risk analysis showed that an *R* factor of 5 can be assigned for low rise PT-CRMWs with a sufficient safety margin against collapse under maximum considered earthquake levels. However, for high-rise PT-CRMWs, if higher modes are not mitigated or considered in the design, then *R* should not be 5, indicating that adequate vertical reinforcement bars or multiple rocking joints need to be placed in PT-CRMWs to mitigate higher modes.

In this dissertation, a simplified macro multi-spring model was developed that was capable of simulating the behavior of both the PT-CRMWs and ED-CRMWs. In case of neglecting the effect of higher modes, elastic beam-column elements were used to model the walls (case of PT-CRMWs), while if the masonry rocking wall is designed to include the higher modes, then force-based elements were used to model the wall element (case of ED-CRMWs). In both cases, the developed multi-spring model simulating the rocking base joint yielded good agreement with the experimental results in terms of simulating the initial stiffness, peak load, stiffness degradation, strength deterioration, hysteretic shape and pinching behavior at different drift levels. Therefore, this model is expected to be a useful tool for future modeling of system-level response, which can subsequently be adapted for the evaluation of a building rather than only individual walls.

The experimental test results of six ED-CRMWs with different configurations (including energy dissipation location, level of axial compression, and toe confinement techniques) showed that all walls were capable of achieving minimized and localized damage only within the crushing toes of the wall while the rest of wall body is free of damage. Also, all walls achieved a high level of self-centering capability with less than 0.15% residual drift, except for one unconfined wall (W1). These results demonstrated that relying on gravity loads from the slabs can maintain the high performance of the rocking wall regarding the self-centering capability, the limited damage, and the high drift capacity. In addition, considering the cost savings by avoiding post-tensioning and with the simplicity of the energy

dissipation used, ED-CRMWs are considered a promising alternative to PT-CRMWs.

The end-confined technique significantly enhanced the ED-CRMW response in all aspects. For instance, the extent of damage was reduced with only superficial vertical cracks on the face shell while the confined core remained intact up to 4.90% drift, achieving higher displacement ductility compared to other walls with only 0.1% residual drift. On the other hand, the Priestley plates confining technique limited the damage to be within the first course only and maintained an acceptable self-centering performance with less than 0.15% residual drifts but did not significantly enhance the wall displacement ductility.

A detailed design approach for the newly proposed system ED-CRMWs was presented and could be adapted to clauses of future editions of TMS 402 and CSA S304, as no design guideline in masonry standards yet incorporate the rocking mechanism with energy dissipation devices. The intended performance was confirmed by analysis of 20 ED-CRMW archetypes, where at the design level earthquake all nonlinearity was from the rocking base joint with damage-free wall bodies. At the maximum considered earthquake, another source of nonlinearity was permitted to reduce the effects of the higher modes on overturning moments by allowing limited vertical reinforcement yielding, which significantly reduced the overturning moment demands.

Moreover, a seismic evaluation of the ED-CRMW system was conducted to propose a seismic response modification factor *R* of 7 that fully met the acceptance criteria of the FEMA P695 (FEMA 2009) methodology against collapse. As such, comparing this system with both special reinforced masonry walls and PT-CRMWs, ED-CRMWs achieved a higher value of *R* and with self-centering capability and limited damage.

The experimental double testing of the ED-CRMW system with externally attached flexural arms and special hollow steel block connection confirmed the idea of considering the reported system as a high-performance structure geared toward system resilience. This is because the damage was localized to the replaceable flexural arms and wall corner only, without any spread of tension or shear cracks, and was easily repaired to fully restore its strength, ductility, energy dissipation and self-centering capabilities. These promising results led to integrating the wall design approach with flexural arm design to the design guidance described above.

## 6.3. RECOMMENDATIONS FOR FUTURE RESEARCH

The research presented in this dissertation included numerical and experimental investigation and response quantification of ED-CRMWs. However, as in any innovative research, several issues remain unresolved and require further investigation. The following points present possible extensions to the research in order to expand the knowledge related to the seismic response of ED-CRMWs:

- Quasi-static fully reversed cyclic loading was the adopted loading protocol in the experimental work of the two phases. This allows evaluation of the wall damage propagation and performance. However, additional experimental tests under dynamic loading (such as shake table testing) are still needed to represent demands closer, including the effect of vertical accelerations, to those experienced during seismic events and to verify the proposed design approach.
- Studying the wall impact during dynamic testing and how it affects the wall crushing toes is vital, and adding an impact absorber material at rocking toes is also a case study that is worth investigating.
- This study adopted individually tested ED-CRMWs walls; however, studies at the system level are needed as previous studies proved that a group of walls inside a building can have different performance in terms of strength, ductility and stiffness. Such testing should also consider the influence that deformations of the system in one direction have on the performance of walls in the orthogonal direction.
- This study considered the slab loading to self-center the ED-CRMWs. In this regard, there is a vital need to experimentally study a connection between the wall system and slab diaphragm to accommodate the wall uplifting demand at the design level earthquake. Also, all load combinations shall be considered during design to ensure rocking behavior.
- This study considered two types of energy dissipation devices, axial yielding bars and flexural arms. In this regard, other types of energy dissipation, such as

friction or viscous, can be investigated in future research to evaluate the most appropriate type suitable for ED-CRMWs in terms of susceptibility to damage, displacement capacity, durability, and ease of replacement.

- As the proposed ED-CRMW systems mainly depend on gravity loads to have their strength, which depends on the architectural plan configuration, these systems may require more walls at their floor plans to reduce the demands compared to PT-CRMWs. Further studies could develop design guidance on how to adapt ED-CRMW systems to walls with relatively low gravity loads.
- The study focuses on walls with aspect ratios greater than one to allow rocking. For a squat wall, future studies are needed as this wall system would require providing joints to divide it into walls of smaller lengths, each wall having its own energy dissipation device(s).
- The more resilient ED-CRMW described in Chapter 5 used replaceable ED devices that were outside the footprint of the wall. To address cases where this may not be acceptable for architectural reasons, further study is recommended to develop a means of containing the replaceable ED within the wall footprint.